UNIVERSITY OF SALERNO
DEPARTMENT OF CHEMISTRY AND BIOLOGY
"A. ZAMBELLI"

Ph.D. Course in Chemistry
XXXV Cycle

Molecular Properties Via Induced Current Densities

Supervisors
Prof. Riccardo Zanasi
Prof. Guglielmo Monaco

Ph.D. Student
Francesco F. Summa

Co-Supervisor
Prof. Paolo Lazzeretti

External-Supervisor
Prof. Sonia Coriani
DTU Chemistry
Technical University Denmark

Ph.D Course Coordinator
Prof. Claudio Pellecchia

Academic year: 2022-2023

Reviewed by

Prof. Carlo Gatti
CNR-SCITEC (Istituto di Scienze e Tecnologie Chimiche Giulio Natta, sezione di via Golgi) c/o Department of Chemistry, Università degli Studi di Milano, via Golgi 19
20133 Milano (Italy)

Prof. Andrew Teale
University of Nottingham, School of Chemistry, University Park,
Nottingham NG7 2RD UK

Contents

List of Papers

Published Papers on the Topics of the Thesis in the Three-Year Period

1. G. Monaco, F. F. Summa, and R. Zanasi
Atomic Size Adjusted Calculation of the Magnetically Induced Current Density, *Chem. Phys. Lett.* **2020**, 745, 137281
https://doi.org/10.1016/j.cplett.2020.137281

2. F. F. Summa, G. Monaco, L. T. Scott, and R. Zanasi
Disentangling the Contributions to the Proton Magnetic Shielding in Carbon Nanohoops and Nanobelts: Evidence for a Paratropic Belt-Current, *J. Phys. Chem. Lett.* **2020**, 11, 18, 7489–7494.
https://pubs.acs.org/doi/pdf/10.1021/acs.jpclett.0c02261

3. G. Monaco, F. F. Summa, and R. Zanasi
Program Package for the Calculation of Origin-Independent Electron Current Density and Derived Magnetic Properties in Molecular Systems, *J. Chem. Inf. Mod.*, **2021**, 61, 1, 270–283.
https://doi.org/10.1021/acs.jcim.0c01136

4. F. F. Summa, G. Monaco, R. Zanasi, S. Pelloni and P. Lazzeretti
Electronic Currents Induced by Optical Fields and Rotatory Power Density in Chiral Molecules, *Molecules*, **2021**, 26(14), 4195.
https://doi.org/10.3390/molecules26144195

5. F. F. Summa, G. Monaco, P. Lazzeretti, and R. Zanasi
Assessment of the Performance of DFT Functionals in the Fulfillment of Off-Diagonal Hypervirial Relationships, *Phys. Chem. Chem. Phys.* **2021**, 23, 15268-15274.
https://doi.org/10.1039/D1CP01298C

6. A. Landi, F. F. Summa, and G. Monaco
Magnetic Aromaticity of Cycloporphyrin Nanorings, *Chemistry* **2021**, 3(3), 991-1004.
https://doi.org/10.3390/chemistry3030071

7. F. F. Summa, and P. Lazzeretti
Electronic Currents and Anapolar Response Induced in Molecules by Monochromatic Light, *Chemistry* **2021**, 3(3), 1022-1036.
https://doi.org/10.3390/chemistry3030073

8. F. F. Summa, G. Monaco, P. Lazzeretti, and R. Zanasi
Origin-Independent Densities of Static and Dynamic Molecular Polarizabilities, *J. Phys. Chem. Lett.* **2021**, 12, 8855-8864.
https://doi.org/10.1021/acs.jpclett.1c02545

9. F. F. Summa, G. Monaco, and R. Zanasi
Decomposition of Molecular Integrals into Atomic Contributions Via Becke Partitioning Scheme: a Caveat, *Croat. Chem. Acta* **2021**, 94, 1.
https://doi.org/10.5562/cca3817

10. F. F. Summa, G. Monaco, P. Lazzeretti, and R. Zanasi
Dynamic Toroidisability as Universal Property of Atoms and Molecules in Optical Electric Fields, *J. Chem. Phys.* **2022**, 156, 054106
https://doi.org/10.1063/5.0082731

11. F. F. Summa, G. Monaco, R. Zanasi and P. Lazzeretti
Origin Independent Current Density Vector Fields Induced by Time-Dependent Magnetic Field. I. The LiH Molecule, *J. Chem. Phys.* **2022**, 156, 154105
https://doi.org/10.1063/5.0089605

12. G. Pierri, R. Schettini, F. F. Summa, F. De Riccardis, G. Monaco, I. Izzo and C. Tedesco
Right- and Left-Handed PPI Helices in Cyclic Dodecapeptoids, *Chem. Commun.* **2022**, 58, 5253-5256
https://doi.org/10.1039/D2CC00682K

13. F. F. Summa and R. Citro
Many Body Current Density from Foldy-Wouthuysen Transformation of the Dirac-Coulomb Hamiltonian, *Physchem* **2022**, 2(2), 96-107
https://doi.org/10.3390/physchem2020007

14. G. Monaco, R. Zanasi and F. F. Summa
Magnetic Characterization of the Infinitene Molecule, *J. Phys. Chem. A* **2022**, 126, 23, 3717–3723
https://pubs.acs.org/doi/10.1021/acs.jpca.2c02339

15. A. Landi, F. F. Summa, R. Zanasi and G. Monaco
On the JAP Method for the Indirect Determination of Delocalized Currents from Experimental Chemical Shifts, *ChemPhysChem* **2022**, 23, e202200411 (1 of 6)
https://doi.org/10.1002/cphc.202200411

16. F. F. Summa, R. Zanasi and P. Lazzeretti
On the Computation of Frequency-Dependent Molecular Magnetizabilities via Dynamical Charge and Current electron Densities
Submitted to J. Chem. Phys.

Other Publications in the Same Period

1. A. Macchia, F. F. Summa, A. Di Mola, C. Tedesco, G. Pierri, A. R. Ofial, G. Monaco, and A. Massa
Base-Promoted Cascade Reactions for the Synthesis of 3,3 Dialkylated Isoindolin-1-ones and 3-Methyleneisoindolin-1-ones, *J. Org. Chem.* **2021**, 86, 21, 15128-15138.
https://doi.org/10.1021/acs.joc.1c01794

2. A. Di Mola, F. F. Summa, P. Oliva, F. Lelj, S. Remiddi, L. Silvani, and A. Massa
Synergistic Properties of Solutions of Arabinogalactan (AG) and Hyaluronic Acid (HA) Sodium Salt, *Molecules* **2021**, 26(23), 7246.
https://doi.org/10.3390/molecules26237246

3. A. Macchia, F. F. Summa, G. Monaco, A. Eitzinger, A. R. Ofial, A. Di Mola and A. Massa
Access to β-Alkylated γ-Functionalized Ketones via Conjugate Additions to Arylideneisoxazol-5-ones and $Mo(CO)_6$ Mediated Reductive Cascade Reactions, *ACS Omega* **2022**, 7, 10, 8808–8818
https://doi.org/10.1021/acsomega.1c07081

Within the text, citations in boldface refer to published papers using the enumeration provided above.

Acknowledgments

> As I get older, I realize being wrong isn't a bad thing like they teach you in the school. It is an opportunity to learn something
>
> Richard Feynman

The contents of this thesis are based on research activities carried out during the years 2020-2022, to a large extent at the Department of Chemistry and Biology "A. Zambelli" of the University of Salerno. Furthermore, I have had a very rewarding stay at the Technical University of Denmark in Copenhagen, whose hospitality is gratefully acknowledged.

I would like to employ this first page of my thesis to thank those who helped me to make it a reality.

First of all, Professor Riccardo Zanasi, who gave me confidence and welcomed with great enthusiasm into his team. A person of the highest cultural and human depth, he has done his utmost, during these years of doctoral work, in teaching me all that was possible, making my work, however heavy, imbued with passion and a desire to always go further. I thank him, with admiration, for all the time he has dedicated to me, time invaluable to me, from which I have drawn invaluable lessons.

I thank Professor Guglielmo Monaco for his helpfulness, mutual esteem, and encouragement. His invaluable collaboration has spurred me to constantly improve myself.

I thank Professor Paolo Lazzeretti for providing his many years of experience and preparation. Collaborating with him has been a continuous enrichment and stimulating confrontation.

I thank Professor Sonia Coriani for making my stay abroad very pleasant both from a working and personal points of view. I met, in her work group, competent and collaborative colleagues and in her person a reference figure. I thank her also for her family exquisite hospitality.

Words cannot describe, in toto, the immense gratitude towards all of them.

Last but not least, I would like to thank my family, in particular my parents, my sisters, my grandparents and my uncles who, as always, have been the pillar to lean on and have never let me lack unwavering support and encouragement in every respect.

CHAPTER 1

Introduction

To describe the interaction of a molecule with an external field the concept of *molecular response* comes into play. Formally, it refers to response theory, namely, the calculation of field-induced molecular properties through changes in expectation values.[1] The molecular response can take a variety of forms depending on the perturbing field, which can be electric, magnetic, or both, static or dynamic as in the case of the electromagnetic radiation. For example, in the presence of an electric field (time-independent or time-dependent) the electron cloud is polarised and an induced electric moment (static or dynamic) appears as a consequence of the perturbation. In the case of a magnetic field, electron currents start flowing within the electron cloud, thus providing an induced magnetic moment. Such induced electric and magnetic moments can be measured and may serve in technological applications.

What primarily changes during the interaction with a static field is the energy of the molecule, which becomes a function of the applied field. The quantum mechanical calculation of the molecular energy is, therefore, a way to achieve the determination of molecular properties. Customarily, the molecular energy is expanded in a series of powers of the applied field, which leads to identification of each term of the series with a specific molecular property. Accordingly, molecular properties are classified as first-order (or intrinsic), second-order (or linear), third, fourth, ... (or non-linear) properties. To cite a few, electric polarizability and magnetizability are linear response molecular properties, whereas first and second hyperpolarizabilities are non-linear molecular properties. By definition, molecular properties are tensors of rank determined by the powers of the applied field.

From a chemical point of view, it is interesting to consider how molecular composition and structure affect response properties. The same atoms, or group of atoms (functional groups) in different chemical contests, can provide substantially different molecular properties. Understanding why this happens may have practical consequences, as for example, directing the work of synthesis of new molecules showing peculiar characteristics.[2] In this regard, the theoretical work can provide a substantial help, avoiding lengthy laboratory work and waste of substances. The great computing power nowadays available makes it possible to achieve this purpose, with a precision comparable to the experimen-

tal one. Computational methods, based on perturbation theory/response theory, not practicable only a few years ago, are now routinely employed for the prediction of static and dynamic molecular properties at different levels of approximation.[3–5]

However, despite the great amount of work done so far, there is still a lot to do. Although the knowledge of electronic energies and transition moments between electronic states allows the determination of a number of molecular response properties, the level of understanding that they permit is not sufficient to analyze in detail the contributions from different places of the molecular space. This further step, necessary for chemical interpretation, can be achieved in the context of a slightly less explored field, i.e., those of *molecular density functions*, in particular those associated to response properties, whose dependence on the position makes this type of study feasible.

The present PhD thesis describes the research work carried out in the last three years by the candidate for the determination and exploration of molecular property density functions associated to the response to external electric and magnetic perturbations.

As it regards this work, there are two basic density functions: the electron charge density $\rho = -e\gamma$, which is a scalar field, and the electron current density $\boldsymbol{J} = -e\boldsymbol{j}$, which is a vector field, where $\gamma(\boldsymbol{r})$ and $\boldsymbol{j}(\boldsymbol{r})$ are the probability density and probability current density functions, respectively, from which the majority of electric and magnetic property density functions can be derived. The general concept of a density function for a molecular property was pioneered by Jameson and Buckingham.[6, 7]

A very appealing feature of any density function is its dependence on the position vector $\boldsymbol{r}$, which permits to explore the molecular space looking for the loci most important for determining the final value of a property. In other words, it allows to study the connection between molecular structure and properties. For example, aromaticity is an important chemical concept that is connected to enhanced diamagnetic response and low-field NMR proton chemical shift. Both phenomena find an explanation in the so called ring-current model,[8–11] which assumes a delocalized current induced in the π-electron cloud of a ring of conjugated atoms by an external magnetic field. Visualization of the magnetically induced current density and related proton magnetic shielding density, permits a rapid understanding of what is happening inside the molecule and provides insight into shape and size of any ring currents present in the molecule under investigation. Moreover, a quantitative estimation of the current density flux gives a measure of aromaticity, which is not directly influenced by any geometrical factor.[12, 13]

In the following, property density functions will be discussed in a number of ways, from their definition, to their representation and analysis. An important aspect of those density functions derived in terms of current density is their vector nature. This entails a number of different ways for their visualization and adoption of topological tools for their analysis.

After a first part of general definitions, a second part of the present thesis is devoted to the molecular density functions induced by a static magnetic field. A third part concerns the dynamic response due to the interaction with the radiation.

All developed methods have been implemented within the freely available SYSMOIC package.[14][**3**]

Throughout this thesis, SI units are used and standard tensor formalism is employed, e.g., the Einstein convention of implicit summation over two repeated Greek indices is applied. The third-rank Levi-Civita skew-tensor is indicated by $\epsilon_{\alpha\beta\gamma}$ and δ_{ij} is the Kronecker's delta. The imaginary unit is represented by a Roman i.

List of Acronyms

AIM Atoms in Molecules

AMM Arrighini-Maestro-Moccia

BO Born-Oppenheimer

BCP Bond Critical Point

BCS Benzene Current Strenght

CCP Cage Critical Point

CP Critical Point

BHandHLYP Becke-Half-and-Half-Lee-Yang-Parr

CCSD Coupled Cluster Singles and Doubles

CDT Current Density Tensor

CI Configuration Interaction

CO Common Origin

CPHF Coupled Perturbed Hartree-Fock

CPKS Coupled Perturbed Kohn-Sham

CSDGT Continuous Set of Damped Gauge Transformations

CSGT Continuous Set of Gauge Transformations

CSGT-STD CSGT STandarD

CSGT-BS CSGT Bragg Slater

CSGT-BCP CSGT Bond Critical Point

CTOCD Continuous Transformation of the Origin of Current Density

CTOCD-DZ CTOCD Diamagnetic Zero

CTOCD-PZ CTOCD Paramagnetic Zero

DFT Density Functional Theory

ELF Electron Localization Function

EOA Electric Octopole Approximation

EQA Electric Quadrupole Approximation

HF Hartree-Fock

^{1}**H-NMR** Proton Nuclear Magnetic Resonance

HOMO Highest Occupied Molecular Orbital

JAP Jirásek-Anderson-Peeks

KB Keith and Bader

LUMO Lowest Unoccupied Molecular Orbital

NC Non Covalent

NCI Non Covalent Interaction

NICS Nucleus Independent Chemical Shift

NCP Nuclear Critical Point

NMR Nuclear Magnetic Resonance

MAGIC MAGnetically Induced Current

MEMDP Mixed Electric Dipole Magnetic Dipole Polarizability

MG Molecular Graph

QCT Quantum Chemical Topology

QM Quantum Mechanical

QTAIM Quantum Theory of Atoms In Molecules

RCP Ring Critical Point

RPA Random Phase Approximation

SG Stagnation Graph

SI Systéme International d'unités

SL Stagnation Line

SOS Sum Over States

SP Stagnation Point

TDDFT Time-Dependent Density Functional Theory

TDHF Time-Dependent Hartree-Fock

CHAPTER 2

General Definitions

We premise that our study of the interaction of a molecule with external electric and magnetic fields is a semi-classical one, i.e., the molecular system is treated at QM level, whilst the fields are considered at classical level. Therefore, we start recalling the basic equations of the classical electromagnetic field theory that will be used in the following. Then the quantum mechanical Hamiltonian in the BO approximation will be outlined together with some of the tools needed for the topological analysis of the scalar field $\rho(\boldsymbol{r})$, useful also for the analysis of the current density exposed later.

2.1 Classical Hamiltonian

In the presence of an electric field $\boldsymbol{E}(\boldsymbol{r},t)$ and a magnetic field $\boldsymbol{B}(\boldsymbol{r},t)$ a classical particle of charge q, moving with velocity $\boldsymbol{v}$, experiences the Lorentz force[15]

$$\boldsymbol{F} = q(\boldsymbol{E} + \boldsymbol{v} \times \boldsymbol{B}) \tag{2.1}$$

The electric and magnetic fields satisfy Maxwell's equations[15–19]

$$\boldsymbol{\nabla} \cdot \boldsymbol{E} = \frac{\rho}{\epsilon_0} \tag{2.2}$$

$$\boldsymbol{\nabla} \times \boldsymbol{B} - \mu_0 \epsilon_0 \frac{\partial \boldsymbol{E}}{\partial t} = \mu_0 \boldsymbol{J} \tag{2.3}$$

$$\boldsymbol{\nabla} \cdot \boldsymbol{B} = 0 \tag{2.4}$$

$$\boldsymbol{\nabla} \times \boldsymbol{E} + \frac{\partial \boldsymbol{B}}{\partial t} = \boldsymbol{0} \tag{2.5}$$

When the charge density $\rho(\boldsymbol{r},t)$ and the current density $\boldsymbol{J}(\boldsymbol{r},t)$ are the sources of the fields, Maxwell's equations can be solved for $\boldsymbol{E}(\boldsymbol{r},t)$ and $\boldsymbol{B}(\boldsymbol{r},t)$. Conversely, since the particles are driven by the Lorentz force (2.1), $\rho(\boldsymbol{r},t)$ and $\boldsymbol{J}(\boldsymbol{r},t)$ depend on $\boldsymbol{E}(\boldsymbol{r},t)$ and $\boldsymbol{B}(\boldsymbol{r},t)$. Maxwell's equations consist of two pairs of distinct equations: the inhomogeneous equations (2.2) and (2.3), and the homogeneous equations (2.4) and (2.5). The

first and third equations correspond to Gauss' law for electric and magnetic fields, respectively. The other two equations are the Ampère-Maxwell and Faraday-Neumann-Lenz laws.

The homogeneous equations are independent of the charges and currents in the system. Indeed, according the equation (2.4) the magnetic field can be written as the curl of a vector field, as the divergence of a curl is always vanishing. Such a vector field is known as the vector potential $\boldsymbol{A}$[15, 19]. Therefore

$$\boldsymbol{B} = \boldsymbol{\nabla} \times \boldsymbol{A} \tag{2.6}$$

Replacing this equation in the Faraday-Neumann-Lenz law (2.5), one has

$$\boldsymbol{\nabla} \times \boldsymbol{E} + \frac{\partial \left(\boldsymbol{\nabla} \times \boldsymbol{A} \right)}{\partial t} = \boldsymbol{0} \tag{2.7}$$

This equation can be rearranged to obtain

$$\boldsymbol{\nabla} \times \left(\boldsymbol{E} + \frac{\partial \boldsymbol{A}}{\partial t} \right) = \boldsymbol{0} \tag{2.8}$$

The quantity $\boldsymbol{E} + \frac{\partial \boldsymbol{A}}{\partial t}$ is irrotational[20, 21] so that

$$\boldsymbol{E} = -\boldsymbol{\nabla}\Phi - \frac{\partial \boldsymbol{A}}{\partial t} \tag{2.9}$$

where Φ is known as the scalar or electric potential (the minus sign is largely a matter of convention).

From Maxwell's inhomogeneous equations one can extract the continuity equation

$$\frac{\partial \rho}{\partial t} + \boldsymbol{\nabla} \cdot \boldsymbol{J} = 0 \tag{2.10}$$

that relates ρ and $\boldsymbol{J}$ and expresses the law of local conservation of the electric charge. Equations (2.6) and (2.9) do not define uniquely the scalar and the vector potentials, indeed they are the same after a gauge transformation. Changing the potentials according to

$$\boldsymbol{A} \to \boldsymbol{A}' = \boldsymbol{A} + \boldsymbol{\nabla} f \tag{2.11}$$

$$\Phi \to \Phi' = \Phi - \frac{\partial f}{\partial t} \tag{2.12}$$

where f is an arbitrary function of position, leads to exactly the same fields, since[22]

$$\boldsymbol{\nabla} \times (\boldsymbol{\nabla} f) = \boldsymbol{0}$$

Equations (2.11) and (2.12) define a *change of gauge*.

Now, let us consider an idealized situation in which, the charged particles in the molecule are not the sources of the fields, rather they interact with an electromagnetic field generated by other sources considered sufficiently remote so that we can set them to zero. Then, Maxwell's equations become

$$\boldsymbol{\nabla} \cdot \boldsymbol{E} = 0 \tag{2.13}$$

$$\boldsymbol{\nabla} \cdot \boldsymbol{B} = 0 \tag{2.14}$$

$$\boldsymbol{\nabla} \times \boldsymbol{E} = -\frac{\partial \boldsymbol{B}}{\partial t} \tag{2.15}$$

$$\boldsymbol{\nabla} \times \boldsymbol{B} = \mu_0 \epsilon_0 \frac{\partial \boldsymbol{E}}{\partial t} \tag{2.16}$$

which constitute a set of coupled, first-order, partial differential equations for $\boldsymbol{E}$ and $\boldsymbol{B}$. They can be decoupled taking the curl of (2.15) and (2.16), arriving at

$$\boldsymbol{\nabla}^2\boldsymbol{E} - \mu_0\epsilon_0\frac{\partial^2\boldsymbol{E}}{\partial t^2} = 0 \tag{2.17}$$

$$\boldsymbol{\nabla}^2\boldsymbol{B} - \mu_0\epsilon_0\frac{\partial^2\boldsymbol{B}}{\partial t^2} = 0 \tag{2.18}$$

whose solutions are the very well known plane waves defined by

$$\boldsymbol{E}(\boldsymbol{r},t) = \Re\left\{\boldsymbol{E}_0 e^{\mathrm{i}(\omega t - \boldsymbol{k}\cdot\boldsymbol{r})}\right\} \tag{2.19}$$

$$\boldsymbol{B}(\boldsymbol{r},t) = \Re\left\{\boldsymbol{B}_0 e^{\mathrm{i}(\omega t - \boldsymbol{k}\cdot\boldsymbol{r})}\right\} \tag{2.20}$$

where $\omega = 2\pi\nu$ is the angular frequency in radians per second, ν is the frequency in hertz, $\boldsymbol{k} = k\hat{\boldsymbol{n}} = \frac{\omega}{c}\hat{\boldsymbol{n}}$ is the the wave vector and $\hat{\boldsymbol{n}}$ is the unit vector indicating the direction of propagation of the wave. $\boldsymbol{E}$ and $\boldsymbol{B}$ oscillate periodically in phase on planes mutually orthogonal whose intersection coincides with $\boldsymbol{k}$. Using the Euler relation

$$e^{\mathrm{i}x} = \cos(x) + \mathrm{i}\sin(x) \tag{2.21}$$

it follows that

$$\boldsymbol{E}(\boldsymbol{r},t) = \boldsymbol{E}_0\cos(\omega t - \boldsymbol{k}\cdot\boldsymbol{r}) \tag{2.22}$$

$$\boldsymbol{B}(\boldsymbol{r},t) = \boldsymbol{B}_0\cos(\omega t - \boldsymbol{k}\cdot\boldsymbol{r}) \tag{2.23}$$

To treat the molecule at QM level, we need a Hamiltonian describing the interaction between the charged particles in the molecule and the external electromagnetic fields traveling in the vacuum. We start considering the Lagrangian of n non-relativistic charged particles with charges q_i, masses m_i and positions $\boldsymbol{r}_i$ in an electromagnetic field,[23] that is,

$$\mathscr{L} = \sum_i^n \frac{1}{2}m_i\dot{\boldsymbol{r}}_i^2 + \sum_i^n q_i\dot{\boldsymbol{r}}_i\cdot\boldsymbol{A}_i - \sum_i^n q_i\Phi_i \tag{2.24}$$

in Cartesian coordinates. Indeed, if we substitute (2.24) in the Euler-Lagrange equations

$$\sum_i^n\left[\frac{d}{dt}\left(\frac{\partial\mathscr{L}}{\partial\dot{\boldsymbol{r}}_i}\right) - \frac{\partial\mathscr{L}}{\partial\boldsymbol{r}_i}\right] = \boldsymbol{0} \tag{2.25}$$

we obtain that

$$\sum_i^n\left[m_i\ddot{\boldsymbol{r}}_i + q_i\boldsymbol{\nabla}\Phi_i + q\frac{d\boldsymbol{A}_i}{dt} - q_i\boldsymbol{\nabla}(\dot{\boldsymbol{r}}_i\cdot\boldsymbol{A}_i)\right] = \boldsymbol{0} \tag{2.26}$$

which is equivalent to Newton's equations with the Lorentz's force. The generalized momenta are given by:

$$\boldsymbol{p}_i = \frac{\partial\mathscr{L}}{\partial\dot{\boldsymbol{r}}_i} = m_i\dot{\boldsymbol{r}}_i + q_i\boldsymbol{A}_i \tag{2.27}$$

which can be rearranged expressing the velocities in terms of the momenta as

$$\dot{\boldsymbol{r}}_i = \frac{\boldsymbol{p}_i - q_i\boldsymbol{A}_i}{m_i} \tag{2.28}$$

Now, starting from the definition of the Hamiltonian

$$H = \left\{ \sum_i^n \boldsymbol{p}_i \cdot \dot{\boldsymbol{r}}_i \right\} - \mathscr{L} \tag{2.29}$$

and considering that

$$\mathscr{L} = \sum_i^n \left[\boldsymbol{p}_i - \frac{1}{2} m_i \dot{\boldsymbol{r}}_i \right] \cdot \dot{\boldsymbol{r}}_i - \sum_i^n q_i \Phi_i \tag{2.30}$$

we obtain

$$H = \sum_i^n \boldsymbol{p}_i \cdot \dot{\boldsymbol{r}}_i - \sum_i^n \left[\boldsymbol{p}_i - \frac{1}{2} m_i \dot{\boldsymbol{r}}_i \right] \cdot \dot{\boldsymbol{r}}_i + \sum_i^n q_i \Phi_i \tag{2.31}$$

from which it follows

$$H = \sum_i^n \frac{1}{2} m_i \dot{\boldsymbol{r}}_i^2 + \sum_i^n q_i \Phi_i \tag{2.32}$$

If we introduce the mechanical momentum of the particle[23]

$$\boldsymbol{\pi}_i = \boldsymbol{p}_i - q_i \boldsymbol{A}_i \tag{2.33}$$

the total Hamiltonian can be written as

$$\boxed{H = \sum_i^n \frac{\boldsymbol{\pi}_i^2}{2m_i} + \sum_i^n q_i \Phi_i} \tag{2.34}$$

This approximation is called minimal coupling.[24] For the sake of simplicity, here we have not taken into account the Coulomb interaction between charged particles. In the QM approach one has to substitute the classical Hamiltonian H with the operator $\hat{H}$. To conclude this section, let us consider the case of a time-independent magnetic field.

For a static and uniform magnetic field equation (2.6) reads

$$B_\alpha = \epsilon_{\alpha\beta\gamma} \nabla_\beta r_\gamma = \text{constant} \tag{2.35}$$

In this case, a satisfactory solution for $\boldsymbol{A}$ is given by

$$\boldsymbol{A} = \frac{1}{2} \boldsymbol{B} \times \boldsymbol{r} \qquad \Rightarrow \qquad A_\alpha = \frac{1}{2} \epsilon_{\alpha\beta\gamma} B_\beta r_\gamma \tag{2.36}$$

since, as it can be easily shown

$$\begin{aligned}
(\boldsymbol{\nabla} \times \boldsymbol{A})_\alpha &= \frac{1}{2} \epsilon_{\alpha\beta\gamma} \nabla_\beta \epsilon_{\gamma\lambda\mu} B_\lambda r_\mu \\
(\boldsymbol{\nabla} \times \boldsymbol{A})_\alpha &= \frac{1}{2} \left(\delta_{\alpha\lambda} \delta_{\beta\mu} - \delta_{\alpha\mu} \delta_{\beta\lambda} \right) \nabla_\beta B_\lambda r_\mu \\
(\boldsymbol{\nabla} \times \boldsymbol{A})_\alpha &= \frac{1}{2} B_\alpha \nabla_\beta r_\beta - \frac{1}{2} B_\beta \nabla_\beta r_\alpha \\
(\boldsymbol{\nabla} \times \boldsymbol{A})_\alpha &= \frac{3}{2} B_\alpha - \frac{1}{2} B_\alpha = B_\alpha
\end{aligned} \tag{2.37}$$

Equation (2.36), proposed for the vector potential $\boldsymbol{A}$, also accounts for the Coulomb gauge

$$\boldsymbol{\nabla} \cdot \boldsymbol{A} = \nabla_\alpha \epsilon_{\alpha\beta\gamma} B_\beta r_\gamma = 0 \tag{2.38}$$

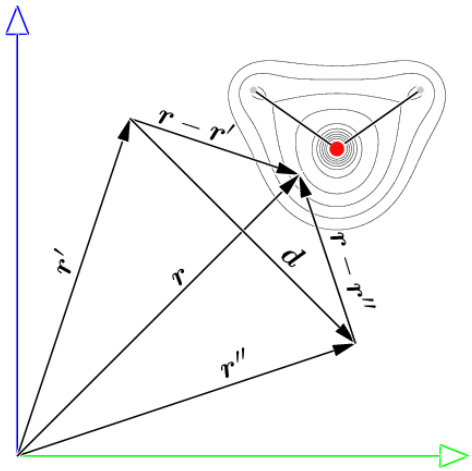

Figure 2.1: For any point at distance $\boldsymbol{r}$ from a physically relevant reference point, in the coordinate system K, the descriptions of induced charge and current densities of two observers in systems K' and K'', with origins $\boldsymbol{r}'$ and $\boldsymbol{r}''$ respectively, separated by a distance $\boldsymbol{d}$ are equivalent.

However, as stated before, this solution is not unique due to the gauge transformations (2.11) and (2.12). For example, two different choices of the origin of the vector potential, as shown in Figure 2.1, give two alternative forms of $\boldsymbol{A}$ at any given point in space, though the field itself remains the same.

$$\boldsymbol{A}' = \frac{1}{2}\boldsymbol{B} \times (\boldsymbol{r} - \boldsymbol{r}') \tag{2.39}$$

$$\boldsymbol{A}' \to \boldsymbol{A}'' = \frac{1}{2}\boldsymbol{B} \times (\boldsymbol{r} - \boldsymbol{r}'') \tag{2.40}$$

$$\boldsymbol{A}'' = \boldsymbol{A}' - \frac{1}{2}\boldsymbol{B} \times \boldsymbol{d} \tag{2.41}$$

$$\boldsymbol{\nabla} \times \boldsymbol{A}'' = \boldsymbol{\nabla} \times \boldsymbol{A}' \tag{2.42}$$

Therefore a shift of the origin of coordinates by a vector $\boldsymbol{d} = \boldsymbol{r}'' - \boldsymbol{r}'$ corresponds to a change of gauge (2.11) where

$$f(\boldsymbol{r}) = -\frac{1}{2}\boldsymbol{B} \times \boldsymbol{d} \cdot \boldsymbol{r} \tag{2.43}$$

since

$$\begin{aligned} \nabla_\alpha f(\boldsymbol{r}) &= -\frac{1}{2}\nabla_\alpha(\boldsymbol{B} \times \boldsymbol{d} \cdot \boldsymbol{r}) \\ &= -\frac{1}{2}\nabla_\alpha \epsilon_{\beta\gamma\delta} B_\gamma d_\delta r_\beta \\ &= -\frac{1}{2}\epsilon_{\beta\gamma\delta} B_\gamma d_\delta \delta_{\alpha\beta} \\ \boldsymbol{\nabla} f(\boldsymbol{r}) &= -\frac{1}{2}\boldsymbol{B} \times \boldsymbol{d} \\ \boldsymbol{A}'' &= \boldsymbol{A}' + \boldsymbol{\nabla} f(\boldsymbol{r}) \end{aligned} \tag{2.44}$$

2.2 Quantum Mechanical Hamiltonian

Within the BO approximation,[25] for a molecule with n electrons and N clamped nuclei, charge, mass, position, canonical and angular momentum of the k-th electron are indicated, in the configuration space, by $-e$, m_e, $\boldsymbol{r}_k$, $\hat{\boldsymbol{p}}_k = -\mathrm{i}\hbar\boldsymbol{\nabla}_k$, $\hat{\boldsymbol{l}}_k = \boldsymbol{r}_k \times \hat{\boldsymbol{p}}_k$, $k = 1, 2 \ldots n$, using boldface letters for electronic vector operators. Analogous quantities for nuclei are $Z_a e$, M_a, $\boldsymbol{R}_a$, *etc.*, for $a = 1, 2 \ldots N$. Capitals denote n-electron vector operators, e.g., for position, canonical momentum and angular momentum

$$\hat{\boldsymbol{R}} = \sum_{k=1}^{n} \boldsymbol{r}_k \quad \hat{\boldsymbol{P}} = \sum_{k=1}^{n} \hat{\boldsymbol{p}}_k \quad \hat{\boldsymbol{L}} = \sum_{k=1}^{n} \hat{\boldsymbol{l}}_k$$

Then, the electric dipole operator in the length formalism becomes

$$\hat{\mu}_\alpha = -e\hat{R}_\alpha \tag{2.45}$$

the electric quadrupole operator is

$$\hat{\mu}_{\alpha\beta} = -\frac{e}{2} \sum_{k=1}^{n} (r_\alpha r_\beta)_k \tag{2.46}$$

and the magnetic dipole operator

$$\hat{m}_\alpha = -\frac{e}{2m_\mathrm{e}} \hat{L}_\alpha \tag{2.47}$$

Let us introduce the general definition of n-electron probability density matrix functions[22] for a stationary state wavefunction $\Psi(\boldsymbol{X})$

$$\gamma\left(\boldsymbol{x}_1; \boldsymbol{x}_1'\right) = n \int \Psi\left(\boldsymbol{x}_1, \boldsymbol{X}_1\right) \Psi^*\left(\boldsymbol{x}_1', \boldsymbol{X}_1\right) d\boldsymbol{X}_1 \tag{2.48}$$

of electronic space-spin coordinates $\boldsymbol{x}_k = \boldsymbol{r}_k \otimes \eta_k$, $k = 1, 2, \ldots, n$, where

$$\boldsymbol{X}_1 \equiv \{\boldsymbol{x}_2, \ldots, \boldsymbol{x}_n\} \quad \boldsymbol{X} = \{\boldsymbol{x}_1, \boldsymbol{X}_1\} \quad d\boldsymbol{X}_1 \equiv \{d\boldsymbol{x}_2, \ldots, d\boldsymbol{x}_n\} \tag{2.49}$$

By integrating over the spin variable η_1, a spatial probability density matrix is obtained

$$\gamma(\boldsymbol{r}; \boldsymbol{r}') \equiv \gamma(\boldsymbol{r}_1; \boldsymbol{r}_1') = \int_{\eta_1' = \eta_1} \gamma\left(\boldsymbol{x}_1; \boldsymbol{x}_1'\right) d\eta_1 \tag{2.50}$$

Putting $\boldsymbol{r} = \boldsymbol{r}'$ we obtain the probability charge density

$$\gamma(\boldsymbol{r}) \equiv \gamma(\boldsymbol{r}; \boldsymbol{r}) \tag{2.51}$$

For the reference state Ψ_a the probability and charge densities are

$$\gamma(\boldsymbol{r}) = n \int \Psi_a\left(\boldsymbol{r}, \boldsymbol{X}_1\right) \Psi_a^*\left(\boldsymbol{r}, \boldsymbol{X}_1\right) d\boldsymbol{X}_1 \tag{2.52}$$

$$\rho(\boldsymbol{r}) = -e\gamma(\boldsymbol{r}) \tag{2.53}$$

Now, let us transform the classical Hamiltonian (2.34) for the interaction with time-dependent fields in the corresponding quantum mechanical operator. To have a correct

description of the molecular system, we must also take into account the Coulomb interactions between charged particles, not introduced before for the sake of simplicity. The QM Hamiltonian reads[22]

$$\hat{H} = \frac{1}{2m_{\mathrm{e}}} \sum_{k}^{n} \hat{\boldsymbol{\pi}}_k^2 - e \sum_{k}^{n} \Phi_k + \hat{V}(\boldsymbol{r}) \tag{2.54}$$

with

$$\hat{V}(\boldsymbol{r}) = \frac{e^2}{8\pi\varepsilon_0} \sum_{k,j}{}' \frac{1}{r_{kj}} - \frac{e^2}{8\pi\varepsilon_0} \sum_{a,k} \frac{Z_a}{r_{ak}} + \frac{e^2}{8\pi\varepsilon_0} \sum_{a,a'}{}' \frac{Z_a Z_{a'}}{R_{aa'}} \tag{2.55}$$

where primes mean that, performing the double summation, $k \neq j$ and $a \neq a'$. After some manipulation (2.54) can be conveniently rewritten as

$$\hat{H} = \hat{H}^{(0)} + \hat{H}^{(1)} + \hat{H}^{(2)} \tag{2.56}$$

where

$$\hat{H}^{(0)} = -\frac{\hbar^2}{2m_{\mathrm{e}}} \sum_{k}^{n} \boldsymbol{\nabla}_k^2 + \hat{V}(\boldsymbol{r}) \tag{2.57}$$

$$\hat{H}^{(1)} = -\frac{\mathrm{i}e\hbar}{2m_{\mathrm{e}}} \sum_{k}^{n} (\boldsymbol{\nabla}_k \cdot \boldsymbol{A}_k + \boldsymbol{A}_k \cdot \boldsymbol{\nabla}_k) - e \sum_{k}^{n} \Phi_k \tag{2.58}$$

$$\hat{H}^{(2)} = \frac{e^2}{2m_{\mathrm{e}}} \sum_{k}^{n} \boldsymbol{A}_k^2 \tag{2.59}$$

Now a question arises: "What are the explicit forms for vector and scalar potentials $\boldsymbol{A}_k$ and Φ_k that we have to consider for the interaction with electric and magnetic time-dependent fields?" A solution can be that of taking into account the series expansions of the vector and scalar potentials about a reference point, which is set equal to the origin[26]

$$A_\alpha(\boldsymbol{r}, t) = \sum_{j=0}^{\infty} \frac{j+1}{(j+2)!} \epsilon_{\alpha\beta\gamma} r_\gamma r_{\alpha_1} r_{\alpha_2} \cdots r_{\alpha_j} B_{\alpha_j \alpha_{j-1} \cdots \alpha_1 \beta}(\boldsymbol{0}, t) \tag{2.60}$$

$$\Phi(\boldsymbol{r}, t) = -\sum_{j=0}^{\infty} \frac{1}{(j+1)!} r_\alpha r_{\alpha_1} r_{\alpha_2} \cdots r_{\alpha_j} E_{\alpha_j \alpha_{j-1} \cdots \alpha_1 \alpha}(\boldsymbol{0}, t) \tag{2.61}$$

with

$$B_{\alpha_j \alpha_{j-1} \cdots \alpha_1 \alpha}(\boldsymbol{0}, t) \equiv \left[\frac{\partial^j B_\alpha(\boldsymbol{r}, t)}{\partial r_{\alpha_j} \partial r_{\alpha_{j-1}} \cdots \partial r_{\alpha_1}} \right]_{\boldsymbol{r}=\boldsymbol{0}} \tag{2.62}$$

and

$$E_{\alpha_j \alpha_{j-1} \cdots \alpha_1 \alpha}(\boldsymbol{0}, t) \equiv \left[\frac{\partial^j E_\alpha(\boldsymbol{r}, t)}{\partial r_{\alpha_j} \partial r_{\alpha_{j-1}} \cdots \partial r_{\alpha_1}} \right]_{\boldsymbol{r}=\boldsymbol{0}} \tag{2.63}$$

obtained according to the Bloch derivation,[26] satisfying the gauge conditions (2.11) and (2.12), with a scalar function defined as

$$f(\boldsymbol{r}, t) = -\sum_{j=1}^{\infty} \frac{1}{j!} r_{\alpha_1} r_{\alpha_2} \cdots r_{\alpha_j} A_{\alpha_j \alpha_{j-1} \cdots \alpha_1}(\boldsymbol{0}, t) \tag{2.64}$$

in which

$$A_{\alpha_j\alpha_{j-1}\cdots\alpha_1\alpha}(\mathbf{0},t) \equiv \left[\frac{\partial^j A_\alpha(\boldsymbol{r},t)}{\partial r_{\alpha_j}\partial r_{\alpha_{j-1}}\cdots\partial r_{\alpha_1}}\right]_{\boldsymbol{r}=\mathbf{0}} \tag{2.65}$$

Within the Bloch gauge, we get for the divergence of the new vector potential

$$\boldsymbol{\nabla}\cdot\boldsymbol{A} = \sum_{j=0}^{\infty}\frac{(j+1)(j+2)}{(j+3)!}\epsilon_{\alpha\beta\gamma}r_\alpha r_{\alpha_1}r_{\alpha_2}\cdots r_{\alpha_j}B_{\alpha_j\alpha_{j-1}\cdots\alpha_1\beta\gamma}(\mathbf{0},t) \tag{2.66}$$

that is, the Bloch potentials fulfill neither the Lorenz gauge

$$\boldsymbol{\nabla}\cdot\boldsymbol{A} + \mu_0\epsilon_0\frac{\partial\Phi}{\partial t} = 0 \tag{2.67}$$

nor the Coulomb gauge,

$$\boldsymbol{\nabla}\cdot\boldsymbol{A} = 0 \tag{2.68}$$

except for a static and uniform magnetic field. In the latter case, we have

$$\boldsymbol{A}_k = \frac{1}{2}\boldsymbol{B}\times\boldsymbol{r}_k \tag{2.69}$$

from which it follows that $\hat{H}^{(1)}$ becomes

$$\hat{H}^{(1)} = -\frac{\mathrm{i}e\hbar}{2m_\mathrm{e}}\sum_k^n \boldsymbol{B}\times\boldsymbol{r}_k\cdot\boldsymbol{\nabla}_k = \frac{e}{2m_\mathrm{e}}\sum_k^n \boldsymbol{l}_k\cdot\boldsymbol{B} \tag{2.70}$$

(in this case Φ is vanishing). In general, for time-dependent fields, different orders in the potentials $\boldsymbol{A}$ and Φ must be considered to obtain a correct description of the molecular system in the presence of an electromagnetic field. The most simple one is the case of the *electric dipole approximation*, introduced for the first time by Maria Göppert Mayer,[27] in which $\boldsymbol{A}(\boldsymbol{r},t) = 0$ and $\Phi(\boldsymbol{r},t) = -r_\alpha E_\alpha(\mathbf{0},t)$. Then, one has

$$\hat{H}^{(1)} = -e\sum_k^n \Phi_k = e\sum_k^n r_{k\alpha}E_\alpha(\mathbf{0},t) = -\hat{\mu}_\alpha E_\alpha(\mathbf{0},t) \tag{2.71}$$

The electric dipole approximation corresponds to a situation in which the wavelength of the radiation is much longer than molecular size, so that the molecule effectively sees only a uniform electric field rather than the full electromagnetic wave. This approximation is therefore reasonable for small- and medium-sized molecules exposed to electromagnetic radiation with wavelengths in the ultraviolet region, or longer. In the dipole approximation, the magnetic field is absent. To have a perturbing magnetic field, we need the expansion (2.60) truncated at first-order, at least. In general, to construct the Hamiltonian $\hat{H}^{(1)}$, a truncation of order n in the electric field must be accompanied by a truncation at order $n-1$ in the magnetic field.[5] To show how this can be accomplished let us consider

$$\boxed{\hat{H}^{(1)} = \hat{H}^{(1)}_\Phi + \hat{H}^{(1)}_A} \tag{2.72}$$

where $\hat{H}^{(1)}_\Phi$ and $\hat{H}^{(1)}_A$ contain respectively the electric and magnetic multipolar expansion. For the electric multipolar expansion we have

$$\boxed{\hat{H}^{(1)}_\Phi = -\sum_{j=0}^{\infty}\left[\hat{\mu}_{\alpha\alpha_1\alpha_2\cdots\alpha_j}E_{\alpha_j\alpha_{j-1}\cdots\alpha_1\alpha}(\mathbf{0},t)\right]} \tag{2.73}$$

with

$$\hat{\mu}_{\alpha\alpha_1\cdots\alpha_j} = -\frac{e}{(j+1)!}\sum_k^n \left(r_\alpha r_{\alpha_1}\cdots r_{\alpha_j}\right)_k \tag{2.74}$$

For $\hat{H}_A^{(1)}$ the simpler approach, due to Bloch[26], consists to write the magnetic multipolar expansion as

$$\boxed{\hat{H}_A^{(1)} = -\sum_{j=0}^{\infty}\left[\hat{m}_{\alpha\alpha_1\alpha_2\cdots\alpha_j} B_{\alpha_j\alpha_{j-1}\cdots\alpha_1\alpha}(\mathbf{0},t)\right]} \tag{2.75}$$

with

$$\hat{m}_{\alpha\alpha_1\cdots\alpha_j} = -\frac{e}{2m_\mathrm{e}}\frac{j+1}{(j+2)!}\sum_k^n \left(l_\alpha r_{\alpha_1}\cdots r_{\alpha_j} + r_{\alpha_1}\cdots r_{\alpha_j} l_\alpha\right)_k \tag{2.76}$$

Using these Hamiltonians we have, for example, that in the *electric quadrupole approximation* (EQA),

$$\boxed{\begin{aligned}\hat{H}^{(1)} &= -\hat{\mu}_\alpha E_\alpha(\mathbf{0},t) - \hat{\mu}_{\alpha\beta}E_{\beta\alpha}(\mathbf{0},t) - \hat{m}_\alpha B_\alpha(\mathbf{0},t)\\ &= \hat{H}^{\boldsymbol{E}} + \hat{H}^{\boldsymbol{\nabla E}} + \hat{H}^{\boldsymbol{B}}\end{aligned}} \tag{2.77}$$

while in the *electric octopole approximation* (EOA)

$$\boxed{\begin{aligned}\hat{H}^{(1)} &= -\hat{\mu}_\alpha E_\alpha(\mathbf{0},t) - \hat{\mu}_{\alpha\beta}E_{\beta\alpha}(\mathbf{0},t) - \hat{\mu}_{\alpha\beta\gamma}E_{\gamma\beta\alpha}(\mathbf{0},t) - \hat{m}_\alpha B_\alpha(\mathbf{0},t) - \hat{m}_{\alpha\beta}B_{\beta\alpha}(\mathbf{0},t)\\ &= \hat{H}^{\boldsymbol{E}} + \hat{H}^{\boldsymbol{\nabla E}} + \hat{H}^{\boldsymbol{\nabla\nabla E}} + \hat{H}^{\boldsymbol{B}} + \hat{H}^{\boldsymbol{\nabla B}}\end{aligned}} \tag{2.78}$$

and so on.

In the following sections only the electric quadrupole approximation will be used to derive the total induced first order polarization charge and current density vector. This approximation corresponds to considering a uniform magnetic field, and a non uniform electric field with uniform gradient on the molecular domain. This is assumed to be enough to have a good description of the interaction between the molecule and the electromagnetic fields. In the case of strongly nonuniform optical fields more elaborate approximations would be needed.

2.3 Topological Analysis of the Electron Charge Density

The aim of this section is to recall briefly the concepts behind the topological analysis of $\rho(\boldsymbol{r})$, first introduced by Bader within the QTAIM theory,[28, 29] and then included under the broader scope of QCT by Popelier in 2003.[30] In QCT other fields, beyond $\boldsymbol{\nabla}\rho$ are also studied, such as the gradients of $\boldsymbol{\nabla}^2\rho(\boldsymbol{r})$, the gradient of the ELF function and others.[31, 32] A useful definition of an atom comes from QTAIM, indeed according to Ref.[28], we have

> A quantum subsystem is bounded by a surface $S(\boldsymbol{r})$ that satisfies the condition of "zero flux" in the gradient vector field of the charge density, the field $\boldsymbol{\nabla}\rho(\boldsymbol{r})$,
>
> $$\boldsymbol{\nabla}\rho(\boldsymbol{r}) \cdot \boldsymbol{n}(\boldsymbol{r}) = 0 \qquad \text{all } \boldsymbol{r} \text{ in } S(\boldsymbol{r}) \tag{2.79}$$
>
> where $\boldsymbol{n}(\boldsymbol{r})$ is the unit vector normal to the surface at $\boldsymbol{r}$. The application of this condition to a charge distribution results in its exhaustive and disjoint partitioning into a set of spatial regions, each of which, in general, contains a single nucleus.

This condition is the starting point of QCT analysis of the electron density $\rho(\boldsymbol{r})$ usually performed with a Newton-Raphson approach. The topology of ρ is understood by studying the gradient vector field $\boldsymbol{\nabla}\rho(\boldsymbol{r})$. This vector field is a collection of gradient paths, which are curves in space that follow the direction of steepest ascent in ρ.[28] Therefore a gradient path has a sense; it always originates and terminates at points where $\boldsymbol{\nabla}\rho(\boldsymbol{r})$ vanishes. These points are called *critical points*. CPs occurring in a 3D function, such as ρ, can be best characterized by the eigenvalues λ_i with $i = 1, 2, 3$ of the Hessian of ρ, evaluated at the CP, introducing the concepts of rank r and signature s. The Hessian is a 3×3 matrix, denoted by $\boldsymbol{\nabla}\boldsymbol{\nabla}\rho$, defined as[28, 30, 33]

$$\boldsymbol{H}\left[\rho(\boldsymbol{r}_c)\right] = \begin{pmatrix} \frac{\partial^2\rho}{\partial x\partial x} & \frac{\partial^2\rho}{\partial x\partial y} & \frac{\partial^2\rho}{\partial x\partial z} \\ \frac{\partial^2\rho}{\partial y\partial x} & \frac{\partial^2\rho}{\partial y\partial y} & \frac{\partial^2\rho}{\partial y\partial z} \\ \frac{\partial^2\rho}{\partial z\partial x} & \frac{\partial^2\rho}{\partial z\partial y} & \frac{\partial^2\rho}{\partial z\partial z} \end{pmatrix}_{\boldsymbol{r}=\boldsymbol{r}_c} \tag{2.80}$$

that contains all partial second derivatives of ρ with respect to the Cartesian position coordinates x, y and z. The Hessian matrix is always real and symmetric so it has real eigenvalues. Recalling that, the rank r of a CP refers to the number of non-zero eigenvalues while the signature s is the sum of the signs of the eigenvalues, it is possible to note that for a 3D scalar function only two kind of saddle points can exist. For example, one type of saddle point has two non-zero eigenvalues and one strictly positive. Consequently, its rank is three and its signature is $(-1) + (-1) + 1 = -1$. This is conveniently denoted[34] as a $(3, -1)$ point, or bond critical point (BCP), where the first index refers to the rank and the second to the signature. The BCPs are linked to the nuclei via the so-called atomic interaction line. This line consists of a pair of gradient paths, each of which originates at the BCP and terminates at a nucleus. The set of all atomic interaction lines occurring in a molecule is called the molecular graph (MG). Another topologically important object is the interatomic surface, which separates two bonded atoms. In summary, to be brief, the following kinds of CPs occur:[34]

- $(3, +1)$ Two positive curvatures: ρ is a minimum in the plane defined by the corresponding eigenvectors and a maximum along the third axis which is perpendicular to this plane. This CP is called *ring critical point* (RCP);

- $(3,-1)$ Two negative curvatures: ρ is a maximum in the plane defined by the corresponding eigenvectors but is a minimum along the third axis which is perpendicular to this plane. This CP is called BCP;
- $(3,+3)$ Three curvatures are positive: ρ is a local minimum. This CP is *called cage critical point* (CCP);
- $(3,-3)$ Three negative curvatures: ρ is a local maximum. This CP is called *nuclear critical point* (NCP) because it is usually, but not always,[35] found to be coincident with the nuclear coordinates.

The number and type of critical points[29, 30] that can coexist in a molecule or crystal follow a strict topological relationship which states that:

$$n_{\mathrm{NCP}} - n_{\mathrm{BCP}} + n_{\mathrm{RCP}} - n_{\mathrm{CCP}} = \begin{cases} 1 & \text{(Isolated molecules)} \\ 0 & \text{(Infinite crystals)} \end{cases} \tag{2.81}$$

where each n denotes the number of CP of each type. The first equality is known as the Poincaré–Hopf relationship and applies for isolated finite systems such as a molecule, the second equality is known as the Morse equation and applies in cases of infinite periodic lattices.[36] The concept of Poincaré index will be introduced, in detail, in chapter 3. Violation of equation (2.81) implies an inconsistent characteristic set, that a critical point has been missed, and that a further search for the missing critical point(s) is necessary. On the other hand, the fulfillment of this equation does not guarantee the completeness of the CPs search.

CHAPTER 3

Time-Independent Electron Current Density

This chapter has a dual aim. The first is to report the equations defining the total current density induced by a time-independent magnetic field, while the second is to show a procedure referred to as CTOCD that provides a solution to the well-known problem of the origin dependence of the computed current density vector field. Withing this chapter spin effects will not be taken into account.[37–39][**13**] To show how the QM expression for the total many body current density $\boldsymbol{J}$ can be obtained, the Landau-Lifshitz approach[37] is used which is based on the relation

$$\delta H_c = -\int \boldsymbol{J}(\boldsymbol{r}) \cdot \delta \boldsymbol{A}(\boldsymbol{r})\, d^3r \tag{3.1}$$

To use this idea for a QM system, Landau and Lifshitz argued that the classical Hamiltonian H_c is to be identified with the expectation value of the QM Hamiltonian according to

$$H_c = \langle H \rangle = \langle \Psi | \hat{H} | \Psi \rangle \tag{3.2}$$

Due to equation (3.1), only terms containing the vector potential $\boldsymbol{A}$ must be taken into account. Looking at the interaction Hamiltonian (2.54), one can see that the vector potential appears only in the first term on the r.h.s.. Then, defining

$$\hat{\mathrm{h}}(1) = \frac{\hat{\boldsymbol{\pi}}^2}{2m_\mathrm{e}} \tag{3.3}$$

and using equation (2.48) we can focus only on the term[22]

$$\left\langle \sum_k^n \hat{\mathrm{h}}(\mathrm{k}) \right\rangle = \int_{\boldsymbol{x}_1' = \boldsymbol{x}_1} \hat{\mathrm{h}}(1) \gamma(\boldsymbol{x}_1; \boldsymbol{x}_1')\, d\boldsymbol{x}_1 \tag{3.4}$$

Moreover, since spin-effects are not taken into account in $\hat{\mathrm{h}}(1)$, it is possible to complete the integration over spin variable and write the following equation

$$\left\langle \sum_k^n \hat{\mathrm{h}}(\mathrm{k}) \right\rangle \quad = \quad \int_{\boldsymbol{r}' = \boldsymbol{r}} \hat{\mathrm{h}}(1) \gamma(\boldsymbol{r}; \boldsymbol{r}')\, d^3r \tag{3.5}$$

recovering the spinless density (2.50) introduced in the previous chapter. To obtain the current density vector $\boldsymbol{J}$ from equation (3.1), we need to calculate the variation δH_c with respect to an infinitesimal change of the vector potential[38, 39][**13**]

$$\boldsymbol{A}(\boldsymbol{r}) + \delta\boldsymbol{A}(\boldsymbol{r}) \tag{3.6}$$

Expanding $\hat{\boldsymbol{\pi}}^2$ we have

$$\hat{\boldsymbol{\pi}}^2 = (-\mathrm{i}\hbar\boldsymbol{\nabla} + e\boldsymbol{A})^2 = -\hbar^2\boldsymbol{\nabla}^2 - \mathrm{i}\hbar e(\boldsymbol{A}\cdot\boldsymbol{\nabla} + \boldsymbol{\nabla}\cdot\boldsymbol{A}) + e^2\boldsymbol{A}^2 \tag{3.7}$$

Substituting this expression and the definition (2.50) in equation (3.5), we can write

$$\begin{aligned} H_c + \delta H_c = &\frac{n}{2m_\mathrm{e}} \int \Psi^*\left(\boldsymbol{r}, \boldsymbol{X}_1\right) \boldsymbol{\pi}^2 \, \Psi\left(\boldsymbol{r}, \boldsymbol{X}_1\right) d\boldsymbol{X}_1 \, d^3r + \\ &\frac{ne}{2m_\mathrm{e}} \int \Psi^*\left(\boldsymbol{r}, \boldsymbol{X}_1\right) \left[\delta\boldsymbol{A}\cdot\hat{\boldsymbol{p}} + \hat{\boldsymbol{p}}\cdot\delta\boldsymbol{A} + 2e\boldsymbol{A}\cdot\delta\boldsymbol{A}\right] \Psi\left(\boldsymbol{r}, \boldsymbol{X}_1\right) d\boldsymbol{X}_1 \, d^3r \end{aligned} \tag{3.8}$$

because

$$(\boldsymbol{A} + \delta\boldsymbol{A})^2 = \boldsymbol{A}\cdot\boldsymbol{A} + \delta\boldsymbol{A}\cdot\delta\boldsymbol{A} + 2\boldsymbol{A}\cdot\delta\boldsymbol{A} \tag{3.9}$$

and the second order variation $\delta\boldsymbol{A}\cdot\delta\boldsymbol{A}$ is not considered to be vanishingly small. From the previous equations it follows that

$$\delta H_c = \frac{ne}{2m_\mathrm{e}} \int \Psi^*\left(\boldsymbol{r}, \boldsymbol{X}_1\right) \left[\delta\boldsymbol{A}\cdot\hat{\boldsymbol{p}} + \hat{\boldsymbol{p}}\cdot\delta\boldsymbol{A} + 2e\boldsymbol{A}\cdot\delta\boldsymbol{A}\right] \Psi\left(\boldsymbol{r}, \boldsymbol{X}_1\right) d\boldsymbol{X}_1 \, d^3r \tag{3.10}$$

Let us consider now the term $\boldsymbol{\nabla}\cdot(\delta\boldsymbol{A}\Psi)$. If we apply the vector identity

$$\boldsymbol{\nabla}\cdot(f\boldsymbol{V}) = f\boldsymbol{\nabla}\cdot\boldsymbol{V} + \boldsymbol{\nabla}f\cdot\boldsymbol{V} \tag{3.11}$$

with $f = \Psi$ and $\boldsymbol{V} = \delta\boldsymbol{A}$ we obtain

$$\boldsymbol{\nabla}\cdot(\Psi\delta\boldsymbol{A}) = \Psi\boldsymbol{\nabla}\cdot(\delta\boldsymbol{A}) + \boldsymbol{\nabla}\Psi\cdot(\delta\boldsymbol{A}) \tag{3.12}$$

Multiplying the last equation on the left by Ψ^*, one can write

$$\Psi^*\boldsymbol{\nabla}\cdot(\Psi\delta\boldsymbol{A}) = \Psi^*\Psi\boldsymbol{\nabla}\cdot(\delta\boldsymbol{A}) + \Psi^*\boldsymbol{\nabla}\Psi\cdot(\delta\boldsymbol{A}) \tag{3.13}$$

The term $\Psi^*\Psi\boldsymbol{\nabla}\cdot(\delta\boldsymbol{A})$, on the r.h.s of the previous equation, can be identified with $f\boldsymbol{\nabla}\cdot\boldsymbol{V}$, in which $f = \Psi^*\Psi$ and $\boldsymbol{V} = \delta\boldsymbol{A}$, so using again the identity (3.11) one has

$$\Psi^*\boldsymbol{\nabla}\cdot(\Psi\delta\boldsymbol{A}) = \boldsymbol{\nabla}\cdot(\Psi^*\delta\boldsymbol{A}\Psi) - \boldsymbol{\nabla}(\Psi^*\Psi)\cdot\delta\boldsymbol{A} + \Psi^*\boldsymbol{\nabla}\Psi\cdot\delta\boldsymbol{A} \tag{3.14}$$

Considering that

$$\boldsymbol{\nabla}(\Psi^*\Psi)\cdot\delta\boldsymbol{A} = \boldsymbol{\nabla}\Psi^*\cdot\delta\boldsymbol{A}\Psi + \Psi^*\boldsymbol{\nabla}\Psi\cdot\delta\boldsymbol{A} \tag{3.15}$$

equation (3.13) can be rearranged in the form

$$\Psi^*\boldsymbol{\nabla}\cdot(\delta\boldsymbol{A}\Psi) = \boldsymbol{\nabla}\cdot(\Psi^*\delta\boldsymbol{A}\Psi) - \boldsymbol{\nabla}\Psi^*\cdot\delta\boldsymbol{A}\Psi \tag{3.16}$$

Applying the divergence theorem for the first term on the r.h.s of the last identity and considering that the wavefunction goes to zero at infinity we have

$$\int \boldsymbol{\nabla}\cdot(\Psi^*\delta\boldsymbol{A}\Psi)\, d^3r = 0 \tag{3.17}$$

from which relation (3.10) can be rewritten as

$$\begin{aligned}\delta H_c = &-n\frac{\mathrm{i}e\hbar}{2m_\mathrm{e}}\int \Psi^*\left(\boldsymbol{r},\boldsymbol{X}_1\right)\delta\boldsymbol{A}\cdot\boldsymbol{\nabla}\Psi\left(\boldsymbol{r},\boldsymbol{X}_1\right)\,d\boldsymbol{X}_1\,d^3r\\ &+n\frac{\mathrm{i}e\hbar}{2m_\mathrm{e}}\int \boldsymbol{\nabla}\Psi^*\left(\boldsymbol{r},\boldsymbol{X}_1\right)\cdot\delta\boldsymbol{A}\Psi\left(\boldsymbol{r},\boldsymbol{X}_1\right)\,d\boldsymbol{X}_1\,d^3r\\ &+n\frac{e^2}{m_\mathrm{e}}\int \Psi^*\left(\boldsymbol{r},\boldsymbol{X}_1\right)\boldsymbol{A}\cdot\delta\boldsymbol{A}\Psi\left(\boldsymbol{r},\boldsymbol{X}_1\right)\,d\boldsymbol{X}_1\,d^3r\end{aligned} \tag{3.18}$$

Comparing this last equation with (3.1) it follows that

$$\boldsymbol{J}(\boldsymbol{r}) = n\frac{\mathrm{i}e\hbar}{2m_\mathrm{e}}\int\left\{\Psi^*\left(\boldsymbol{r},\boldsymbol{X}_1\right)\boldsymbol{\nabla}\Psi\left(\boldsymbol{r},\boldsymbol{X}_1\right)-\Psi\left(\boldsymbol{r},\boldsymbol{X}_1\right)\boldsymbol{\nabla}\Psi^*\left(\boldsymbol{r},\boldsymbol{X}_1\right)\right\}d\boldsymbol{X}_1-\frac{e^2}{m_\mathrm{e}}\boldsymbol{A}\gamma(\boldsymbol{r}) \tag{3.19}$$

conventionally rewritten as

$$\boxed{\boldsymbol{J}(\boldsymbol{r}) = -\frac{e}{m_\mathrm{e}}\Re\left[\hat{\boldsymbol{\pi}}\gamma\left(\boldsymbol{r};\boldsymbol{r}'\right)\right]_{\boldsymbol{r}'=\boldsymbol{r}}} \tag{3.20}$$

In SI units the dimensions of $\boldsymbol{J}$ are $\left[\mathrm{Am}^{-2}\right]$. This is the equation obtained in the static case. Then, according to equation (2.10) it must be the case that $\boldsymbol{\nabla}\cdot\boldsymbol{J}=0$.

The expression of $\boldsymbol{J}(\boldsymbol{r})$ is conventionally rewritten as the sum of a paramagnetic and a diamagnetic term

$$\boldsymbol{J}(\boldsymbol{r}) = \boldsymbol{J}_\mathrm{p}(\boldsymbol{r}) + \boldsymbol{J}_\mathrm{d}(\boldsymbol{r}) \tag{3.21}$$

The paramagnetic term is

$$\boldsymbol{J}_\mathrm{p}(\boldsymbol{r}) = n\frac{\mathrm{i}e\hbar}{2m_\mathrm{e}}\int\left\{\Psi^*\left(\boldsymbol{r},\boldsymbol{X}_1\right)\boldsymbol{\nabla}\Psi\left(\boldsymbol{r},\boldsymbol{X}_1\right)-\Psi\left(\boldsymbol{r},\boldsymbol{X}_1\right)\boldsymbol{\nabla}\Psi^*\left(\boldsymbol{r},\boldsymbol{X}_1\right)\right\}d\boldsymbol{X}_1 \tag{3.22}$$

while the diamagnetic term, called also Larmor contribution, is

$$\boldsymbol{J}_\mathrm{d}(\boldsymbol{r}) = -\frac{e^2}{m_\mathrm{e}}\boldsymbol{A}\gamma(\boldsymbol{r}) \tag{3.23}$$

with the vector potential $\boldsymbol{A}$ defined as

$$\boldsymbol{A} = \boldsymbol{A}^{\boldsymbol{B}} + \sum_{I=1}^{N'}\boldsymbol{A}^{\boldsymbol{m}_I} \tag{3.24}$$

$$\boldsymbol{A}^{\boldsymbol{B}} = \frac{1}{2}\boldsymbol{B}\times\boldsymbol{r} \qquad \boldsymbol{A}^{\boldsymbol{m}_I} = \frac{\mu_0}{4\pi}\frac{\boldsymbol{m}_I\times(\boldsymbol{r}-\boldsymbol{R}_I)}{\left|\boldsymbol{r}-\boldsymbol{R}_I\right|^3} \tag{3.25}$$

Considering the reference state $\Psi=\Psi_a$ and expanding the wavefunction in powers of the applied external magnetic field $\boldsymbol{B}$, we have

$$\Psi_a = \Psi_a^{(0)} + \boldsymbol{\Psi}_a^{\boldsymbol{B}}\cdot\boldsymbol{B} + \cdots \tag{3.26}$$

Substituting this expansion in equation (3.19) we have

$$\begin{aligned}\boldsymbol{J}(\boldsymbol{r}) = n\frac{\mathrm{i}e\hbar}{2m_\mathrm{e}}\int\Big\{&(\Psi_a^{(0)}+\boldsymbol{\Psi}_a^{\boldsymbol{B}}\cdot\boldsymbol{B}+\cdots)^*\boldsymbol{\nabla}(\Psi_a^{(0)}+\boldsymbol{\Psi}_a^{\boldsymbol{B}}\cdot\boldsymbol{B}+\cdots)+\\ &-(\Psi_a^{(0)}+\boldsymbol{\Psi}_a^{\boldsymbol{B}}\cdot\boldsymbol{B}+\cdots)\boldsymbol{\nabla}(\Psi_a^{(0)}+\boldsymbol{\Psi}_a^{\boldsymbol{B}}\cdot\boldsymbol{B}+\cdots)^*\Big\}\,d\boldsymbol{X}_1\\ &-n\frac{e^2}{m_\mathrm{e}}\boldsymbol{A}\int(\Psi_a^{(0)}+\boldsymbol{\Psi}_a^{\boldsymbol{B}}\cdot\boldsymbol{B}+\cdots)(\Psi_a^{(0)}+\boldsymbol{\Psi}_a^{\boldsymbol{B}}\cdot\boldsymbol{B}+\cdots)^*d\boldsymbol{X}_1\end{aligned} \tag{3.27}$$

where we have omitted the function arguments for the sake of space. Collecting terms in different powers of the applied magnetic field, we can split the total current density as

$$J_\alpha(\boldsymbol{r}) = J_\alpha^{(0)}(\boldsymbol{r}) + \mathcal{J}_\alpha^{B_\beta}(\boldsymbol{r})B_\beta + \cdots \tag{3.28}$$

where $\mathcal{J}_\alpha^{B_\beta}$ is the second rank current density tensor[40] defined as

$$\mathcal{J}_\alpha^{B_\beta} = \frac{\partial J_\alpha^{\boldsymbol{B}}}{\partial B_\beta} \tag{3.29}$$

Considering that $\boldsymbol{\Psi}_a^{\boldsymbol{B}}$ is pure imaginary, i.e. $\boldsymbol{\Psi}_a^{\boldsymbol{B}*} = -\boldsymbol{\Psi}_a^{\boldsymbol{B}}$ the different terms are

$$\boldsymbol{J}^{(0)}(\boldsymbol{r}) = n\frac{\mathrm{i}e\hbar}{2m_\mathrm{e}}\int\{\Psi_a^{(0)*}\boldsymbol{\nabla}\Psi_a^{(0)} - \Psi_a^{(0)}\boldsymbol{\nabla}\Psi_a^{(0)*}\}\,d\boldsymbol{X}_1 \tag{3.30}$$

$$\boldsymbol{J}^{\boldsymbol{B}}(\boldsymbol{r}) = n\frac{\mathrm{i}e\hbar}{m_\mathrm{e}}\int\{\Psi_a^{(0)*}\boldsymbol{\nabla}\boldsymbol{\Psi}_a^{\boldsymbol{B}}\cdot\boldsymbol{B} + \boldsymbol{\Psi}_a^{\boldsymbol{B}*}\cdot\boldsymbol{B}\boldsymbol{\nabla}\Psi_a^{(0)}\}\,d\boldsymbol{X}_1 - \frac{ne^2}{2m_\mathrm{e}}\boldsymbol{B}\times\boldsymbol{r}\int\Psi_a^{(0)}\Psi_a^{(0)*}d\boldsymbol{X}_1 \tag{3.31}$$

Since $\Psi_a^{(0)}$ can always be chosen real, i.e. $\Psi_a^{(0)} = \Psi_a^{(0)*}$, we have $\boldsymbol{J}^{(0)}(\boldsymbol{r}) = \boldsymbol{0}$. In (3.31) it is still possible to distinguish a paramagnetic and a diamagnetic term

$$\boldsymbol{J}_\mathrm{p}^{\boldsymbol{B}}(\boldsymbol{r}) = n\frac{\mathrm{i}e\hbar}{m_\mathrm{e}}\int\{\Psi_a^{(0)*}\boldsymbol{\nabla}\boldsymbol{\Psi}_a^{\boldsymbol{B}}\cdot\boldsymbol{B} + \boldsymbol{\Psi}_a^{\boldsymbol{B}*}\cdot\boldsymbol{B}\boldsymbol{\nabla}\Psi_a^{(0)}\}\,d\boldsymbol{X}_1 \tag{3.32}$$

$$\boldsymbol{J}_\mathrm{d}^{\boldsymbol{B}}(\boldsymbol{r}) = -\frac{ne^2}{2m_\mathrm{e}}\boldsymbol{B}\times\boldsymbol{r}\int\Psi_a^{(0)}\Psi_a^{(0)*}d\boldsymbol{X}_1 \tag{3.33}$$

From Rayleigh-Schrödinger perturbation theory, the first order perturbed wavefunction is

$$\Psi_a^{B_\alpha} = -\frac{e}{2m_\mathrm{e}\hbar}\sum_{j\neq a}\omega_{ja}^{-1}\left|j\right\rangle\left\langle j\right|\hat{L}_\alpha\left|a\right\rangle \tag{3.34}$$

where $|a\rangle$ stands for the reference state $\Psi_a^{(0)}$. Substituting this equation in (3.32) we can see that the first-order perturbed paramagnetic component becomes

$$\begin{aligned} J_{\mathrm{p}_\alpha}^{\boldsymbol{B}}(\boldsymbol{r}) &= \frac{ne^2}{2m_\mathrm{e}^2\hbar}B_\beta\sum_{j\neq a}\frac{1}{\omega_{ja}} \\ &\times \Re\left\{\left\langle a\left|\hat{L}_\beta\right|j\right\rangle\int\Psi_j^{(0)*}(\boldsymbol{r},\boldsymbol{X}_1)\hat{p}_\alpha\Psi_a^{(0)}(\boldsymbol{r},\boldsymbol{X}_1)\,d\boldsymbol{X}_1\right. \\ &+ \left.\int\Psi_a^{(0)*}(\boldsymbol{r},\boldsymbol{X}_1)\hat{p}_\alpha\Psi_j^{(0)}(\boldsymbol{r},\boldsymbol{X}_1)\,d\boldsymbol{X}_1\left\langle j\left|\hat{L}_\beta\right|a\right\rangle\right\} \end{aligned} \tag{3.35}$$

Magnetic properties, like magnetizability and nuclear magnetic shielding, can be obtained by integrating the current density tensor field according to[41]

$$\xi_{\alpha\beta} = \frac{1}{4}\int r_\gamma\left(\epsilon_{\alpha\gamma\delta}\mathcal{J}_\delta^{B_\beta} + \epsilon_{\beta\gamma\delta}\mathcal{J}_\delta^{B_\alpha}\right)d^3r \tag{3.36}$$

$$\sigma_{\alpha\delta}^I = -\frac{\mu_0}{4\pi}\epsilon_{\alpha\beta\gamma}\int\frac{r_\beta - R_{I\beta}}{|\boldsymbol{r}-\boldsymbol{R}_I|^3}\mathcal{J}_\gamma^{B_\delta}(\boldsymbol{r})\,d^3r \tag{3.37}$$

3.1 Continuous Transformation of the Origin of the Current Density

Since the interest here is only on the linear response hereafter the magnetically induced first-order current density vector will be briefly referred to as current density and the second-rank current density tensor just as current density tensor. According to a definition proposed by Hirschfelder,[42] the current density, as well the charge density, is a subobservable. As a consequence, the exact current density tensor is *origin-independent* although it can be written as the sum of *origin-dependent* paramagnetic and diamagnetic contributions. In other words, in a change of the coordinate system, see picture 2.1,

$$\boldsymbol{r}' \rightarrow \boldsymbol{r}'' = \boldsymbol{r}' + \boldsymbol{d} \tag{3.38}$$

the total current density must remain unchanged, whilst the paramagnetic and diamagnetic terms change in a compensatory manner. For the change of origin (3.38) the paramagnetic and diamagnetic terms change according to[14][**3**]

$$\mathcal{J}_{\mathrm{p}_\alpha}^{B_\beta}(\boldsymbol{r}-\boldsymbol{r}'') = \mathcal{J}_{\mathrm{p}_\alpha}^{B_\beta}(\boldsymbol{r}-\boldsymbol{r}') + \mathcal{J}_{\mathrm{p}_\alpha}^{(\boldsymbol{d}\times\boldsymbol{B})_\beta}(\boldsymbol{r}) \tag{3.39}$$

$$\mathcal{J}_{\mathrm{d}_\alpha}^{B_\beta}(\boldsymbol{r}-\boldsymbol{r}'') = \mathcal{J}_{\mathrm{d}_\alpha}^{B_\beta}(\boldsymbol{r}-\boldsymbol{r}') + \mathcal{J}_{\mathrm{d}_\alpha}^{(\boldsymbol{d}\times\boldsymbol{B})_\beta}(\boldsymbol{r}) \tag{3.40}$$

with

$$\begin{aligned}
\mathcal{J}_{\mathrm{p}_\alpha}^{(\boldsymbol{d}\times\boldsymbol{B})_\beta}(\boldsymbol{r}) &= -\frac{ne^2}{2m_{\mathrm{e}}^2\hbar}\epsilon_{\beta\gamma\delta}d_\gamma \sum_{j\neq a}\frac{1}{\omega_{ja}} \\
&\quad \times\Re\left\{\left\langle a\left|\hat{P}_\delta\right|j\right\rangle\int\Psi_j^{(0)*}(\boldsymbol{r},\boldsymbol{X}_1)\,\hat{p}_\alpha\Psi_a^{(0)}(\boldsymbol{r},\boldsymbol{X}_1)\,d\boldsymbol{X}_1\right. \\
&\quad \left.+\int\Psi_a^{(0)*}(\boldsymbol{r},\boldsymbol{X}_1)\,\hat{p}_\alpha\Psi_j^{(0)}(\boldsymbol{r},\boldsymbol{X}_1)\,d\boldsymbol{X}_1\left\langle j\left|\hat{P}_\delta\right|a\right\rangle\right\}
\end{aligned} \tag{3.41}$$

$$\mathcal{J}_{\mathrm{d}_\alpha}^{(\boldsymbol{d}\times\boldsymbol{B})_\beta}(\boldsymbol{r}) = \frac{e^2}{2m_{\mathrm{e}}}\epsilon_{\alpha\beta\gamma}d_\gamma\gamma^{(0)}(\boldsymbol{r}) \tag{3.42}$$

Therefore, for any new origin $\boldsymbol{r}''$ of the current density tensor, one can write

$$\mathcal{J}_\alpha^{B_\beta}(\boldsymbol{r}-\boldsymbol{r}'') = \mathcal{J}_{\mathrm{p}_\alpha}^{B_\beta}(\boldsymbol{r}-\boldsymbol{r}') + \mathcal{J}_{\mathrm{p}_\alpha}^{(\boldsymbol{d}\times\boldsymbol{B})_\beta}(\boldsymbol{r}) + \mathcal{J}_{\mathrm{d}_\alpha}^{B_\beta}(\boldsymbol{r}-\boldsymbol{r}') + \mathcal{J}_{\mathrm{d}_\alpha}^{(\boldsymbol{d}\times\boldsymbol{B})_\beta}(\boldsymbol{r}) \tag{3.43}$$

Hence, the constraint for invariance of total current density tensor reduces to

$$\mathcal{J}_{\mathrm{p}_\alpha}^{(\boldsymbol{d}\times\boldsymbol{B})_\beta}(\boldsymbol{r}) = -\mathcal{J}_{\mathrm{d}_\alpha}^{(\boldsymbol{d}\times\boldsymbol{B})_\beta}(\boldsymbol{r}) \tag{3.44}$$

However, this condition is not true in practical calculations. To overcome this difficulty, and to obtain *origin-independent* current densities within the algebraic approximation, Keith and Bader[43] have reported an approach that employs a different origin for each point in real space. This method, which has been termed "continuous set of gauge transformations" by the authors, actually amounts to considering the shift $\boldsymbol{d}$, in equation (3.38), as a function of $\boldsymbol{r}$. However, it must be noted that within this approach the continuity condition for the current density is not satisfied in practical calculation (see section 3.1.6 for further considerations). It is better, from a physical point of view, to call this method "continuous transformation of the origin of the current density" (CTOCD) instead of "continuous set of gauge transformations" (CSGT).[44] Some possible forms for $\boldsymbol{d}(\boldsymbol{r})$ have been proposed during the years and in the following sections a description of the most important variants of them will be given.

3.1.1 CTOCD-DZ1

The simplest choice is to set $\boldsymbol{d}(\boldsymbol{r}) = \boldsymbol{r}$. This method is called "diamagnetic zero" or "ipsocentric"[45, 46] approach because it makes the diamagnetic contribution vanish everywhere for exact and approximate cases, indeed:[44]

$$\mathcal{J}_{\alpha}^{B_\beta}(\boldsymbol{r}) = \mathcal{J}_{\mathrm{p}_\alpha}^{B_\beta}(\boldsymbol{r}) + \mathcal{J}_{\mathrm{p}_\alpha}^{(\boldsymbol{d}\times\boldsymbol{B})_\beta}(\boldsymbol{r}) \tag{3.45}$$

where

$$\begin{aligned}
\mathcal{J}_{\mathrm{p}_\alpha}^{B_\beta}(\boldsymbol{r}) &= \frac{ne^2}{2m_{\mathrm{e}}^2\hbar}\sum_{j\neq a}\frac{1}{\omega_{ja}} \\
&\times \Re\Big\{\Big\langle a\Big|\hat{L}_\beta\Big|j\Big\rangle\int \Psi_j^{(0)*}(\boldsymbol{r},\boldsymbol{X}_1)\hat{p}_\alpha\Psi_a^{(0)}(\boldsymbol{r},\boldsymbol{X}_1)\,d\boldsymbol{X}_1 \\
&+ \int \Psi_a^{(0)*}(\boldsymbol{r},\boldsymbol{X}_1)\hat{p}_\alpha\Psi_j^{(0)}(\boldsymbol{r},\boldsymbol{X}_1)\,d\boldsymbol{X}_1\Big\langle j\Big|\hat{L}_\beta\Big|a\Big\rangle\Big\}
\end{aligned} \tag{3.46}$$

$$\begin{aligned}
\mathcal{J}_{\mathrm{p}_\alpha}^{(\boldsymbol{d}\times\boldsymbol{B})_\beta}(\boldsymbol{r}) &= -\frac{ne^2}{2m_{\mathrm{e}}^2\hbar}\epsilon_{\beta\gamma\delta}r_\gamma\sum_{j\neq a}\frac{1}{\omega_{ja}} \\
&\times\Re\left\{\left\langle a\left|\hat{P}_\delta\right|j\right\rangle\int\Psi_j^{(0)*}(\boldsymbol{r},\boldsymbol{X}_1)\,\hat{p}_\alpha\Psi_a^{(0)}(\boldsymbol{r},\boldsymbol{X}_1)\,d\boldsymbol{X}_1\right. \\
&\left.+\int\Psi_a^{(0)*}(\boldsymbol{r},\boldsymbol{X}_1)\,\hat{p}_\alpha\Psi_j^{(0)}(\boldsymbol{r},\boldsymbol{X}_1)\,d\boldsymbol{X}_1\left\langle j\left|\hat{P}_\delta\right|a\right\rangle\right\}
\end{aligned} \tag{3.47}$$

It has been proven, by numerical applications, that this choice of the shift function is not particularly good, as perturbed wavefunctions are involved in the calculations.[43, 47] For this reason other variants of the method have been proposed, which are detailed here in the following.

3.1.2 CTOCD-DZ2

The CTOCD-DZ1 approach requires very large basis sets and it is not recommended for the calculation of accurate nuclear magnetic shieldings and magnetizabilities. To overcome this difficulty, in the original implementation of the method,[43] an exponential function was used to shift the origin toward the nearest nucleus. This modification was termed by KB as CSDGT (continuous set of damped gauge transformations), which is also referred to in the literature as CTOCD-DZ2.[48]

Within the CTOCD-DZ2 approach the shift function is defined as:

$$\boldsymbol{d}(\boldsymbol{r}) = \boldsymbol{r} - \sum_a (\boldsymbol{r} - \boldsymbol{R}_a)\, e^{-\alpha|\boldsymbol{r}-\boldsymbol{R}_a|^4} \tag{3.48}$$

where the summation runs over all nuclei at their positions $\boldsymbol{R}_a$, and the positive constant α is somewhat arbitrarily set to 2 au. The CTOCD-DZ2 shift function is illustrated in Figure (3.1)

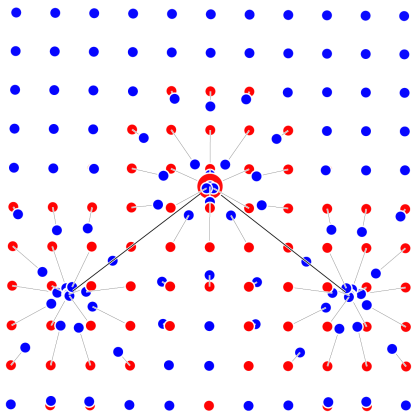

Figure 3.1: The $\boldsymbol{d}(\boldsymbol{r})$ function for H_2O molecule in the CTOCD-DZ2 approach. When applied to a red point in $\boldsymbol{r}$, the $\boldsymbol{d}(\boldsymbol{r})$ function shifts it to the blue point connected through a line.

The total current density tensor with this shift function becomes

$$\mathcal{J}_\alpha^{B_\beta}(\boldsymbol{r}) = \mathcal{J}_{\mathrm{p}_\alpha}^{B_\beta}(\boldsymbol{r}) + \mathcal{J}_{\mathrm{p}_\alpha}^{(\boldsymbol{d}\times\boldsymbol{B})_\beta}(\boldsymbol{r}) + \mathcal{J}_{\mathrm{d}_\alpha}^{(\boldsymbol{d}\times\boldsymbol{B})_\beta}(\boldsymbol{r}) \tag{3.49}$$

where $\mathcal{J}_{\mathrm{p}_\alpha}^{B_\beta}(\boldsymbol{r})$ is the term defined in (3.35) and

$$\begin{aligned}
\mathcal{J}_{\mathrm{p}_\alpha}^{(\boldsymbol{d}\times\boldsymbol{B})_\beta}(\boldsymbol{r}) &= \frac{ne^2}{2m_{\mathrm{e}}^2\hbar}\epsilon_{\beta\gamma\delta}\left\{r_\gamma - \sum_a (r_\gamma - R_{a\gamma})\, e^{-\alpha|\boldsymbol{r}-\boldsymbol{R}_a|^4}\right\}\sum_{j\neq a}\frac{1}{\omega_{ja}} \\
&\quad \times\Re\left\{\left\langle a\left|\hat{P}_\delta\right|j\right\rangle\int \Psi_j^{(0)*}(\boldsymbol{r},\boldsymbol{X}_1)\,\hat{p}_\alpha\Psi_a^{(0)}(\boldsymbol{r},\boldsymbol{X}_1)\,d\boldsymbol{X}_1\right. \\
&\quad \left. + \int \Psi_a^{(0)*}(\boldsymbol{r},\boldsymbol{X}_1)\,\hat{p}_\alpha\Psi_j^{(0)}(\boldsymbol{r},\boldsymbol{X}_1)\,d\boldsymbol{X}_1\left\langle j\left|\hat{P}_\delta\right|a\right\rangle\right\}
\end{aligned} \tag{3.50}$$

$$\mathcal{J}_{\mathrm{d}_\alpha}^{(\boldsymbol{d}\times\boldsymbol{B})_\beta}(\boldsymbol{r}) = -\frac{e^2}{2m_{\mathrm{e}}}\epsilon_{\alpha\beta\gamma}\sum_a\left\{(r_\gamma - R_{a\gamma})\, e^{-\alpha|\boldsymbol{r}-\boldsymbol{R}_a|^4}\right\}\gamma^{(0)}(\boldsymbol{r}) \tag{3.51}$$

3.1.3 CTOCD-PZ1

Since the paramagnetic contribution to the current density is the most difficult to calculate with high accuracy,[47] a more suitable choice for $\boldsymbol{d}(\boldsymbol{r})$ can be obtained by searching for an origin which causes $\boldsymbol{J}_{\mathrm{p}}^{\boldsymbol{B}}$ to vanish everywhere. The respective *Ansatz* leads to a contradiction which is resolved by setting to zero only the two components of $\boldsymbol{J}_{\mathrm{p}}^{\boldsymbol{B}}$ that are perpendicular to the inducing magnetic field. This variant of the method was termed CTOCD-PZ1, after paramagnetic zero.[49, 50]

Within the CTOCD-PZ1 approach, a shift function $\boldsymbol{d}(\boldsymbol{r})$ is sought such that the

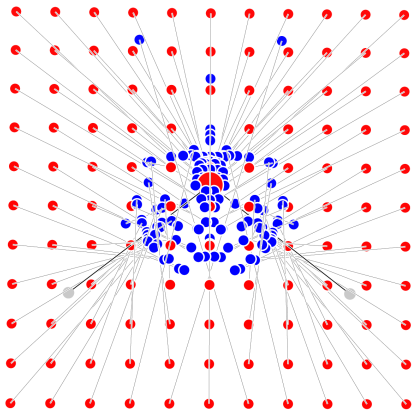

Figure 3.2: The $\boldsymbol{d}(\boldsymbol{r})$ function for H_2O molecule in the CTOCD-PZ1 approach. See caption 3.1 for details.

paramagnetic contributions to the current density is formally annihilated. The condition is:

$$\mathcal{J}_{\mathrm{p}\alpha}^{B_\beta}\left(\boldsymbol{r}-\boldsymbol{r}'\right) = -\mathcal{J}_{\mathrm{p}\alpha}^{(\boldsymbol{d}\times\boldsymbol{B})_\beta} \tag{3.52}$$

which gives the 3×3 system of linear equations

$$\boldsymbol{M}\boldsymbol{d} = \boldsymbol{T} \tag{3.53}$$

where

$$M_{\delta\beta} = \frac{ne}{m_e}\epsilon_{\alpha\beta\gamma}B_\gamma \int \left[\Psi_a^{(\boldsymbol{d}\times\boldsymbol{B})_\alpha *}\hat{p}_\delta\Psi_a^{(0)} + \Psi_a^{(0)*}\hat{p}_\delta\Psi_a^{(\boldsymbol{d}\times\boldsymbol{B})_\alpha}\right] d\boldsymbol{X}_1 \tag{3.54}$$

$$T_\delta = -\frac{ne}{m_e}B_\alpha \int \left[\Psi_a^{B_\alpha *}\hat{p}_\delta\Psi_a^{(0)} + \Psi_a^{(0)*}\hat{p}_\delta\Psi_a^{B_\alpha}\right] d\boldsymbol{X}_1 \tag{3.55}$$

and the wavefunction $\Psi_a^{(\boldsymbol{d}\times\boldsymbol{B})_\alpha}$ is defined according to

$$\Psi_a^{(\boldsymbol{d}\times\boldsymbol{B})_\alpha} = -\frac{e}{2m_e\hbar}\sum_{j\neq a}\omega_{ja}^{-1}|j\rangle\langle j|\hat{P}_\alpha|a\rangle \tag{3.56}$$

The 3×3 $\boldsymbol{M}$ matrix defined accordingly equation (3.54) is singular, for example, setting $\boldsymbol{B} = B_z\boldsymbol{\epsilon}_3$ its last column vanishes:

$$\boldsymbol{M} = \begin{pmatrix} M_{xx} & M_{xy} & 0 \\ M_{yx} & M_{yy} & 0 \\ M_{zx} & M_{zy} & 0 \end{pmatrix} \tag{3.57}$$

In physical terms, the quantum mechanical paramagnetic current flowing in the direction of $\boldsymbol{B}$ cannot be annihilated. Therefore, a 2×2 subsystem of equations

$$\begin{pmatrix} M_{xx} & M_{xy} \\ M_{yx} & M_{yy} \end{pmatrix} \begin{pmatrix} d_x \\ d_y \end{pmatrix} = \begin{pmatrix} T_x \\ T_y \end{pmatrix} \tag{3.58}$$

is solved, over a grid of points in real space, to determine the components

$$\begin{aligned} d_x &= \frac{T_x M_{yy} - T_y M_{xy}}{M_{xx} M_{yy} - M_{xy} M_{yx}} \\ d_y &= \frac{T_y M_{xx} - T_x M_{yx}}{M_{xx} M_{yy} - M_{xy} M_{yx}} \end{aligned} \tag{3.59}$$

of the shift vector function that annihilates the paramagnetic current over planes perpendicular to $\boldsymbol{B}$. The equations derived are valid for cyclic permutations of x, y, z. The CTOCD-PZ1 shift function is illustrated in Figure (3.2). Thus, within the CTOCD-PZ1 scheme, the transverse current density contains only contributions that are formally diamagnetic:

$$\mathcal{J}_{\alpha}^{B_\beta}(\boldsymbol{r}) = \mathcal{J}_{\mathrm{d}_\alpha}^{B_\beta}(\boldsymbol{r}) + \mathcal{J}_{\mathrm{d}_\alpha}^{(\boldsymbol{d}\times\boldsymbol{B})_\beta}(\boldsymbol{r}) \tag{3.60}$$

Therefore, the transverse PZ1 current density is explicitly origin independent also for approximate electronic wavefunctions, since it depends on the difference $\boldsymbol{r} - \boldsymbol{d}(\boldsymbol{r})$ of two vectors whose origin can arbitrarily be chosen.[51]

3.1.4 CTOCD-PZ2

Similarly to the CTOCD-DZ2 case a CTOCD-PZ2 variant has been proposed, which shifts the origin towards the nearest nucleus. Within the CTOCD-PZ2 approach the $\boldsymbol{d}(\boldsymbol{r})$ function is that provided by the CTOCD-PZ1, then it is moved to the nearest nucleus according to

$$\boldsymbol{d}(\boldsymbol{r}) = \boldsymbol{d}^{PZ1}(\boldsymbol{r}) - \sum_a \left[\boldsymbol{d}^{PZ1}(\boldsymbol{r}) - \boldsymbol{R}_a\right] e^{-\alpha|\boldsymbol{r}-\boldsymbol{R}_a|^4} \tag{3.61}$$

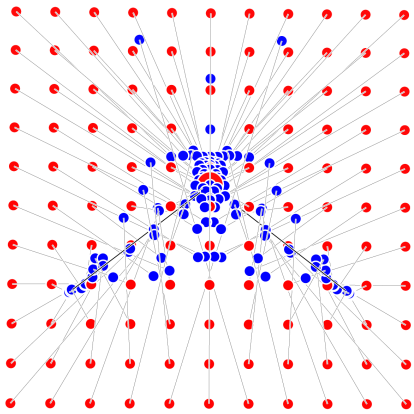

Figure 3.3: The $\boldsymbol{d}(\boldsymbol{r})$ function for H_2O molecule in the CTOCD-PZ2 approach. See caption 3.1 for details.

The CTOCD-PZ2 shift function is illustrated in Figure (3.3). This approach is particularly useful for the calculation of magnetic properties using a small basis set.[52]

3.1.5 CSGT Methods

Recently, a few other choices for $\boldsymbol{d}(\boldsymbol{r})$ have been developed, as for example the CSGT with atomic size adjustments determined using the Bragg-Slater atomic radii or considering the bond critical points of the electron density distribution.[53, 54][**1**]

Within the CSGT-STD approach,[55] available within the Gaussian package[56], the shift function is

$$\boldsymbol{d}(\boldsymbol{r}) = \boldsymbol{r} - \sum_{a=1}^{N} (\boldsymbol{r} - \boldsymbol{R}_a)\, w_a(\boldsymbol{r}) \tag{3.62}$$

where the exponential function of the CTOCD-DZ2/PZ2 variants, see equations (3.48) and (3.61), has been replaced by the normalized nuclear weight function

$$w_a(\boldsymbol{r}) = \frac{P_a(\boldsymbol{r})}{\sum_j P_j(\boldsymbol{r})} \tag{3.63}$$

of the Becke's algorithm.[53] CSGT-STD, CSGT-BS, and CSGT-BCP methods differ in how the cell function $P_a(\boldsymbol{r})$ is determined. Here we give our implementation of the Becke's algorithm, keeping as much as possible the original notation:[53, 54][**1**]

1. Some data required by the algorithm are predetermined such as: (i) a matrix of interatomic distances R_{ij}; (ii) BCP positions are assigned to each pair of bonded atoms; (iii) each element of a matrix of ratios χ_{ij} is set to one.

2. if not CSGT-STD, then only for pairs of bonded atoms i and j:
   (a) $\chi_{ij} = \frac{R_i}{R_j}$, where R_i, R_j are the atomic radii, respectively, of atom i and j for the CSGT-BS method;
   (b) $\chi_{ij} = \frac{D_i}{D_j}$ where D_i,D_j are the distances, respectively, from the internuclear BCP to atom i and j for the CSGT-BCP method.

3. For each atom $i = 1, ..., N$

   (a) set $P_i = 1$

   (b) for each atom $j(\neq i) = 1, ..., N$

      i. set $\mu_{ij} = (r_i - r_j)/R_{ij}$, where r_i and r_j are the distances, respectively, from $\boldsymbol{r}$ to nuclei i and j;
      ii. set $u_{ij} = (\chi_{ij} - 1)/(\chi_{ij} + 1)$
      iii. set $a_{ij} = u_{ij}/\left(u_{ij}^2 - 1\right)$
      iv. adjust $|a_{ij}| \leq \frac{1}{2}$ only for CSGT-BS method
      v. set $v_{ij} = \mu_{ij} + a_{ij}(1 - \mu_{ij}^2)$
      vi. set $f_1 = \text{PolyBecke}(v_{ij})$, where $\text{PolyBecke}(x) = \frac{3}{2}x - \frac{1}{2}x^3$
      vii. set $f_2 = \text{PolyBecke}(f_1)$
      viii. set $f_3 = \text{PolyBecke}(f_2)$
      ix. set $s_3 = \frac{1}{2}(1 - f_3)$
      x. set $P_i = P_i \times s_3$

   (c) next j

   (d) Calculation of the cell function $P_i(\boldsymbol{r}) = \prod_{j \neq i} s(v_{ij})$ is now complete.

4. Next i

When all the cell functions have been determined, we can use them to calculate the origin according to equation (3.62). The differences between the three CSGT methods are illustrated in the following pictures, where it is possible to recognize how the origin is differently chosen for each approach.

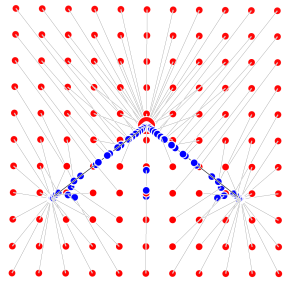

Figure 3.4: The $\boldsymbol{d}(\boldsymbol{r})$ function for H_2O molecule in the CSGT-STD approach. See caption 3.1 for details.

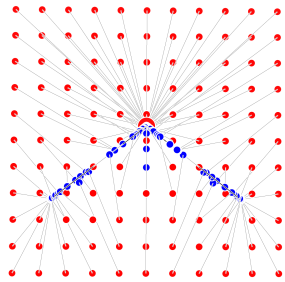

Figure 3.5: The $\boldsymbol{d}(\boldsymbol{r})$ function for H_2O molecule in the CSGT-BS approach. See caption 3.1 for details.

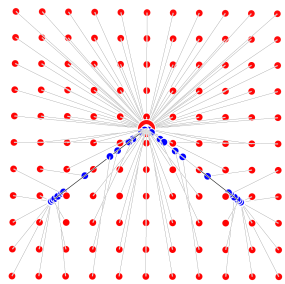

Figure 3.6: The $\boldsymbol{d}(\boldsymbol{r})$ function for H_2O molecule in the CSGT-BCP approach. See caption 3.1 for details.

3.1.6 About the Translational Invariance of the Current Density

The aim of this section is to illustrate some aspects of the translational invariance of the total CTOCD current density tensor and related consequences on the continuity and charge-current conservation. We start proving the condition

$$\mathcal{J}_{\mathrm{p}_\alpha}^{(\boldsymbol{d}\times\boldsymbol{B})_\beta}(\boldsymbol{r}) = -\mathcal{J}_{\mathrm{d}_\alpha}^{(\boldsymbol{d}\times\boldsymbol{B})_\beta}(\boldsymbol{r}) \tag{3.64}$$

for any shift function $\boldsymbol{d}(\boldsymbol{r})$. We rewrite equations (3.41) and (3.42) as

$$\begin{aligned}\mathcal{J}_{\mathrm{p}_\alpha}^{(\boldsymbol{d}\times\boldsymbol{B})_\beta}(\boldsymbol{r}) &= -\frac{ne^2}{2m_{\mathrm{e}}^2\hbar}\epsilon_{\beta\gamma\delta}d_\gamma(\boldsymbol{r})\sum_{j\neq a}\frac{1}{\omega_{ja}} \\ &\quad\times\Re\left\{\left\langle a\left|\hat{P}_\delta\right|j\right\rangle\int\Psi_j^{(0)*}(\boldsymbol{r},\boldsymbol{X}_1)\,\hat{p}_\alpha\Psi_a^{(0)}(\boldsymbol{r},\boldsymbol{X}_1)\,d\boldsymbol{X}_1\right. \\ &\quad\left.+\int\Psi_a^{(0)*}(\boldsymbol{r},\boldsymbol{X}_1)\,\hat{p}_\alpha\Psi_j^{(0)}(\boldsymbol{r},\boldsymbol{X}_1)\,d\boldsymbol{X}_1\left\langle j\left|\hat{P}_\delta\right|a\right\rangle\right\} \qquad (3.65)\\ \mathcal{J}_{\mathrm{d}_\alpha}^{(\boldsymbol{d}\times\boldsymbol{B})_\beta}(\boldsymbol{r}) &= \frac{e^2}{2m_{\mathrm{e}}}\epsilon_{\alpha\beta\gamma}d_\gamma(\boldsymbol{r})\gamma^{(0)}(\boldsymbol{r}) \qquad (3.66)\end{aligned}$$

Considering off-diagonal hypervirial relationships

$$\left\langle a\left|\hat{R}_\alpha\right|j\right\rangle = \frac{\mathrm{i}}{m_{\mathrm{e}}\omega_{ja}}\left\langle a\left|\hat{P}_\alpha\right|j\right\rangle \tag{3.67}$$

$$\left\langle j\left|\hat{R}_\alpha\right|a\right\rangle = -\frac{\mathrm{i}}{m_{\mathrm{e}}\omega_{ja}}\left\langle j\left|\hat{P}_\alpha\right|a\right\rangle \tag{3.68}$$

and

$$\Re\left(a+\mathrm{i}b\right) = a \qquad \Im\left(a+\mathrm{i}b\right) = b \tag{3.69}$$

$$\Im\left[\mathrm{i}\left(a+\mathrm{i}b\right)\right] = a \qquad \Im\left[\mathrm{i}\left(a+\mathrm{i}b\right)\right] = \Re\left(a+\mathrm{i}b\right) \tag{3.70}$$

$$\Re\left[\mathrm{i}\left(a+\mathrm{i}b\right)\right] = -b \qquad \Re\left[\mathrm{i}\left(a+\mathrm{i}b\right)\right] = -\Im\left(a+\mathrm{i}b\right) \tag{3.71}$$

equation (3.65) can be rewritten as

$$\begin{aligned}\mathcal{J}_{\mathrm{p}_\alpha}^{(\boldsymbol{d}\times\boldsymbol{B})_\beta}(\boldsymbol{r}) = -\frac{ne^2}{2m_{\mathrm{e}}\hbar}\epsilon_{\beta\gamma\delta}d_\gamma(\boldsymbol{r})\sum_{j\neq a}\Im\Big\{&\left\langle a\left|\hat{R}_\delta\right|j\right\rangle\int\Psi_j^{(0)*}(\boldsymbol{r},\boldsymbol{X}_1)\,\hat{p}_\alpha\Psi_a^{(0)}(\boldsymbol{r},\boldsymbol{X}_1)\;d\boldsymbol{X}_1 \\ &-\int\Psi_a^{(0)*}(\boldsymbol{r},\boldsymbol{X}_1)\,\hat{p}_\alpha\Psi_j^{(0)}(\boldsymbol{r},\boldsymbol{X}_1)\;d\boldsymbol{X}_1\left\langle j\left|\hat{R}_\delta\right|a\right\rangle\Big\}\end{aligned} \tag{3.72}$$

and is easily recast in the following form

$$\begin{aligned}\mathcal{J}_{\mathrm{p}_\alpha}^{(\boldsymbol{d}\times\boldsymbol{B})_\beta}(\boldsymbol{r}) = -\frac{ne^2}{2m_{\mathrm{e}}\hbar}\epsilon_{\beta\gamma\delta}d_\gamma(\boldsymbol{r})\Im\Big\{&\int\left(\sum_{j\neq a}\Psi_j^{(0)}(\boldsymbol{r},\boldsymbol{X}_1)\left\langle j\left|\hat{R}_\delta\right|a\right\rangle\right)^*\hat{p}_\alpha\Psi_a^{(0)}(\boldsymbol{r},\boldsymbol{X}_1)\,d\boldsymbol{X}_1 \\ &-\int\Psi_a^{(0)*}(\boldsymbol{r},\boldsymbol{X}_1)\,\hat{p}_\alpha\left(\sum_{j\neq a}\Psi_j^{(0)}(\boldsymbol{r},\boldsymbol{X}_1)\left\langle j\left|\hat{R}_\delta\right|a\right\rangle\right)\,d\boldsymbol{X}_1\Big\}\end{aligned} \tag{3.73}$$

Then, if we add and subtract the same quantity, twice in both summations, we have

$$\begin{aligned}\mathcal{J}_{\mathrm{p}_\alpha}^{(\boldsymbol{d}\times\boldsymbol{B})_\beta}(\boldsymbol{r}) = &-\frac{ne^2}{2m_\mathrm{e}\hbar}\epsilon_{\beta\gamma\delta}d_\gamma(\boldsymbol{r})\Im\Bigg\{\int\left(\sum_j\Psi_j^{(0)}\left(\boldsymbol{r},\boldsymbol{X}_1\right)\left\langle j\left|\hat{R}_\delta\right|a\right\rangle\right)^*\hat{p}_\alpha\Psi_a^{(0)}\left(\boldsymbol{r},\boldsymbol{X}_1\right)\,d\boldsymbol{X}_1\\ &-\left\langle a\left|\hat{R}_\delta\right|j\right\rangle\int\Psi_a^{(0)*}\left(\boldsymbol{r},\boldsymbol{X}_1\right)\hat{p}_\alpha\Psi_a^{(0)}\left(\boldsymbol{r},\boldsymbol{X}_1\right)\,d\boldsymbol{X}_1\\ &-\int\Psi_a^{(0)*}\left(\boldsymbol{r},\boldsymbol{X}_1\right)\hat{p}_\alpha\left(\sum_j\Psi_j^{(0)}\left(\boldsymbol{r},\boldsymbol{X}_1\right)\left\langle j\left|\hat{R}_\delta\right|a\right\rangle\right)\,d\boldsymbol{X}_1\\ &+\left\langle j\left|\hat{R}_\delta\right|a\right\rangle\int\Psi_a^{(0)*}\left(\boldsymbol{r},\boldsymbol{X}_1\right)\hat{p}_\alpha\Psi_a^{(0)}\left(\boldsymbol{r},\boldsymbol{X}_1\right)\,d\boldsymbol{X}_1\Bigg\}\end{aligned}\tag{3.74}$$

Using the condition of completeness, the previous equation is rewritten as

$$\begin{aligned}\mathcal{J}_{\mathrm{p}_\alpha}^{(\boldsymbol{d}\times\boldsymbol{B})_\beta}(\boldsymbol{r}) = &-\frac{ne^2}{2m_\mathrm{e}\hbar}\epsilon_{\beta\gamma\delta}d_\gamma(\boldsymbol{r})\Im\Bigg\{\int\Psi_a^{(0)*}\left(\boldsymbol{r},\boldsymbol{X}_1\right)\hat{R}_\delta\hat{p}_\alpha\Psi_a^{(0)}\left(\boldsymbol{r},\boldsymbol{X}_1\right)\,d\boldsymbol{X}_1\\ &-\int\Psi_a^{(0)*}\left(\boldsymbol{r},\boldsymbol{X}_1\right)\hat{p}_\alpha\hat{R}_\delta\Psi_a^{(0)}\left(\boldsymbol{r},\boldsymbol{X}_1\right)\,d\boldsymbol{X}_1\Bigg\}\end{aligned}\tag{3.75}$$

or introducing the commutator, $\left[\hat{R}_\delta,\hat{p}_\alpha\right]$, as

$$\mathcal{J}_{\mathrm{p}_\alpha}^{(\boldsymbol{d}\times\boldsymbol{B})_\beta}(\boldsymbol{r}) = -\frac{ne^2}{2m_\mathrm{e}\hbar}\epsilon_{\beta\gamma\delta}d_\gamma(\boldsymbol{r})\Im\left\{\int\Psi_a^{(0)*}\left(\boldsymbol{r},\boldsymbol{X}_1\right)\left[\hat{R}_\delta,\hat{p}_\alpha\right]\Psi_a^{(0)}\left(\boldsymbol{r},\boldsymbol{X}_1\right)\,d\boldsymbol{X}_1\right\}\tag{3.76}$$

Now, let's focus on the commutator

$$\left[\hat{R}_\delta,\hat{p}_\alpha\right] = \left[\sum_{i=1}^n\hat{r}_{i\delta},\hat{p}_{1\alpha}\right] = [\hat{r}_{1\delta},\hat{p}_{1\alpha}] = \mathrm{i}\hbar\delta_{\delta\alpha}\tag{3.77}$$

Then, we have

$$\mathcal{J}_{\mathrm{p}_\alpha}^{(\boldsymbol{d}\times\boldsymbol{B})_\beta}(\boldsymbol{r}) = -\frac{ne^2}{2m_\mathrm{e}}\epsilon_{\beta\gamma\alpha}d_\gamma(\boldsymbol{r})\int\Psi_a^{(0)*}\left(\boldsymbol{r},\boldsymbol{X}_1\right)\Psi_a^{(0)}\left(\boldsymbol{r},\boldsymbol{X}_1\right)d\boldsymbol{X}_1\tag{3.78}$$

which proves (3.64) since

$$\mathcal{J}_{\mathrm{p}_\alpha}^{(\boldsymbol{d}\times\boldsymbol{B})_\beta}(\boldsymbol{r}) = -\frac{e^2}{2m_\mathrm{e}}\epsilon_{\alpha\beta\gamma}d_\gamma(\boldsymbol{r})\gamma^{(0)} = -\mathcal{J}_{\mathrm{d}_\alpha}^{(\boldsymbol{d}\times\boldsymbol{B})_\beta}(\boldsymbol{r})\tag{3.79}$$

This equality is satisfied only in the complete basis set limit if the state functions are exact eigenfunctions of a model Hamiltonian and therefore satisfy the off-diagonal hypervirial theorem for the position operator, as in HF, DFT or Full-CI approaches.[57, 58][**5**]

Let us consider the following equality, with $f(\boldsymbol{r})$ any real function

$$\int\boldsymbol{\nabla}\cdot\left[f(\boldsymbol{r})\boldsymbol{J}^{\boldsymbol{B}}(\boldsymbol{r})\right]d^3r = \int\boldsymbol{J}^{\boldsymbol{B}}(\boldsymbol{r})\cdot\boldsymbol{\nabla}f(\boldsymbol{r})\,d^3r + \int f(\boldsymbol{r})\boldsymbol{\nabla}\cdot\boldsymbol{J}^{\boldsymbol{B}}(\boldsymbol{r})\,d^3r\tag{3.80}$$

Applying the divergence theorem

$$\int\boldsymbol{J}^{\boldsymbol{B}}(\boldsymbol{r})\cdot\boldsymbol{\nabla}f(\boldsymbol{r})\,d^3r = \underbrace{\oint f(\boldsymbol{r})\boldsymbol{J}^{\boldsymbol{B}}(\boldsymbol{r})\cdot ds}_{=0} - \int f(\boldsymbol{r})\boldsymbol{\nabla}\cdot\boldsymbol{J}^{\boldsymbol{B}}(\boldsymbol{r})\,d^3r\tag{3.81}$$

Then, allowing for the continuity equation

$$\boldsymbol{\nabla} \cdot \boldsymbol{J}^{\boldsymbol{B}}(\boldsymbol{r}) = 0 \tag{3.82}$$

one has that

$$\int \boldsymbol{J}^{\boldsymbol{B}}(\boldsymbol{r}) \cdot \boldsymbol{\nabla} f(\boldsymbol{r})\, d^3r = 0 \tag{3.83}$$

Choosing $f(\boldsymbol{r}) = x, y,$ and z one obtains

$$\int J^{\boldsymbol{B}}_{\alpha}(\boldsymbol{r})\, d^3r = 0 \tag{3.84}$$

which is the Sambe condition for charge and current conservation.[59]

We observe that continuity implies conservation of the current. Further, the origin-independence condition (3.79), for the exact case, permits to reduce the Sambe condition (3.84) to the Arrighini-Maestro-Moccia (AMM) sum rule[60], in which the integrals of the traditional (not shifted) paramagnetic and diamagnetic components equal to

$$\begin{aligned} \int J^{\boldsymbol{B}}_{\mathrm{p}_\alpha}(\boldsymbol{r})\, d^3r &= \frac{e^2}{2m_{\mathrm{e}}^2} \left\{ \hat{P}_\alpha, \hat{L}_\beta \right\}_{-1} B_\beta, \\ \int J^{\boldsymbol{B}}_{\mathrm{d}_\alpha}(\boldsymbol{r})\, d^3r &= -\frac{e^2}{2m_{\mathrm{e}}} \epsilon_{\alpha\beta\gamma} \left\langle a \middle| \hat{R}_\gamma \middle| a \right\rangle B_\beta, \end{aligned} \tag{3.85}$$

where

$$\left\{ \hat{P}_\alpha, \hat{L}_\beta \right\}_{-1} = \frac{1}{\hbar} \sum_{j \neq a} \frac{2}{\omega_{ja}} \Re \left\{ \left\langle a \middle| \hat{P}_\alpha \middle| j \right\rangle \left\langle j \middle| \hat{L}_\beta \middle| a \right\rangle \right\} = m_{\mathrm{e}} \epsilon_{\alpha\beta\gamma} \left\langle a \middle| \hat{R}_\gamma \middle| a \right\rangle \tag{3.86}$$

In an approximate calculation, conditions (3.79) and (3.84) are not fulfilled, even if the CTOCD current densities (all variants) are origin-independent.[51] Therefore the latter do not fulfill the continuity equation and the charge and current conservation, except for symmetry reasons. For example, in Figure (3.7) $\boldsymbol{\nabla} \cdot \boldsymbol{J}^{\boldsymbol{B}}$ is shown for the benzene molecule, where the Sambe condition (3.84) of conservation is fulfilled by symmetry, the current is origin independent, but the divergence, as one can see is not vanishing at all.

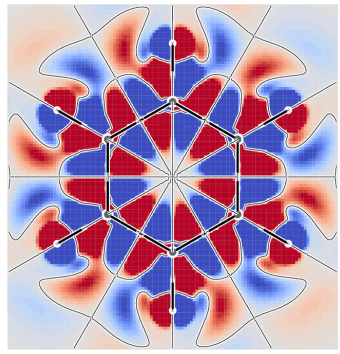

Figure 3.7: Diverging color maps of $\boldsymbol{\nabla} \cdot \boldsymbol{J}^{\boldsymbol{B}}(\boldsymbol{r})$ in benzene calculated at the B972/pc-Sseg-0 level of theory, using the CTOCD-DZ1 method. Red/blue color means positive/negative divergence.

3.2 Symmetry of the MAGIC Density

The electron density $\rho(\boldsymbol{r})$ of a molecule has the same symmetry as the molecule itself, considered as a rigid body in its equilibrium state. Accordingly, we may regard the 32 conventional symmetry classes [61] as mathematical tools which describe the possible point groups symmetry of ρ. In the presence of a static magnetic field an electronic current density is induced, which satisfies two conditions: (a) there must not be sinks or sources in the current density field, because $\boldsymbol{\nabla} \cdot \boldsymbol{J^B}(\boldsymbol{r}) = 0$; (b) there must not be any current leaving the molecular region, thus the integral conservation condition

$$\int \boldsymbol{J^B}(\boldsymbol{r})\, d^3r = 0 \tag{3.87}$$

over the full space should be satisfied. Within a non vanishing current density field, new symmetry transformations are required, which must be regarded as the combination of an operation acting on the geometrical shape of the molecule and another that acts on $\boldsymbol{J^B}$ without altering the space coordinates. An operation peculiar to vector fields is the reversal in direction. In the case of current density this is equivalent to time reversal R, that is, an antiunitary operator which does not affect position, but changes sign of the velocity vector.[62] Thus,

$$R\rho(\boldsymbol{r}) = \rho(\boldsymbol{r}) \qquad R\boldsymbol{J^B}(\boldsymbol{r}) = -\boldsymbol{J^B}(\boldsymbol{r}) \tag{3.88}$$

Since R changes the sign of time, it is a cyclic operator of order $o = 2$, i.e., $R^2 = E$. However R is not a symmetry operation by itself, i.e., it cannot appear alone in any group, since it would imply $\boldsymbol{J^B}(\boldsymbol{r}) = -\boldsymbol{J^B}(\boldsymbol{r})$ at any point $\boldsymbol{r}$. In the presence of current density, R is always combined with other symmetry operations as $P = RQ$, where Q is either a rotation or a reflection. The set of symmetry transformations $\{P\}$ forms a group in the usual mathematical sense. It is called a magnetic group (M hereafter), which is the same as one of Shubnikov color group [63], where the color change is replaced by the time-reversal operator. However, some further restrictions must be considered. Both Q and $P = RQ$ cannot occur in a magnetic group M, since M would then contain Q^{-1} and $PQ^{-1} = RQQ^{-1} = R$, which is not allowed, as stated before. Equally excluded are those $P = RQ$ for which Q is of odd order o, since $P^o = R^oQ^o = RE = R$. It follows that the possibility of RC_3 axes is ruled out. Conversely, RS_3 is an allowed operation. On the basis of these properties an algorithm for finding the groups of point symmetry transformations, in the presence of a magnetic field, can be devised.[64] Take a symmetry class and let elements $\{Q_1, Q_2, \ldots, Q_g\}$ to form the group G. Consider a subgroup H of elements $\{Q_i\}$ among the elements of G, which also belong to one of the 32 symmetry classes. Multiply by R all elements of $G - H$, i.e., all those belonging to G but not to H, to obtain $P_k = RQ_k$. If the set of element $Q_i \in H$ and $P_k = RQ_k$ ($Q_k \in G - H$) form a group, then this is one of the possible groups searched for. The proposed algorithm is quite laborious to apply. A theorem that makes the search easier has been proven by Tavger and Zaitsev.[64] Accordingly, let H be a subgroup of G, then a necessary and sufficient condition for the elements $Q_i \in H$ and elements $P_k = RQ_k$ ($Q_k \in G - H$) to form a group is that H is of index 2 in G. Then, the following Tavger-Zaitsev algorithm follows:[64]

1. the groups of point transformations in the presence of a magnetic field will contain in the first place the 32 conventional symmetry classes;

2. to find all the others, select a subgroup $H \equiv \{Q_i\}$ of index 2 in G;

3. form the set $G - H$ of operators $\{Q_k\}$;

4. construct $R\{G - H\}$, consisting of $\{P_k\} = \{RQ_k\}$;

5. obtain the magnetic group M as $H + R\{G - H\}$, consisting of $\{Q_i, P_k\}$.

Altogether, there are 90 classes of point symmetry transformations with a non vanishing current density; of these 32 coincide with the 32 conventional symmetry classes and 58 are new. Within the Schönflies notation, a magnetic group can be given a symbol that makes explicit the H subgroup of index 2 used in the TZ algorithm, i.e., $M(H)$. Some interesting features of the current density field are a direct consequence of the magnetic group symmetry:

(i) a σ_h plane cannot be crossed by the streamlines of the current density;

(ii) $R\sigma_v$ and $R\sigma_d$ planes can be crossed only by streamlines perpendicular to them. If a trajectory approaches $R\sigma$ planes to an angle different from 90°, it is scattered away, and the phase portrait of a saddle is observed;

(iii) vortex or saddle stagnation lines, i.e., (2,0) manifolds, may lie on, but not pass through, an $R\sigma$;

(iv) quite frequently stagnation lines are fully contained in $R\sigma$ planes;

(v) in the absence of $R\sigma$ planes, with rare exceptions, the stagnation graphs contain only isolated singularities;

(vi) C_n symmetry axes, parallel to the inducing magnetic field and lying on $R\sigma_v$ planes, are necessarily (2,0) stagnation lines.

3.3 Topological Analysis and Stagnation Graph of the MAGIC Density

In this section some of the tools needed to deal with vectorial fields and in particular with the current density vector field $\boldsymbol{J}(\boldsymbol{r})$ will be recalled in analogy to the topological analysis of the electron charge density. In particular a description of trajectories as streamlines and stagnation graphs (SG) is given. Within classical hydrodynamics the differential equations for the velocity vector field $\boldsymbol{v}$ are

$$\boldsymbol{v} = \frac{d\boldsymbol{r}}{dt} \quad \frac{dx}{v_x} = \frac{dy}{v_y} = \frac{dz}{v_z} \tag{3.89}$$

where t is time. Similar equations can be written for the trajectories of the stationary field $\boldsymbol{J} = \rho\boldsymbol{v}$, which defines a field parallel to the velocity. The streamlines of the current density vector field $\boldsymbol{J}(\boldsymbol{r})$ are determined as solutions of the real autonomous system of differential equations

$$\boldsymbol{J}(\boldsymbol{r}) = \frac{d\boldsymbol{r}}{d\tau} \tag{3.90}$$

where the derivatives $dx/d\tau$, $dy/d\tau$ and $dz/d\tau$ have been arranged in a column vector, and τ is any convenient coordinate along the trajectory. A (time) arrow is used in the maps to indicate the direction of the current. Equation (3.90) can be rewritten in the form

$$\frac{dx}{J_x} = \frac{dy}{J_y} = \frac{dz}{J_z} \tag{3.91}$$

which characterizes a deterministic problem: one and only one trajectory passes through any nonsingular point of the vector field. The solution to (3.91) is easily arrived at by well-known numerical procedures, e.g. Euler and Runge–Kutta integration, in the regions of space where $\boldsymbol{J}^{\boldsymbol{B}}$ does not vanish. Trajectories of the induced current density are plotted in magenta in the following maps. The induced current density $J_\alpha^{\boldsymbol{B}}(\boldsymbol{r}) = \mathcal{J}_\alpha^{B_\beta}(\boldsymbol{r})B_\beta$ is a three-dimensional vector field, which has a topological structure determined by its stagnation points, i.e., singularities, where the current density vector field vanishes.[65–67] The ensemble of all isolated points $\boldsymbol{r}$ and lines at which $J_\alpha^{\boldsymbol{B}}(\boldsymbol{r}) = 0$ is termed the stagnation graph of the current density. A convenient way for searching and characterizing stagnation points is a Newton-Raphson based procedure, albeit other methods have also been proposed.[68] In the vicinity of a singularity at $\boldsymbol{r}_0$ the current density field can be described by the Taylor series expansion

$$J_\alpha^{\boldsymbol{B}}(\boldsymbol{r}) = (r_\beta - r_{0\beta}) \left(\nabla_\beta J_\alpha^{\boldsymbol{B}}\right)_{\boldsymbol{r}_0} + \frac{1}{2}(r_\beta - r_{0\beta})(r_\gamma - r_{0\gamma}) \left(\nabla_\beta \nabla_\gamma J_\alpha^{\boldsymbol{B}}\right)_{\boldsymbol{r}_0} + \cdots \tag{3.92}$$

then, dropping all non linear terms and setting the current density vector components to zero, one has

$$\boldsymbol{J}^{\boldsymbol{B}}(\boldsymbol{r}_2) \approx \boldsymbol{J}^{\boldsymbol{B}}(\boldsymbol{r}_1) + \left(\boldsymbol{\nabla}\boldsymbol{J}^{\boldsymbol{B}}\right)_{\boldsymbol{r}_1} (\boldsymbol{r}_2 - \boldsymbol{r}_1) = \boldsymbol{0} \tag{3.93}$$

Starting from a grid of arbitrarily chosen points $\boldsymbol{r}_1$, the following loop (vector components by column)

$$
\begin{aligned}
&n = 0;\\
&\text{while } \left(\left|\boldsymbol{J}^{\boldsymbol{B}}(\boldsymbol{r}_1)\right| > \epsilon \text{ and } n < \text{NMAX}\right)\{ \quad n = n + 1;\\
&\quad \boldsymbol{g} = \left(\boldsymbol{\nabla} \boldsymbol{J}^{\boldsymbol{B}}\right)_{\boldsymbol{r}_1}; \quad \boldsymbol{t} = -\boldsymbol{J}^{\boldsymbol{B}}(\boldsymbol{r}_1);\\
&\quad \boldsymbol{r}_2 = \boldsymbol{r}_1 + \boldsymbol{g}^{-1}\boldsymbol{t}; \quad \boldsymbol{r}_1 = \boldsymbol{r}_2;\\
&\}
\end{aligned}
$$

is repeated until the current density modulus is found smaller than a certain minimum threshold ϵ, or a maximum number of steps NMAX has been employed. At the end of each successful search, one determines the Jacobian matrix, whose eigenvalues ξ_1, ξ_2, ξ_3 (eigenvectors $\boldsymbol{v}_1, \boldsymbol{v}_2, \boldsymbol{v}_3$) permit to characterize the singularity according to the widely adopted Euler index, in terms of (*rank*, *signature*).[65–67, 69] The rank r is defined as the number of non-vanishing eigenvalues of the Jacobian matrix. The signature s is the excess of eigenvalues with a positive real part over a negative real part. The continuity equation $\nabla_\alpha J^{\boldsymbol{B}}_\alpha = 0$ implies that $\xi_1 + \xi_2 + \xi_3 = 0$, which poses a limit on the possible (r, s). Adopting a conventional nomenclature[34], the allowed cases are as follows:

- $(3, \pm 1)$ points correspond to isolated singularities. The eigenvalues satisfy the condition $\xi_3 = -\Re(\xi_1 + \xi_2)$. If ξ_1 and ξ_2 are real then a node or a saddle is observed in the phase portrait of the flow over the plane of the eigenvectors $\boldsymbol{v}_1$ and $\boldsymbol{v}_2$. If ξ_1 and ξ_2 are complex conjugate, a focus is found.

- $(2, 0)$ points belong to stagnation lines, $\xi_3 = 0$ and $\xi_1 = -\xi_2$. If $\xi_{1,2}$ are real (pure imaginary) the phase portrait of a saddle (vortex) is observed. In the case of a saddle, the corresponding eigenvectors $\boldsymbol{v}_1$ and $\boldsymbol{v}_2$ are real and give the direction of the asymptotes through the singularity. In the case of a vortex, the two eigenvectors are complex conjugate. Saddle and vortex stagnation lines are continuous manifolds of $(2, 0)$ points. The eigenvector $\boldsymbol{v}_3$ is locally tangent to the stagnation line, which can be an open line, as in the case of an axial vortex, or form a close loop, as in the case of a toroidal vortex.

- $(0, 0)$ points correspond to transition singularities at which *branching* of stagnation lines may occur, with eigenvalues $\xi_3 = \xi_1 = \xi_2 = 0$. From a mathematical point of view, these points correspond to a transition between pure imaginary and pure real eigenvalues.

The direction of flow about a singularity, a focus or vortex in particular, is determined by the vorticity, i.e., by the local curl $\left(\boldsymbol{\nabla} \times \boldsymbol{J}^{\boldsymbol{B}}\right)_{\boldsymbol{r}_0}$, which corresponds to the non null elements of antisymmetric component of the Jacobian matrix.[67] Stagnation graphs for several molecules of interest can be found in the literature.[67, 69–74] In order to distinguish all kinds of stagnation points (SP), different symbols and colors will be used in the maps according to the following code: (0,0) branching points are marked with magenta dots; isolated (3,±1) and (2,0) points belonging to vortical lines are indicated by a red/green dot if $\left(\boldsymbol{\nabla} \times \boldsymbol{J}^{\boldsymbol{B}}\right)_{\boldsymbol{r}_0} \cdot \boldsymbol{B}$ is positive/negative; (2,0) saddle lines are denoted by a sequence of blue dots; isolated (3,±1) saddle-node points are marked using 3-dash crosses, one dash for each eigenvalue ξ_i, parallel to the corresponding eigenvector $\boldsymbol{v}_i$ and coloured in blue/red if ξ_i is positive/negative. In practice, SGs can be determined searching for singularities over planes perpendicular to the inducing magnetic field, neglecting

the component of the current density parallel to $\boldsymbol{B}$. Repeating the search for many contiguous planes, a pseudo-SG is obtained, which contains the true SG plus a number of additional points. The latter can be easily eliminated checking whether the modulus of the current calculated using all the vector components is less then the minimum search threshold. However, pseudo-SGs are very useful and have their own conceptual value.[75, 76] A simple spatial model of vector field, defined by three equations for the current density components, describing trajectories everywhere parallel to the xy plane, has been proposed by Gomes[66] to illustrate the notion of SG and the associated idea of a separatrix as a closed boundaryless surface encasing a vortex and separating it from other domains of $\boldsymbol{J^B}$. A separatrix cannot be crossed by any trajectory, it is filled with asymptotic current lines which may start and finish at singular (0,0) branching points, as found for the Gomes model,[77] or for molecules.[76] Separatrices represented by the surface of a topological sphere contain poloidal currents flowing on the surface of a torus, and connecting $(3, \pm 1)$ singularities.

Another tool that can be used to characterize the topology of a vectorial field is the Poincaré index, that is also known as Poincaré–Hopf index formula. Here for the sake of simplicity we report only an extrapolation of the mathematical definition given in Ref. [78]. Let $\boldsymbol{X}$ be a vector field on the manifold M. A critical point of $\boldsymbol{X}$ is a point x_0 at which $\boldsymbol{X}$ vanishes

$$\boldsymbol{X}(x_0) = \boldsymbol{0} \tag{3.94}$$

In any coordinate system surrounding x_0 the Jacobian matrix of $\boldsymbol{X}$ is

$$\boldsymbol{J}(x_0) = \left[\left(\frac{\partial X^i}{\partial x^k} \right)_{x_0} \right] \tag{3.95}$$

The eigenvalues of this matrix do not depend on the coordinate system. The critical point is called hyperbolic if none of its eigenvalues has zero real part. Since the Jacobian matrix is real, then the characteristic exponents occur in complex conjugate pairs. If x_0 is a hyperbolic critical point of $\boldsymbol{X}$, the number of eigenvalues (counting multiplicities) with negative real part is called the *index* of x_0. The Poincaré-Hopf index theorem states that if M is compact and the vector field $\boldsymbol{X}$ only has (isolated) critical points, then the number of critical points is finite and

$$\sum_i \mathrm{index}_{x_i}(\boldsymbol{X}) = \chi(M) \tag{3.96}$$

where $\chi(M)$ is the Euler characteristic of M.

CHAPTER 4

Time-Dependent Perturbations

In this chapter expressions for the polarization charge and current densities induced in the electron cloud of a molecule by a monochromatic plane wave will be briefly recalled using the time-dependent quantum mechanical perturbation theory.[79] As usual, let us consider that the eigenvalue problem for the time-independent Born Oppenheimer electronic Hamiltonian

$$\hat{H}^{(0)}\Psi_j^{(0)} = E_j^{(0)}\Psi_j^{(0)} \tag{4.1}$$

has been solved, determining a set of eigenfunctions $\Psi_j^{(0)}$ and corresponding energy eigenvalues $E_j^{(0)}$. The reference (ground) non-degenerate state is indicated by $\Psi_a^{(0)}$. Let us denote with $\hat{H}^{(1)}$ the first order correction to $\hat{H}^{(0)}$ that satisfies the general requirement[80]

$$\hat{H}^{(1)}(\boldsymbol{r}, t \to -\infty) = \hat{0} \tag{4.2}$$

and that depends explicitly on time according to

$$\hat{H}^{(1)}(\boldsymbol{r}, t) = \hat{\mathcal{H}}^{(1)}(\boldsymbol{r})\cos(\omega t) \tag{4.3}$$

Then, the Schrödinger equation reads

$$\mathrm{i}\hbar\frac{\partial\Phi_a}{\partial t} = \left[\hat{H}^{(0)} + \hat{H}^{(1)}\right]\Phi_a \tag{4.4}$$

Conventionally, within the Schrödinger picture, the perturbed wave function Φ_a is expressed as a linear combination

$$\Phi_a = \sum_{b=0}^{\infty} c_b(t)\Theta_b(t) \tag{4.5}$$

of stationary states $\Theta_b(t)$

$$\Theta_b(t) = \Psi_b^{(0)} e^{-\frac{\mathrm{i}}{\hbar}E_b^{(0)}t} \tag{4.6}$$

with coefficients c_b depending on time. Substituting the previous expression in (4.4) one has

$$\mathrm{i}\hbar\sum_{b=0}^{\infty}\frac{d}{dt}\left[c_b(t)\Psi_b^{(0)}e^{-\frac{\mathrm{i}}{\hbar}E_b^{(0)}t}\right]=\left[\hat{H}^{(0)}+\hat{H}^{(1)}\right]\sum_{b=0}^{\infty}c_b(t)\Psi_b^{(0)}e^{-\frac{\mathrm{i}}{\hbar}E_b^{(0)}t} \tag{4.7}$$

from which it follows

$$\begin{aligned}\mathrm{i}\hbar\sum_{b=0}^{\infty}\frac{d}{dt}\left[c_b(t)\Psi_b^{(0)}e^{-\frac{\mathrm{i}}{\hbar}E_b^{(0)}t}\right]&=\sum_{b=0}^{\infty}c_b(t)\hat{H}^{(0)}\Psi_b^{(0)}e^{-\frac{\mathrm{i}}{\hbar}E_b^{(0)}t}\\&+\sum_{b=0}^{\infty}c_b(t)\hat{H}^{(1)}\Psi_b^{(0)}e^{-\frac{\mathrm{i}}{\hbar}E_b^{(0)}t}\end{aligned} \tag{4.8}$$

Now, using equation (4.1) we obtain

$$\begin{aligned}\mathrm{i}\hbar\sum_{b=0}^{\infty}\frac{d}{dt}\left[c_b(t)\Psi_b^{(0)}e^{-\frac{\mathrm{i}}{\hbar}E_b^{(0)}t}\right]&=\sum_{b=0}^{\infty}c_b(t)E_b^{(0)}\Psi_b^{(0)}e^{-\frac{\mathrm{i}}{\hbar}E_b^{(0)}t}\\&+\sum_{b=0}^{\infty}c_b(t)\hat{H}^{(1)}\Psi_b^{(0)}e^{-\frac{\mathrm{i}}{\hbar}E_b^{(0)}t}\end{aligned} \tag{4.9}$$

The l.h.s of the above equation can be rearranged as

$$\mathrm{i}\hbar\frac{d}{dt}\left[c_b(t)\Psi_b^{(0)}e^{-\frac{\mathrm{i}}{\hbar}E_b^{(0)}t}\right]=\mathrm{i}\hbar\frac{dc_b(t)}{dt}\Psi_b^{(0)}e^{-\frac{\mathrm{i}}{\hbar}E_b^{(0)}t}+c_b(t)E_b^{(0)}\Psi_b^{(0)}e^{-\frac{\mathrm{i}}{\hbar}E_b^{(0)}t} \tag{4.10}$$

from which it follows that (4.9) reduces to

$$\mathrm{i}\hbar\sum_{b=0}^{\infty}\frac{dc_b(t)}{dt}\Psi_b^{(0)}e^{-\frac{\mathrm{i}}{\hbar}E_b^{(0)}t}=\sum_{b=0}^{\infty}c_b(t)\hat{H}^{(1)}\Psi_b^{(0)}e^{-\frac{\mathrm{i}}{\hbar}E_b^{(0)}t} \tag{4.11}$$

Multiplying the previous equation by $\Psi_j^{(0)*}$, and integrating both sides with respect to space and spin coordinates, one has

$$\mathrm{i}\hbar\sum_{b=0}^{\infty}\frac{dc_b(t)}{dt}\left\langle\Psi_j^{(0)}|\Psi_b^{(0)}\right\rangle e^{-\frac{\mathrm{i}}{\hbar}E_b^{(0)}t}=\sum_{b=0}^{\infty}c_b(t)\left\langle\Psi_j^{(0)}\left|\hat{H}^{(1)}\right|\Psi_b^{(0)}\right\rangle e^{-\frac{\mathrm{i}}{\hbar}E_b^{(0)}t} \tag{4.12}$$

Using the orthonormalization condition of the unperturbed wave functions, and then multiplying by $-\frac{\mathrm{i}}{\hbar}e^{\frac{\mathrm{i}}{\hbar}E_j^{(0)}t}$ one gets

$$\frac{dc_j(t)}{dt}=-\frac{\mathrm{i}}{\hbar}\sum_{b=0}^{\infty}c_b(t)\left\langle\Psi_j^{(0)}\left|\hat{H}^{(1)}\right|\Psi_b^{(0)}\right\rangle e^{\mathrm{i}\omega_{jb}t} \tag{4.13}$$

where $\omega_{jb}=\left(E_j^{(0)}-E_b^{(0)}\right)/\hbar$ are the natural transition frequencies. As it is very well known equation (4.13) corresponds to the matrix formulation of the time-dependent Schrödinger equation. The time-dependent coefficients are obtained by a perturbation expansion

$$c_b(t)=c_b^{(0)}(t)+\lambda c_b^{(1)}(t)+\lambda^2c_b^{(2)}(t)+\cdots \tag{4.14}$$

with the requirements[80]

$$c_b^{(0)}(t) = \delta_{ba} \tag{4.15}$$

$$c_b^{(l)}(t\to-\infty) = 0,\quad l\neq 0 \tag{4.16}$$

Using the last expansion in equation (4.13) and considering that according to perturbation theory λ appears also as a factor multiplying $\hat{H}^{(1)}$ we get

$$\frac{d}{dt}[c_j^{(0)}(t)+\lambda c_j^{(1)}(t)+\cdots]=-\frac{\mathrm{i}}{\hbar}\sum_{b=0}^{\infty}[c_b^{(0)}(t)+\lambda c_b^{(1)}(t)+\cdots]\left\langle \Psi_j^{(0)}\left|\lambda\hat{H}^{(1)}\right|\Psi_b^{(0)}\right\rangle e^{\mathrm{i}\omega_{jb}t} \tag{4.17}$$

The equality holds for each power of λ, so we get

$$\dot{c}_j^{(0)}(t) = 0 \tag{4.18}$$

$$\dot{c}_j^{(1)}(t) = -\frac{\mathrm{i}}{\hbar}\sum_{b=0}^{\infty}c_b^{(0)}(t)\left\langle \Psi_j^{(0)}\left|\hat{H}^{(1)}\right|\Psi_b^{(0)}\right\rangle e^{\mathrm{i}\omega_{jb}t} \tag{4.19}$$

$$\vdots$$

$$\dot{c}_j^{(l)}(t) = -\frac{\mathrm{i}}{\hbar}\sum_{b=0}^{\infty}c_b^{(l-1)}(t)\left\langle \Psi_j^{(0)}\left|\hat{H}^{(1)}\right|\Psi_b^{(0)}\right\rangle e^{\mathrm{i}\omega_{jb}t} \tag{4.20}$$

with $\dot{c}_j=\frac{d}{dt}c_j$. Starting from equation (4.20) and using the requirement (4.15) one finds

$$c_j^{(1)}(t)=-\frac{\mathrm{i}}{\hbar}\left\langle j|\hat{\mathcal{H}}^{(1)}|a\right\rangle\int_{-\infty}^{t}e^{\mathrm{i}\omega_{ja}t'}\cos\omega t'dt'\equiv c_{ja}(t) \tag{4.21}$$

where $|j\rangle\equiv|\Psi_j^{(0)}\rangle$. The integral is calculated by parts, allowing for the assumption (4.2) and equation (4.3), see, for instance Ref. [81],

$$\int_{-\infty}^{t}e^{\mathrm{i}\omega_{ja}t'}\cos\omega t'dt'=-\frac{e^{\mathrm{i}\omega_{ja}t}}{(\omega_{ja}^2-\omega^2)}(\omega\sin\omega t+\mathrm{i}\omega_{ja}\cos\omega t) \tag{4.22}$$

It can be argued that an alternative, and possibly more rigorous, calculation of integral (4.22) would require the use of a convergence factor,[82] since the integrand function keeps oscillating for $t\to-\infty$. At any rate, we can assume that the integral is multiplied by $\hat{\mathcal{H}}^{(1)}$, relying on equation (4.3). Thus, owing to equation (4.2),

$$c_{ja}(t)=-\frac{e^{\mathrm{i}\omega_{ja}t}}{\hbar(\omega_{ja}^2-\omega^2)}\left[\left\langle j\left|\hat{H}^{(1)}\right|a\right\rangle\omega_{ja}+\mathrm{i}\left\langle j\left|\hat{\dot{H}}^{(1)}\right|a\right\rangle\right] \tag{4.23}$$

with

$$\hat{\dot{H}}^{(1)}=\frac{\partial}{\partial t}\hat{H}^{(1)}$$

The zero- and first-order perturbed wave functions are given by the expressions

$$\Phi_a^{(0)} \equiv \Theta_a=\Psi_a^{(0)}e^{-\frac{\mathrm{i}}{\hbar}E_a^{(0)}t} \tag{4.24}$$

$$\Phi_a^{(1)} = -\frac{1}{\hbar}\sum_{j\neq a}(\omega_{ja}^2-\omega^2)^{-1}\left[\left\langle k\left|\hat{H}^{(1)}\right|a\right\rangle\omega_{ka}+\mathrm{i}\left\langle k\left|\hat{\dot{H}}^{(1)}\right|a\right\rangle\right]e^{-\frac{\mathrm{i}}{\hbar}E_a^{(0)}t} \tag{4.25}$$

then the first-order perturbed electron charge density is written in the form

$$\rho^{(1)}(\boldsymbol{r},t)=-ne\int\left[\Phi_a^{(0)}(\boldsymbol{r},\boldsymbol{X}_1)\Phi_a^{(1)*}(\boldsymbol{r},\boldsymbol{X}_1)+\Phi_a^{(1)}(\boldsymbol{r},\boldsymbol{X}_1)\Phi_a^{(0)*}(\boldsymbol{r},\boldsymbol{X}_1)\right]d\boldsymbol{X}_1 \tag{4.26}$$

A non-Larmor contribution to the electron current density is given by the relation

$$\boldsymbol{J}^{(1)}(\boldsymbol{r},t) = -\frac{ne}{m_{\mathrm{e}}}\int \Re\left[\Phi_a^{(0)}(\boldsymbol{r},\boldsymbol{X}_1)\hat{\boldsymbol{p}}\,\Phi_a^{(1)*}(\boldsymbol{r},\boldsymbol{X}_1) + \Phi_a^{(1)}(\boldsymbol{r},\boldsymbol{X}_1)\hat{\boldsymbol{p}}\,\Phi_a^{(0)*}(\boldsymbol{r},\boldsymbol{X}_1)\right] d\boldsymbol{X}_1 \tag{4.27}$$

with $\hat{\boldsymbol{p}} = -\mathrm{i}\hbar\boldsymbol{\nabla}$. Introducing the expressions for $\Phi_a^{(0)}$ and $\Phi_a^{(1)}$ we write the first-order charge polarization density induced by the electromagnetic perturbation within the electron cloud as[83]

$$\begin{aligned}\rho^{(1)}(\boldsymbol{r},t) &= \frac{2ne}{\hbar}\sum_{j\neq a}\left(\omega_{ja}^2-\omega^2\right)^{-1}\Re\left\{\left[\omega_{ja}\left\langle a\left|\hat{H}^{(1)}\right|j\right\rangle - \mathrm{i}\left\langle a\left|\hat{\dot{H}}\right|j\right\rangle\right]\right.\\ &\left.\times\int \Psi_j^{(0)*}(\boldsymbol{r},\boldsymbol{X}_1)\,\Psi_a^{(0)}(\boldsymbol{r},\boldsymbol{X}_1)\,d\boldsymbol{X}_1\right\}\end{aligned} \tag{4.28}$$

and the first order induced dynamic current density vector as[83]

$$\begin{aligned}\boldsymbol{J}^{(1)}(\boldsymbol{r},t) &= \frac{ne}{m_{\mathrm{e}}\hbar}\sum_{j\neq a}\left(\omega_{ja}^2-\omega^2\right)^{-1}\Re\left\{\left[\left\langle a\left|\hat{H}^{(1)}\right|j\right\rangle\omega_{ja} - \mathrm{i}\left\langle a\left|\hat{\dot{H}}^{(1)}\right|j\right\rangle\right]\right.\\ &\times\int \Psi_j^{(0)*}(\boldsymbol{r},\boldsymbol{X}_1)\,\hat{\boldsymbol{p}}\Psi_a^{(0)}(\boldsymbol{r},\boldsymbol{X}_1)\,d\boldsymbol{X}_1\\ &+\int \Psi_a^{(0)*}(\boldsymbol{r},\boldsymbol{X}_1)\,\hat{\boldsymbol{p}}\Psi_j^{(0)}(\boldsymbol{r},\boldsymbol{X}_1)\,d\boldsymbol{X}_1\\ &\left.\times\left[\left\langle j\left|\hat{H}^{(1)}\right|a\right\rangle\omega_{ja} + \mathrm{i}\left\langle j\left|\hat{\dot{H}}^{(1)}\right|a\right\rangle\right]\right\}\end{aligned} \tag{4.29}$$

The first order induced current density vector contains also a Larmor term that is the same appearing in the static case (see chapter 3 for the derivation)

$$\boldsymbol{J}_d^{\boldsymbol{B}}(\boldsymbol{r},t) = -\frac{e^2}{2m_{\mathrm{e}}}\boldsymbol{B}(\omega,t)\times\boldsymbol{r}\gamma^{(0)}(\boldsymbol{r}) \tag{4.30}$$

Eventually, we recall that the problem (4.4) discussed above is given an alternative, formally easier, solution within the framework of Dirac's interaction picture,[80] introducing the operator[84]

$$\hat{\mathcal{R}} = e^{\frac{\mathrm{i}}{\hbar}\hat{H}^{(0)}t} \tag{4.31}$$

which brings the stationary states (4.6) to rest, consistently transforming the Hamiltonian,

$$\hat{\mathcal{R}}\Theta_j = \Psi_j^{(0)}, \quad \hat{H}^{(1)}(\boldsymbol{r},t) \to \hat{H}_I^{(1)}(\boldsymbol{r},t) = \hat{\mathcal{R}}\hat{H}^{(1)}\hat{\mathcal{R}}^\dagger. \tag{4.32}$$

Within this approach, one obtains a general expression for the differential "equation of motion" in the I picture,

$$\hat{H}_I^{(1)}\Phi_I = \mathrm{i}\hbar\frac{\partial}{\partial t}\Phi_I, \tag{4.33}$$

whereby the $c_j^{(l)}(t)$ coefficients are obtained[80] for any l, via a procedure analogous to that employed to solve equation (4.20).

4.1 Time-Dependent Electron Charge Densities

In this section we will show explicitly the equations that define the first order induced charge polarization density using the previous derived equation (4.28) obtained with time dependent perturbation theory. If the electronic eigenstates have been determined for a molecule perturbed by an external static magnetic field $\boldsymbol{B}$, $\Psi_a^{(0)}$ and $\Psi_j^{(0)}$ contain imaginary contributions. Therefore, within the electric quadrupole approximation (EQA),[83] and to first order in the fields associated to a monochromatic plane wave, six charge densities are considered to account for perturbation effects,[79]

$$\begin{aligned}\rho^{(1)}(\boldsymbol{r},\omega) &= \rho^{\boldsymbol{E}}(\boldsymbol{r},\omega)+\rho^{\dot{\boldsymbol{B}}}(\boldsymbol{r},\omega)+\rho^{\boldsymbol{\nabla E}}(\boldsymbol{r},\omega)\\ &+ \rho^{\dot{\boldsymbol{E}}}(\boldsymbol{r},\omega)+\rho^{\boldsymbol{B}}(\boldsymbol{r},\omega)+\rho^{\boldsymbol{\nabla}\dot{\boldsymbol{E}}}(\boldsymbol{r},\omega)\end{aligned} \tag{4.34}$$

where here we have changed the argument of the function from t to ω because it is usual, if we want to study the topology of these scalar fields, to analyze them considering a fixed time, for example $t = 0$ in which $\cos(\omega t) = 1$. The expressions that define the different terms are

$$\rho^{\boldsymbol{E}}(\boldsymbol{r},\omega) = -\frac{2ne}{\hbar}E_\beta(\boldsymbol{0},\omega)\sum_{j\neq a}\frac{\omega_{ja}}{\omega_{ja}^2-\omega^2}\Re\left\{\langle a|\hat{\mu}_\beta|j\rangle\int\Psi_j^{(0)*}(\boldsymbol{r},\boldsymbol{X}_1)\Psi_a^{(0)}(\boldsymbol{r},\boldsymbol{X}_1)d\boldsymbol{X}_1\right\} \tag{4.35}$$

$$\rho^{\dot{\boldsymbol{B}}}(\boldsymbol{r},\omega) = -\frac{2ne}{\hbar}\dot{B}_\beta(\omega)\sum_{j\neq a}\frac{1}{\omega_{ja}^2-\omega^2}\Im\left\{\langle a|\hat{m}_\beta|j\rangle\int\Psi_j^{(0)*}(\boldsymbol{r},\boldsymbol{X}_1)\Psi_a^{(0)}(\boldsymbol{r},\boldsymbol{X}_1)d\boldsymbol{X}_1\right\} \tag{4.36}$$

$$\rho^{\boldsymbol{\nabla E}}(\boldsymbol{r},\omega) = -\frac{2ne}{\hbar}E_{\gamma\beta}(\omega)\sum_{j\neq a}\frac{\omega_{ja}}{\omega_{ja}^2-\omega^2}\Re\left\{\langle a|\hat{\mu}_{\beta\gamma}|j\rangle\int\Psi_j^{(0)*}(\boldsymbol{r},\boldsymbol{X}_1)\Psi_a^{(0)}(\boldsymbol{r},\boldsymbol{X}_1)d\boldsymbol{X}_1\right\} \tag{4.37}$$

$$\rho^{\dot{\boldsymbol{E}}}(\boldsymbol{r},\omega) = -\frac{2ne}{\hbar}\dot{E}_\beta(\boldsymbol{0},\omega)\sum_{j\neq a}\frac{1}{\omega_{ja}^2-\omega^2}\Im\left\{\langle a|\hat{\mu}_\beta|j\rangle\int\Psi_j^{(0)*}(\boldsymbol{r},\boldsymbol{X}_1)\Psi_a^{(0)}(\boldsymbol{r},\boldsymbol{X}_1)d\boldsymbol{X}_1\right\} \tag{4.38}$$

$$\rho^{\boldsymbol{B}}(\boldsymbol{r},\omega) = -\frac{2ne}{\hbar}B_\beta(\omega)\sum_{j\neq a}\frac{\omega_{ja}}{\omega_{ja}^2-\omega^2}\Re\left\{\langle a|\hat{m}_\beta|j\rangle\int\Psi_j^{(0)*}(\boldsymbol{r},\boldsymbol{X}_1)\Psi_a^{(0)}(\boldsymbol{r},\boldsymbol{X}_1)d\boldsymbol{X}_1\right\} \tag{4.39}$$

$$\rho^{\boldsymbol{\nabla}\dot{\boldsymbol{E}}}(\boldsymbol{r},\omega) = -\frac{2ne}{\hbar}\dot{E}_{\gamma\beta}(\omega)\sum_{j\neq a}\frac{1}{\omega_{ja}^2-\omega^2}\Im\left\{\langle a|\hat{\mu}_{\beta\gamma}|j\rangle\int\Psi_j^{(0)*}(\boldsymbol{r},\boldsymbol{X}_1)\Psi_a^{(0)}(\boldsymbol{r},\boldsymbol{X}_1)d\boldsymbol{X}_1\right\} \tag{4.40}$$

If $\Psi_a^{(0)}$ and $\Psi_j^{(0)}$ are real, the second line of equation (4.34) vanishes. The polarization charge density (4.34) is invariant with respect to passive and active translations of the origin[79] if the hypervirial momentum theorem[57] expressed in terms of off-diagonal hypervirial relationships introduced before in equations (3.67) and (3.68) is satisfied. Within the algebraic approximation,[85] this condition is met only for complete basis sets.

4.2 Time-Dependent Electron Current Densities

Using an approach similar to the one employed in the previous section, for the induced first-order charge polarization, it is possible to obtain equations defining the first-order induced current density vector using equation (4.29). As before, if the electronic eigenstates have been determined for a molecule perturbed by an external static magnetic field $\boldsymbol{B}$, $\Psi_a^{(0)}$ and $\Psi_j^{(0)}$ contain imaginary contributions. Therefore, within the electric quadrupole approximation (EQA),[83] and to first order in the fields associated to a monochromatic plane wave, six terms must be considered to account for perturbation effects,[79]

$$\begin{aligned} \boldsymbol{J}^{(1)}(\boldsymbol{r},\omega) &= \boldsymbol{J}^{\dot{\boldsymbol{E}}}(\boldsymbol{r},\omega) + \boldsymbol{J}^{\boldsymbol{B}}(\boldsymbol{r},\omega) + \boldsymbol{J}^{\boldsymbol{\nabla}\dot{\boldsymbol{E}}}(\boldsymbol{r},\omega) \\ &+ \boldsymbol{J}^{\boldsymbol{E}}(\boldsymbol{r},\omega) + \boldsymbol{J}^{\dot{\boldsymbol{B}}}(\boldsymbol{r},\omega) + \boldsymbol{J}^{\boldsymbol{\nabla}\boldsymbol{E}}(\boldsymbol{r},\omega) \end{aligned} \tag{4.41}$$

where

$$\boldsymbol{J}^{\boldsymbol{B}}(\boldsymbol{r},\omega) \equiv \boldsymbol{J}^{\boldsymbol{B}}_{\mathrm{CO}}(\boldsymbol{r},\omega) = \boldsymbol{J}^{\boldsymbol{B}}_{\mathrm{p}}(\boldsymbol{r},\omega) + \boldsymbol{J}^{\boldsymbol{B}}_{\mathrm{d}}(\boldsymbol{r},\omega) \tag{4.42}$$

is calculated relying on the Van Vleck common origin (CO) approach.[86] The total electronic current density (4.41) is invariant with respect to passive and active translations of the origin[79] in the case of exact and optimal variational wavefunctions.[57]. It is expedient to rewrite the expression defined in equation (4.41) in terms of second- and third-rank current density tensors (CDT),[40] as done for the static case in the previous chapter, according to

$$\begin{aligned} \mathcal{J}_\alpha^{\dot{E}_\beta}(\boldsymbol{r},\omega) &= \frac{\partial J_\alpha^{\dot{\boldsymbol{E}}}}{\partial \dot{E}_\beta} = -\frac{ne}{m_{\mathrm{e}}\hbar}\sum_{j\neq a}\left(\omega_{ja}^2-\omega^2\right)^{-1} \\ &\times\Im\left\{\langle a\,|\hat{\mu}_\beta|\,j\rangle\int \Psi_j^{(0)*}(\boldsymbol{r},\boldsymbol{X}_1)\,\hat{p}_\alpha\Psi_a^{(0)}(\boldsymbol{r},\boldsymbol{X}_1)\,d\boldsymbol{X}_1\right. \\ &\left.-\int \Psi_a^{(0)*}(\boldsymbol{r},\boldsymbol{X}_1)\,\hat{p}_\alpha\Psi_j^{(0)}(\boldsymbol{r},\boldsymbol{X}_1)\,d\boldsymbol{X}_1\,\langle j\,|\hat{\mu}_\beta|\,a\rangle\right\} \end{aligned} \tag{4.43}$$

$$\begin{aligned} \mathcal{J}_{\mathrm{p}_\alpha}^{B_\beta}(\boldsymbol{r},\omega) &= \frac{\partial J_\alpha^{\boldsymbol{B}}}{\partial B_\beta} = -\frac{ne}{m_{\mathrm{e}}\hbar}\sum_{j\neq a}\frac{\omega_{ja}}{\omega_{ja}^2-\omega^2} \\ &\times\Re\left\{\langle a\,|\hat{m}_\beta|\,j\rangle\int \Psi_j^{(0)*}(\boldsymbol{r},\boldsymbol{X}_1)\,\hat{p}_\alpha\Psi_a^{(0)}(\boldsymbol{r},\boldsymbol{X}_1)\,d\boldsymbol{X}_1\right. \\ &\left.+\int \Psi_a^{(0)*}(\boldsymbol{r},\boldsymbol{X}_1)\,\hat{p}_\alpha\Psi_j^{(0)}(\boldsymbol{r},\boldsymbol{X}_1)\,d\boldsymbol{X}_1\,\langle j\,|\hat{m}_\beta|\,a\rangle\right\} \end{aligned} \tag{4.44}$$

$$\mathcal{J}_{\mathrm{d}_\alpha}^{B_\beta} = \frac{\partial J_{\mathrm{d}_\alpha}^{\boldsymbol{B}}}{\partial B_\beta} = -\frac{e^2}{2m_{\mathrm{e}}}\epsilon_{\alpha\beta\gamma}r_\gamma\gamma^{(0)}(\boldsymbol{r}) \tag{4.45}$$

$$\begin{aligned} \mathcal{J}_\alpha^{\dot{E}_{\gamma\beta}}(\boldsymbol{r},\omega) &= \frac{\partial J_\alpha^{\boldsymbol{\nabla}\dot{\boldsymbol{E}}}}{\partial \dot{E}_{\gamma\beta}} = -\frac{ne}{m_{\mathrm{e}}\hbar}\sum_{j\neq a}\left(\omega_{ja}^2-\omega^2\right)^{-1} \\ &\times\Im\left\{\langle a\,|\hat{\mu}_{\beta\gamma}|\,j\rangle\int \Psi_j^{(0)*}(\boldsymbol{r},\boldsymbol{X}_1)\,\hat{p}_\alpha\Psi_a^{(0)}(\boldsymbol{r},\boldsymbol{X}_1)\,d\boldsymbol{X}_1\right. \\ &\left.-\int \Psi_a^{(0)*}(\boldsymbol{r},\boldsymbol{X}_1)\,\hat{p}_\alpha\Psi_j^{(0)}(\boldsymbol{r},\boldsymbol{X}_1)\,d\boldsymbol{X}_1\,\langle j\,|\hat{\mu}_{\beta\gamma}|\,a\rangle\right\} \end{aligned} \tag{4.46}$$

$$\mathcal{J}_{\alpha}^{E_{\beta}}(\boldsymbol{r},\omega) = \frac{\partial J_{\alpha}^{\boldsymbol{E}}}{\partial E_{\beta}} = -\frac{ne}{m_{\mathrm{e}}\hbar}\sum_{j\neq a}\frac{\omega_{ja}}{\omega_{ja}^{2}-\omega^{2}}\Re\Big\{\langle a\,|\hat{\mu}_{\beta}|\,j\rangle \times\int\Psi_{j}^{(0)*}(\boldsymbol{r},\boldsymbol{X}_{1})\,\hat{p}_{\alpha}\Psi_{a}^{(0)}(\boldsymbol{r},\boldsymbol{X}_{1})\,d\boldsymbol{X}_{1} +\int\Psi_{a}^{(0)*}(\boldsymbol{r},\boldsymbol{X}_{1})\,\hat{p}_{\alpha}\Psi_{j}^{(0)}(\boldsymbol{r},\boldsymbol{X}_{1})\,d\boldsymbol{X}_{1}\,\langle j\,|\hat{\mu}_{\beta}|\,a\rangle\Big\} \tag{4.47}$$

$$\mathcal{J}_{\alpha}^{\dot{B}_{\beta}}(\boldsymbol{r},\omega) = \frac{\partial J_{\alpha}^{\dot{\boldsymbol{B}}}}{\partial \dot{B}_{\beta}} = -\frac{ne}{m_{\mathrm{e}}\hbar}\sum_{j\neq a}\left(\omega_{ja}^{2}-\omega^{2}\right)^{-1}\Im\Big\{\langle a\,|\hat{m}_{\beta}|\,j\rangle \times\int\Psi_{j}^{(0)*}(\boldsymbol{r},\boldsymbol{X}_{1})\,\hat{p}_{\alpha}\Psi_{a}^{(0)}(\boldsymbol{r},\boldsymbol{X}_{1})\,d\boldsymbol{X}_{1} -\int\Psi_{a}^{(0)*}(\boldsymbol{r},\boldsymbol{X}_{1})\,\hat{p}_{\alpha}\Psi_{j}^{(0)}(\boldsymbol{r},\boldsymbol{X}_{1})\,d\boldsymbol{X}_{1}\,\langle j\,|\hat{m}_{\beta}|\,a\rangle\Big\} \tag{4.48}$$

$$\mathcal{J}_{\alpha}^{E_{\gamma\beta}}(\boldsymbol{r},\omega) = \frac{\partial J_{\alpha}^{\boldsymbol{\nabla E}}}{\partial E_{\gamma\beta}} = -\frac{ne}{m_{\mathrm{e}}\hbar}\sum_{j\neq a}\frac{\omega_{ja}}{\omega_{ja}^{2}-\omega^{2}}\Re\Big\{\langle a\,|\hat{\mu}_{\beta\gamma}|\,j\rangle \times\int\Psi_{j}^{(0)*}(\boldsymbol{r},\boldsymbol{X}_{1})\,\hat{p}_{\alpha}\Psi_{a}^{(0)}(\boldsymbol{r},\boldsymbol{X}_{1})\,d\boldsymbol{X}_{1} +\int\Psi_{a}^{(0)*}(\boldsymbol{r},\boldsymbol{X}_{1})\,\hat{p}_{\alpha}\Psi_{j}^{(0)}(\boldsymbol{r},\boldsymbol{X}_{1})\,d\boldsymbol{X}_{1}\,\langle j\,|\hat{\mu}_{\beta\gamma}|\,a\rangle\Big\} \tag{4.49}$$

In this case if $\Psi_{a}^{(0)}$ and $\Psi_{j}^{(0)}$ are real the second line of equation (4.41) vanishes. In the following, we will not consider any term in the second line of equation (4.41) as they vanish as a consequence of choosing real unperturbed eigenstates. As regards terms contained in the first line, of equation (4.41), their physical behavior will be illustrated. For this purpose the decomposition of these tensors into a pure static and a pure dynamic contribution will be given. Furthermore the links between the vectors, from which these tensors can be obtained by differentiation, and some molecular properties like polarizabilities and optical rotation power will be shown.

4.3 Charge and Current Conservation

Now that we have introduced the first order polarization charge and the total induced current density vector at the first order, in the quadrupole approximation, it is important to establish the laws that link the currents to the charge distributions term by term. These laws can be written in terms of continuity equations for the different kinds of perturbations considered in this approximation[87]

$$\nabla_\alpha J_\alpha^{\dot{\boldsymbol{E}}} + \frac{\partial}{\partial t}\rho^{\boldsymbol{E}} = 0 \tag{4.50}$$

$$\nabla_\alpha J_\alpha^{\boldsymbol{B}} + \frac{\partial}{\partial t}\rho^{\dot{\boldsymbol{B}}} = 0 \tag{4.51}$$

$$\nabla_\alpha J_\alpha^{\nabla\dot{\boldsymbol{E}}} + \frac{\partial}{\partial t}\rho^{\nabla\boldsymbol{E}} = 0 \tag{4.52}$$

$$\nabla_\alpha J_\alpha^{\boldsymbol{E}} + \frac{\partial}{\partial t}\rho^{\dot{\boldsymbol{E}}} = 0 \tag{4.53}$$

$$\nabla_\alpha J_\alpha^{\dot{\boldsymbol{B}}} + \frac{\partial}{\partial t}\rho^{\boldsymbol{B}} = 0 \tag{4.54}$$

$$\nabla_\alpha J_\alpha^{\nabla\boldsymbol{E}} + \frac{\partial}{\partial t}\rho^{\nabla\dot{\boldsymbol{E}}} = 0 \tag{4.55}$$

A tensorial notation of the previous equations is also useful

$$\nabla_\alpha \mathcal{J}_\alpha^{\dot{E}_\beta} + \varrho^{E_\beta} = 0 \tag{4.56}$$

$$\nabla_\alpha \mathcal{J}_\alpha^{B_\beta} - \omega^2 \varrho^{\dot{B}_\beta} = 0 \tag{4.57}$$

$$\nabla_\alpha \mathcal{J}_\alpha^{\nabla_\gamma \dot{E}_\beta} + \varrho^{\nabla_\gamma E_\beta} = 0 \tag{4.58}$$

$$\nabla_\alpha \mathcal{J}_\alpha^{E_\beta} - \omega^2 \varrho^{\dot{E}_\beta} = 0 \tag{4.59}$$

$$\nabla_\alpha \mathcal{J}_\alpha^{\dot{B}_\beta} + \varrho^{B_\beta} = 0 \tag{4.60}$$

$$\nabla_\alpha \mathcal{J}_\alpha^{\nabla_\gamma E_\beta} - \omega^2 \varrho^{\nabla_\gamma \dot{E}_\beta} = 0 \tag{4.61}$$

where in general we have introduced the notation

$$\varrho^{X_\beta} = \frac{\partial \rho^{\boldsymbol{X}}}{\partial X_\beta} \tag{4.62}$$

to identify the vector that can be used to define the perturbed polarization charge at first order. It is found that these continuity equations are satisfied by the exact eigenfunctions of a model Hamiltonian and by variationally optimal wavefunctions, for which hypervirial theorems are valid. They are expected to hold only approximately in calculations using the algebraic approximation, with increasing accuracy for extended high-quality basis sets.

4.4 Time-Dependent CTOCD-DZ

Within the algebraic approximation,[85] computed CO current densities, equation (4.42), introduced before are not separately invariant of origin. Starting from these definitions, it is possible to obtain a magnetically induced current that is alone invariant under active and passive translations of the origin, as for the time-independent case shown in chapter 3. These new relationships defining this magnetically induced current density can be obtained starting from equation

$$\begin{aligned}
\mathcal{J}_{\alpha}^{B_{\beta}}(\boldsymbol{r},\omega) &= \frac{ne^2}{2m_{\mathrm{e}}^2\hbar}\sum_{j\neq a}\frac{\omega_{ja}}{\omega_{ja}^2-\omega^2} \\
&\quad\times\Re\left\{\left\langle a\left|\hat{L}_{\beta}\right|j\right\rangle\int\Psi_j^{(0)*}(\boldsymbol{r},\boldsymbol{X}_1)\,\hat{p}_{\alpha}\Psi_a^{(0)}(\boldsymbol{r},\boldsymbol{X}_1)\,d\boldsymbol{X}_1\right. \\
&\quad\left.+\int\Psi_a^{(0)*}(\boldsymbol{r},\boldsymbol{X}_1)\,\hat{p}_{\alpha}\Psi_j^{(0)}(\boldsymbol{r},\boldsymbol{X}_1)\,d\boldsymbol{X}_1\left\langle j\left|\hat{L}_{\beta}\right|a\right\rangle\right\} \\
&\quad-\frac{e^2}{2m_{\mathrm{e}}}\epsilon_{\alpha\beta\gamma}r_{\gamma}\gamma^{(0)}(\boldsymbol{r})
\end{aligned} \tag{4.63}$$

and introducing a translation of the origin $\boldsymbol{r}' \rightarrow \boldsymbol{r}'' = \boldsymbol{r}' + \boldsymbol{d}$, assuming $\boldsymbol{r}'$ coincident with the origin of the reference system. In this way we have that

$$\begin{aligned}
\mathcal{J}_{\alpha}^{B_{\beta}}(\boldsymbol{r},\omega) &= \frac{ne^2}{2m_{\mathrm{e}}^2\hbar}\sum_{j\neq a}\frac{\omega_{ja}}{\omega_{ja}^2-\omega^2}\Re\left\{\left\langle a\left|\hat{L}_{\beta}\right|j\right\rangle\int\Psi_j^{(0)*}(\boldsymbol{r},\boldsymbol{X}_1)\,\hat{p}_{\alpha}\Psi_a^{(0)}(\boldsymbol{r},\boldsymbol{X}_1)\,d\boldsymbol{X}_1\right. \\
&\quad-\epsilon_{\beta\gamma\delta}d_{\gamma}\left\langle a\left|\hat{P}_{\delta}\right|j\right\rangle\int\Psi_j^{(0)*}(\boldsymbol{r},\boldsymbol{X}_1)\,\hat{p}_{\alpha}\Psi_a^{(0)}(\boldsymbol{r},\boldsymbol{X}_1)\,d\boldsymbol{X}_1 \\
&\quad+\int\Psi_a^{(0)*}(\boldsymbol{r},\boldsymbol{X}_1)\,\hat{p}_{\alpha}\Psi_j^{(0)}(\boldsymbol{r},\boldsymbol{X}_1)\,d\boldsymbol{X}_1\left\langle j\left|\hat{L}_{\beta}\right|a\right\rangle \\
&\quad\left.-\epsilon_{\beta\gamma\delta}d_{\gamma}\int\Psi_a^{(0)*}(\boldsymbol{r},\boldsymbol{X}_1)\,\hat{p}_{\alpha}\Psi_j^{(0)}(\boldsymbol{r},\boldsymbol{X}_1)\,d\boldsymbol{X}_1\left\langle j\left|\hat{P}_{\delta}\right|a\right\rangle\right\} \\
&\quad-\frac{e^2}{2m_{\mathrm{e}}}\epsilon_{\alpha\beta\gamma}r_{\gamma}\gamma^{(0)}(\boldsymbol{r})+\frac{e^2}{2m_{\mathrm{e}}}\epsilon_{\alpha\beta\gamma}d_{\gamma}\gamma^{(0)}(\boldsymbol{r})
\end{aligned} \tag{4.64}$$

As before, it is the aim of the CTOCD method to assume that $\boldsymbol{d}$ depends on the position, i.e., $\boldsymbol{d}(\boldsymbol{r})$. By choosing the ipsocentric approach, $\boldsymbol{d}(\boldsymbol{r}) = \boldsymbol{r}$, we are able to recover the two non-Larmor terms defined according to

$$\begin{aligned}
\mathcal{J}_{\mathrm{p}_{\alpha}}^{B_{\beta}}(\boldsymbol{r},\omega) &= \frac{ne^2}{2m_{\mathrm{e}}^2\hbar}\sum_{j\neq a}\frac{\omega_{ja}}{\omega_{ja}^2-\omega^2} \\
&\quad\times\Re\left\{\left\langle a\left|\hat{L}_{\beta}\right|j\right\rangle\int\Psi_j^{(0)*}(\boldsymbol{r},\boldsymbol{X}_1)\,\hat{p}_{\alpha}\Psi_a^{(0)}(\boldsymbol{r},\boldsymbol{X}_1)\,d\boldsymbol{X}_1\right. \\
&\quad\left.+\int\Psi_a^{(0)*}(\boldsymbol{r},\boldsymbol{X}_1)\,\hat{p}_{\alpha}\Psi_j^{(0)}(\boldsymbol{r},\boldsymbol{X}_1)\,d\boldsymbol{X}_1\left\langle j\left|\hat{L}_{\beta}\right|a\right\rangle\right\}
\end{aligned} \tag{4.65}$$

$$\begin{aligned}\mathcal{J}_{\mathrm{p}_\alpha}^{(\boldsymbol{d}\times\boldsymbol{B})_\beta}(\boldsymbol{r},\omega) &= -\frac{ne^2}{2m_{\mathrm{e}}^2\hbar}\epsilon_{\beta\gamma\delta}r_\gamma\sum_{j\neq a}\frac{\omega_{ja}}{\omega_{ja}^2-\omega^2}\\ &\times\Re\left\{\left\langle a\left|\hat{P}_\delta\right|j\right\rangle\int\Psi_j^{(0)*}(\boldsymbol{r},\boldsymbol{X}_1)\,\hat{p}_\alpha\Psi_a^{(0)}(\boldsymbol{r},\boldsymbol{X}_1)\,d\boldsymbol{X}\right.\\ &\left.+\int\Psi_a^{(0)*}(\boldsymbol{r},\boldsymbol{X}_1)\,\hat{p}_\alpha\Psi_j^{(0)}(\boldsymbol{r},\boldsymbol{X}_1)\,d\boldsymbol{X}_1\left\langle j\left|\hat{P}_\delta\right|a\right\rangle\right\} \qquad (4.66)\end{aligned}$$

Let's consider now the $\mathcal{J}_{\mathrm{p}_\alpha}^{B_\beta}$ term. If we multiply and divide by ω_{ja}, the fraction can be rewritten as

$$\frac{\omega_{ja}}{\omega_{ja}}\frac{\omega_{ja}}{\omega_{ja}^2-\omega^2}=\frac{1}{\omega_{ja}}\left[1+\frac{\omega^2}{\omega_{ja}^2-\omega^2}\right]=\frac{1}{\omega_{ja}}+\frac{\omega^2}{\omega_{ja}(\omega_{ja}^2-\omega^2)} \qquad (4.67)$$

Then, the CTOCD-DZ dynamic current density tensor is rewritten

$$\mathcal{J}_{\mathrm{p}_\alpha}^{B_\beta}(\boldsymbol{r},\omega)=\mathcal{J}_{\mathrm{ps}_\alpha}^{B_\beta}(\boldsymbol{r})+\mathcal{J}_{\mathrm{pd}_\alpha}^{B_\beta}(\boldsymbol{r},\omega) \qquad (4.68)$$

with

$$\begin{aligned}\mathcal{J}_{\mathrm{ps}_\alpha}^{B_\beta}(\boldsymbol{r}) &= \frac{ne^2}{2m_{\mathrm{e}}^2\hbar}\sum_{j\neq a}(\omega_{ja})^{-1}\\ &\times\Re\left\{\left\langle a\left|\hat{L}_\beta\right|j\right\rangle\int\Psi_j^{(0)*}(\boldsymbol{r},\boldsymbol{X}_1)\,\hat{p}_\alpha\Psi_a^{(0)}(\boldsymbol{r},\boldsymbol{X}_1)\,d\boldsymbol{X}_1\right.\\ &\left.+\int\Psi_a^{(0)*}(\boldsymbol{r},\boldsymbol{X}_1)\,\hat{p}_\alpha\Psi_j^{(0)}(\boldsymbol{r},\boldsymbol{X}_1)\,d\boldsymbol{X}_1\left\langle j\left|\hat{L}_\beta\right|a\right\rangle\right\} \qquad (4.69)\end{aligned}$$

$$\begin{aligned}\mathcal{J}_{\mathrm{pd}_\alpha}^{B_\beta}(\boldsymbol{r},\omega) &= \frac{ne^2}{2m_{\mathrm{e}}^2\hbar}\sum_{j\neq a}\frac{\omega^2}{\omega_{ja}(\omega_{ja}^2-\omega^2)}\\ &\times\Re\left\{\left\langle a\left|\hat{L}_\beta\right|j\right\rangle\int\Psi_j^{(0)*}(\boldsymbol{r},\boldsymbol{X}_1)\,\hat{p}_\alpha\Psi_a^{(0)}(\boldsymbol{r},\boldsymbol{X}_1)\,d\boldsymbol{X}_1\right.\\ &\left.+\int\Psi_a^{(0)*}(\boldsymbol{r},\boldsymbol{X}_1)\,\hat{p}_\alpha\Psi_j^{(0)}(\boldsymbol{r},\boldsymbol{X}_1)\,d\boldsymbol{X}_1\left\langle j\left|\hat{L}_\beta\right|a\right\rangle\right\} \qquad (4.70)\end{aligned}$$

where the first term gives the static limit while the second gives the dynamic behavior. Now, if we consider the $\mathcal{J}_{\mathrm{p}_\alpha}^{(\boldsymbol{d}\times\boldsymbol{B})_\beta}$ term of the CTOCD-DZ current density tensor a similar factorization

$$\mathcal{J}_{\mathrm{p}_\alpha}^{(\boldsymbol{d}\times\boldsymbol{B})_\beta}(\boldsymbol{r},\omega)=\mathcal{J}_{\mathrm{ps}_\alpha}^{(\boldsymbol{d}\times\boldsymbol{B})_\beta}(\boldsymbol{r})+\mathcal{J}_{\mathrm{pd}_\alpha}^{(\boldsymbol{d}\times\boldsymbol{B})_\beta}(\boldsymbol{r},\omega) \qquad (4.71)$$

can be done. The results are

$$\begin{aligned}\mathcal{J}_{\mathrm{ps}_\alpha}^{(\boldsymbol{d}\times\boldsymbol{B})_\beta}(\boldsymbol{r}) &= -\frac{ne^2}{2m_{\mathrm{e}}^2\hbar}\epsilon_{\beta\gamma\delta}r_\gamma\sum_{j\neq a}(\omega_{ja})^{-1}\\ &\times\Re\left\{\left\langle a\left|\hat{P}_\delta\right|j\right\rangle\int\Psi_j^{(0)*}(\boldsymbol{r},\boldsymbol{X}_1)\,\hat{p}_\alpha\ \Psi_a^{(0)}(\boldsymbol{r},\boldsymbol{X}_1)\,d\boldsymbol{X}_1\right.\\ &\left.+\int\Psi_a^{(0)*}(\boldsymbol{r},\boldsymbol{X}_1)\,\hat{p}_\alpha\ \Psi_j^{(0)}(\boldsymbol{r},\boldsymbol{X}_1)\,d\boldsymbol{X}_1\left\langle j\left|\hat{R}_\delta\right|a\right\rangle\right\} \qquad (4.72)\end{aligned}$$

$$
\begin{aligned}
\mathcal{J}^{(\boldsymbol{d}\times\boldsymbol{B})_\beta}_{\mathrm{pd}_\alpha}(\boldsymbol{r},\omega) &= -\frac{ne^2}{2m_{\mathrm{e}}^2\hbar}\epsilon_{\beta\gamma\delta}r_\gamma\sum_{j\neq a}\frac{\omega^2}{\omega_{ja}(\omega_{ja}^2-\omega^2)} \\
&\times\Re\left\{\left\langle a\left|\hat{P}_\delta\right|j\right\rangle\int\Psi_j^{(0)*}(\boldsymbol{r},\boldsymbol{X}_1)\,\hat{p}_\alpha\,\Psi_a^{(0)}(\boldsymbol{r},\boldsymbol{X}_1)\,d\boldsymbol{X}_1\right. \\
&\left.+\int\Psi_a^{(0)*}(\boldsymbol{r},\boldsymbol{X}_1)\,\hat{p}_\alpha\,\Psi_j^{(0)}(\boldsymbol{r},\boldsymbol{X}_1)\,d\boldsymbol{X}_1\left\langle j\left|\hat{P}_\delta\right|a\right\rangle\right\} \qquad (4.73)
\end{aligned}
$$

The equations derived here, decomposing the tensor $\mathcal{J}^{(\boldsymbol{d}\times\boldsymbol{B})_\beta}_{\mathrm{p}_\alpha}$ into a static and a dynamic contribution, can be rewritten using the off-diagonal hypervirial relationships (3.67) and (3.68) and the relation $\Re[\mathrm{i}(a+\mathrm{i}b)] = -\Im(a+\mathrm{i}b)$ as

$$
\begin{aligned}
\mathcal{J}^{(\boldsymbol{d}\times\boldsymbol{B})_\beta}_{\mathrm{ps}_\alpha}(\boldsymbol{r}) &= -\frac{ne^2}{2m_{\mathrm{e}}\hbar}\epsilon_{\beta\gamma\delta}r_\gamma\sum_{j\neq a} \\
&\times\Im\left\{\left\langle a\left|\hat{R}_\delta\right|j\right\rangle\int\Psi_j^{(0)*}(\boldsymbol{r},\boldsymbol{X}_1)\,\hat{p}_\alpha\,\Psi_a^{(0)}(\boldsymbol{r},\boldsymbol{X}_1)\,d\boldsymbol{X}_1\right. \\
&\left.-\int\Psi_a^{(0)*}(\boldsymbol{r},\boldsymbol{X}_1)\,\hat{p}_\alpha\,\Psi_j^{(0)}(\boldsymbol{r},\boldsymbol{X}_1)\,d\boldsymbol{X}_1\left\langle j\left|\hat{R}_\delta\right|a\right\rangle\right\} \qquad (4.74)
\end{aligned}
$$

$$
\begin{aligned}
\mathcal{J}^{(\boldsymbol{d}\times\boldsymbol{B})_\beta}_{\mathrm{pd}_\alpha}(\boldsymbol{r},\omega) &= -\frac{ne^2}{2m_{\mathrm{e}}\hbar}\epsilon_{\beta\gamma\delta}r_\gamma\sum_{j\neq a}\frac{\omega^2}{\omega_{ja}^2-\omega^2} \\
&\times\Im\left\{\left\langle a\left|\hat{R}_\delta\right|j\right\rangle\int\Psi_j^{(0)*}(\boldsymbol{r},\boldsymbol{X}_1)\,\hat{p}_\alpha\,\Psi_a^{(0)}(\boldsymbol{r},\boldsymbol{X}_1)\,d\boldsymbol{X}_1\right. \\
&\left.-\int\Psi_a^{(0)*}(\boldsymbol{r},\boldsymbol{X}_1)\,\hat{p}_\alpha\,\Psi_j^{(0)}(\boldsymbol{r},\boldsymbol{X}_1)\,d\boldsymbol{X}_1\left\langle j\left|\hat{R}_\delta\right|a\right\rangle\right\} \qquad (4.75)
\end{aligned}
$$

Summarizing, we note that it is possible to express the CTOCD-DZ current density tensor as

$$
\mathcal{I}_\alpha^{B_\beta}(\boldsymbol{r},\omega) = \mathcal{J}^{B_\beta}_{\mathrm{ps}_\alpha}(\boldsymbol{r}) + \mathcal{J}^{B_\beta}_{\mathrm{pd}_\alpha}(\boldsymbol{r},\omega) + \mathcal{J}^{(\boldsymbol{d}\times\boldsymbol{B})_\beta}_{\mathrm{ps}_\alpha}(\boldsymbol{r}) + \mathcal{J}^{(\boldsymbol{d}\times\boldsymbol{B})_\beta}_{\mathrm{pd}_\alpha}(\boldsymbol{r},\omega) \qquad (4.76)
$$

while the vector can be rewritten as

$$
\begin{aligned}
\boldsymbol{I}^{\boldsymbol{B}}(\boldsymbol{r},\omega) &= \boldsymbol{J}^{\boldsymbol{B}}_{\mathrm{ps}}(\boldsymbol{r},\omega) + \boldsymbol{J}^{\boldsymbol{B}}_{\mathrm{pd}}(\boldsymbol{r},\omega) + \boldsymbol{J}^{\boldsymbol{d}\times\boldsymbol{B}}_{\mathrm{ps}}(\boldsymbol{r},\omega) + \boldsymbol{J}^{\boldsymbol{d}\times\boldsymbol{B}}_{\mathrm{pd}}(\boldsymbol{r},\omega) \qquad (4.77) \\
&= \boldsymbol{J}^{\boldsymbol{B}}_{\mathrm{ps}}(\boldsymbol{r},\omega) + \boldsymbol{J}^{\boldsymbol{B}}_{\mathrm{pd}}(\boldsymbol{r},\omega) + \boldsymbol{J}^{\boldsymbol{d}\times\boldsymbol{B}}_{\mathrm{ps}}(\boldsymbol{r},\omega) + \boldsymbol{\Delta}(\boldsymbol{r},\omega) \qquad (4.78)
\end{aligned}
$$

where

$$
\boldsymbol{\Delta}(\boldsymbol{r},\omega) = \boldsymbol{J}^{\boldsymbol{d}\times\boldsymbol{B}}_{\mathrm{pd}}(\boldsymbol{r},\omega) \qquad (4.79)
$$

The technique applied here to decompose the time-dependent CTOCD-DZ current density tensor, in a pure static and a pure dynamic term, can be applied in general to all the dynamic current density tensors previously derived, as we will see in the following sections. We note also that

$$
\begin{aligned}
&\int J^{\boldsymbol{B}}_{\mathrm{ps}_\alpha}(\boldsymbol{r},0)\,d^3r = \frac{e^2}{2m_{\mathrm{e}}^2}\left\{\hat{P}_\alpha,\hat{L}_\beta\right\}_{-1}B_\beta \\
&\int J^{\boldsymbol{d}\times\boldsymbol{B}}_{\mathrm{ps}_\alpha}(\boldsymbol{r},0)\,d^3r = -\frac{e^2}{4m_{\mathrm{e}}^2}\left\{\hat{P}_\alpha,\hat{L}_\beta\right\}_{-1}B_\beta - \frac{e^2}{4m_{\mathrm{e}}}\epsilon_{\alpha\beta\gamma}\left\langle a\left|\hat{R}_\gamma\right|a\right\rangle B_\beta
\end{aligned} \qquad (4.80)
$$

with

$$\left\{\hat{P}_\alpha, \hat{L}_\beta\right\}_{-1} = \frac{1}{\hbar}\sum_{j\neq a}\frac{2}{\omega_{ja}}\Re\left\{\left\langle a\left|\hat{P}_\alpha\right|j\right\rangle\left\langle j\left|\hat{L}_\beta\right|a\right\rangle\right\} = m_{\mathrm{e}}\epsilon_{\alpha\beta\gamma}\left\langle a\left|\hat{R}_\gamma\right|a\right\rangle \tag{4.81}$$

as in the static case shown in chapter 3, while in the dynamic case the satisfied relationships are

$$\int J^{\boldsymbol{B}}_{\mathrm{p}_\alpha}(\boldsymbol{r},\omega)\,d^3r = -\kappa'^{(R,L)}_{\alpha\beta}\omega B_\beta(\omega) + \frac{e^2}{2m_{\mathrm{e}}^2}\left\{\hat{P}_\alpha, \hat{L}_\beta\right\}_{-1} B_\beta(\omega) \tag{4.82}$$

$$\int J^{\boldsymbol{d}\times\boldsymbol{B}}_{\mathrm{p}_\alpha}(\boldsymbol{r},\omega)\,d^3r = \frac{1}{2}\left\{\omega\left[\kappa'_{\alpha\beta} - \kappa'_{\gamma\gamma}\delta_{\alpha\beta} - \omega\epsilon_{\beta\gamma\delta}\alpha_{\delta,\gamma\alpha}\right] - \frac{e^2}{m_{\mathrm{e}}}\epsilon_{\alpha\beta\gamma}\left\langle a\left|\hat{R}_\gamma\right|a\right\rangle\right\} B_\beta(\omega) \tag{4.83}$$

where

$$\kappa'^{(R,L)}_{\alpha\beta} = -\frac{e^2}{2m_{\mathrm{e}}\hbar}\sum_{j\neq a}\frac{2\omega}{\omega_{ja}^2-\omega^2}\Im\left\{\left\langle a\left|\hat{R}_\alpha\right|j\right\rangle\left\langle j\left|\hat{L}_\beta\right|a\right\rangle\right\} \tag{4.84}$$

is the mixed electric-dipole magnetic-dipole polarizability in the (R,L) formalism, while $\alpha_{\alpha,\beta\gamma}$ is the mixed electric-dipole electric-quadrupole polarizability in the (R) or (P) gauges defined respectively as

$$\begin{aligned}
\alpha^{(R)}_{\alpha,\beta\gamma} &= -\frac{e}{\hbar}\sum_{j\neq a}\frac{2\omega_{ja}}{\omega_{ja}^2-\omega^2}\Re\left\{\left\langle a\left|\hat{R}_\alpha\right|j\right\rangle\left\langle j\left|\hat{\mu}_{\beta\gamma}\right|a\right\rangle\right\} \\
\alpha^{(P)}_{\alpha,\beta\gamma} &= \frac{e}{m_{\mathrm{e}}\hbar}\sum_{j\neq a}\frac{2}{\omega_{ja}^2-\omega^2}\Im\left\{\left\langle a\left|\hat{P}_\alpha\right|j\right\rangle\left\langle j\left|\hat{\mu}_{\beta\gamma}\right|a\right\rangle\right\}
\end{aligned} \tag{4.85}$$

From the previous equations it follows that

$$\int J^{\boldsymbol{B}}_{\mathrm{p}_\alpha}(\boldsymbol{r},\omega)\,d^3r + \int J^{\boldsymbol{d}\times\boldsymbol{B}}_{\mathrm{p}_\alpha}(\boldsymbol{r},\omega)\,d^3 = -\frac{1}{2}\left[\kappa'_{\gamma\gamma}\delta_{\alpha\beta} + \kappa'_{\alpha\beta} + \omega\epsilon_{\beta\gamma\delta}\alpha_{\delta,\gamma\alpha}\right]\omega B_\beta(\omega) \tag{4.86}$$

This relation can be used to obtain a definition of the isotropic optical rotation power density that is independent from the chosen origin[88][**4**]

$$\boxed{k'_{\alpha\alpha}(\boldsymbol{r},\omega) = -\frac{1}{2\omega}\mathcal{I}^{B_\alpha}_{\alpha}(\boldsymbol{r},\omega)} \tag{4.87}$$

4.5 Decomposition of the Current Density Induced by the Time Derivative of the Electric Field

Let us consider now the current density tensor components induced by the time derivative of the electric field

$$\begin{aligned}\mathcal{J}_{\alpha}^{\dot{E}_{\beta}}(\boldsymbol{r},\omega) &= \frac{ne^2}{m_{\mathrm{e}}\hbar}\sum_{j\neq a}\left(\omega_{ja}^2-\omega^2\right)^{-1}\\ &\times\Im\left\{\left\langle a\left|\hat{R}_{\beta}\right|j\right\rangle\int\Psi_j^{(0)*}(\boldsymbol{r},\boldsymbol{X}_1)\,\hat{p}_{\alpha}\Psi_a^{(0)}(\boldsymbol{r},\boldsymbol{X}_1)\,d\boldsymbol{X}_1\right.\\ &\left.-\int\Psi_a^{(0)*}(\boldsymbol{r},\boldsymbol{X}_1)\,\hat{p}_{\alpha}\Psi_j^{(0)}(\boldsymbol{r},\boldsymbol{X}_1)\,d\boldsymbol{X}_1\left\langle j\left|\hat{R}_{\beta}\right|a\right\rangle\right\}\end{aligned}\tag{4.88}$$

that constitutes a useful definition for an origin independent polarizability density. If we multiply and divide for ω_{ja}^2 being

$$\frac{\omega_{ja}^2}{\omega_{ja}^2}\frac{1}{\omega_{ja}^2-\omega^2}=\frac{1}{\omega_{ja}^2}\left[1+\frac{\omega^2}{\omega_{ja}^2-\omega^2}\right]=\frac{1}{\omega_{ja}^2}+\frac{\omega^2}{\omega_{ja}^2(\omega_{ja}^2-\omega^2)}\tag{4.89}$$

it is possible to write, as before, two terms

$$\mathcal{J}_{\alpha}^{\dot{E}_{\beta}}(\boldsymbol{r},\omega)=\mathcal{J}_{\mathrm{s}_{\alpha}}^{\dot{E}_{\beta}}(\boldsymbol{r})+\mathcal{J}_{\mathrm{d}_{\alpha}}^{\dot{E}_{\beta}}(\boldsymbol{r},\omega)\tag{4.90}$$

defined respectively as

$$\begin{aligned}\mathcal{J}_{\mathrm{s}_{\beta}}^{\dot{E}_{\gamma}}(\boldsymbol{r},\omega) &= \frac{ne^2}{m_{\mathrm{e}}\hbar}\sum_{j\neq a}\left(\omega_{ja}^2\right)^{-1}\\ &\times\Im\left\{\left\langle a\left|\hat{R}_{\gamma}\right|j\right\rangle\int\Psi_j^{(0)*}(\boldsymbol{r},\boldsymbol{X}_1)\,\hat{p}_{\beta}\Psi_a^{(0)}(\boldsymbol{r},\boldsymbol{X}_1)\,d\boldsymbol{X}_1\right.\\ &\left.-\int\Psi_a^{(0)*}(\boldsymbol{r},\boldsymbol{X}_1)\,\hat{p}_{\beta}\Psi_j^{(0)}(\boldsymbol{r},\boldsymbol{X}_1)\,d\boldsymbol{X}_1\left\langle j\left|\hat{R}_{\gamma}\right|a\right\rangle\right\}\end{aligned}\tag{4.91}$$

$$\begin{aligned}\mathcal{J}_{\mathrm{d}_{\beta}}^{\dot{E}_{\gamma}}(\boldsymbol{r},\omega) &= \frac{ne^2}{m_{\mathrm{e}}\hbar}\sum_{j\neq a}\frac{\omega^2}{\omega_{ja}^2(\omega_{ja}^2-\omega^2)}\\ &\times\Im\left\{\left\langle a\left|\hat{R}_{\gamma}\right|j\right\rangle\int\Psi_j^{(0)*}(\boldsymbol{r},\boldsymbol{X}_1)\,\hat{p}_{\beta}\Psi_a^{(0)}(\boldsymbol{r},\boldsymbol{X}_1)\,d\boldsymbol{X}_1\right.\\ &\left.-\int\Psi_a^{(0)*}(\boldsymbol{r},\boldsymbol{X}_1)\,\hat{p}_{\beta}\Psi_j^{(0)}(\boldsymbol{r},\boldsymbol{X}_1)\,d\boldsymbol{X}_1\left\langle j\left|\hat{R}_{\gamma}\right|a\right\rangle\right\}\end{aligned}\tag{4.92}$$

or using the off-diagonal hypervirial relationships (3.67) and (3.68) as

$$\begin{aligned}\mathcal{J}_{\mathrm{s}_{\beta}}^{\dot{E}_{\gamma}}(\boldsymbol{r},\omega) &= \frac{ne^2}{\hbar}\sum_{j\neq a}\left(\omega_{ja}\right)^{-3}\\ &\times\Im\left\{\mathrm{i}\left\langle a\left|\hat{P}_{\gamma}\right|j\right\rangle\int\Psi_j^{(0)*}(\boldsymbol{r},\boldsymbol{X}_1)\,\hat{p}_{\beta}\Psi_a^{(0)}(\boldsymbol{r},\boldsymbol{X}_1)\,d\boldsymbol{X}_1\right.\\ &\left.+\int\Psi_a^{(0)*}(\boldsymbol{r},\boldsymbol{X}_1)\,\hat{p}_{\beta}\Psi_j^{(0)}(\boldsymbol{r},\boldsymbol{X}_1)\,d\boldsymbol{X}_1\mathrm{i}\left\langle j\left|\hat{P}_{\gamma}\right|a\right\rangle\right\}\end{aligned}\tag{4.93}$$

$$\mathcal{J}^{\dot{E}_\gamma}_{\mathrm{d}_\beta}(\boldsymbol{r},\omega) = \frac{ne^2}{\hbar}\sum_{j\neq a}\frac{\omega^2}{\omega_{ja}^3(\omega_{ja}^2-\omega^2)} \times\Im\left\{\mathrm{i}\left\langle a\left|\hat{P}_\gamma\right|j\right\rangle\int\Psi_j^{(0)*}(\boldsymbol{r},\boldsymbol{X}_1)\,\hat{p}_\beta\Psi_a^{(0)}(\boldsymbol{r},\boldsymbol{X}_1)\,d\boldsymbol{X}_1 + \int\Psi_a^{(0)*}(\boldsymbol{r},\boldsymbol{X}_1)\,\hat{p}_\beta\Psi_j^{(0)}(\boldsymbol{r},\boldsymbol{X}_1)\,d\boldsymbol{X}_1\mathrm{i}\left\langle j\left|\hat{P}_\gamma\right|a\right\rangle\right\} \tag{4.94}$$

Now, using $\Im[\mathrm{i}(a+\mathrm{i}b)]=\Re(a+\mathrm{i}b)$ we obtain

$$\mathcal{J}^{\dot{E}_\gamma}_{\mathrm{s}_\beta}(\boldsymbol{r},\omega) = \frac{ne^2}{\hbar}\sum_{j\neq a}(\omega_{ja})^{-3} \times\Re\left\{\left\langle a\left|\hat{P}_\gamma\right|j\right\rangle\int\Psi_j^{(0)*}(\boldsymbol{r},\boldsymbol{X}_1)\,\hat{p}_\beta\Psi_a^{(0)}(\boldsymbol{r},\boldsymbol{X}_1)\,d\boldsymbol{X}_1 + \int\Psi_a^{(0)*}(\boldsymbol{r},\boldsymbol{X}_1)\,\hat{p}_\beta\Psi_j^{(0)}(\boldsymbol{r},\boldsymbol{X}_1)\,d\boldsymbol{X}_1\left\langle j\left|\hat{P}_\gamma\right|a\right\rangle\right\} \tag{4.95}$$

$$\mathcal{J}^{\dot{E}_\gamma}_{\mathrm{d}_\beta}(\boldsymbol{r},\omega) = \frac{ne^2}{\hbar}\sum_{j\neq a}\frac{\omega^2}{\omega_{ja}^3(\omega_{ja}^2-\omega^2)} \times\Re\left\{\left\langle a\left|\hat{P}_\gamma\right|j\right\rangle\int\Psi_j^{(0)*}(\boldsymbol{r},\boldsymbol{X}_1)\,\hat{p}_\beta\Psi_a^{(0)}(\boldsymbol{r},\boldsymbol{X}_1)\,d\boldsymbol{X}_1 + \int\Psi_a^{(0)*}(\boldsymbol{r},\boldsymbol{X}_1)\,\hat{p}_\beta\Psi_j^{(0)}(\boldsymbol{r},\boldsymbol{X}_1)\,d\boldsymbol{X}_1\left\langle j\left|\hat{P}_\gamma\right|a\right\rangle\right\} \tag{4.96}$$

The integration of the total vector gives

$$\int J^{\dot{\boldsymbol{E}}}_\alpha(\boldsymbol{r},\omega)\,d^3r = \alpha_{\beta\alpha}\dot{E}_\beta(\boldsymbol{0},\omega) \tag{4.97}$$

where $\alpha_{\beta\alpha}$ is the electric dipole polarizability defined in the mixed dipole-length dipole-velocity formalism

$$\alpha^{(RP)}_{\alpha\beta} = \frac{e^2}{m_\mathrm{e}\hbar}\sum_{j\neq a}\frac{2}{\omega_{ja}^2-\omega^2}\Im\left\{\left\langle a\left|\hat{R}_\alpha\right|j\right\rangle\left\langle j\left|\hat{P}_\beta\right|a\right\rangle\right\} \tag{4.98}$$

or using equations (4.95) and (4.96) in the dipole-velocity dipole-velocity formalism

$$\alpha^{(PP)}_{\alpha\beta} = \frac{e^2}{m_\mathrm{e}^2\hbar}\sum_{j\neq a}\frac{2}{\omega_{ja}(\omega_{ja}^2-\omega^2)}\Re\left\{\left\langle a\left|\hat{P}_\alpha\right|j\right\rangle\left\langle j\left|\hat{P}_\beta\right|a\right\rangle\right\} \tag{4.99}$$

4.6 Decomposition of the Current Density Induced by the Time Derivative of Electric Field Gradient

Let us consider the current density tensor components induced by the time derivative of the electric field gradient

$$\begin{aligned}\mathcal{J}_{\beta}^{\dot{E}_{\gamma\alpha}}(\boldsymbol{r},\omega) &= -\frac{ne}{m_{\mathrm{e}}\hbar}\sum_{j\neq a}\left(\omega_{ja}^{2}-\omega^{2}\right)^{-1} \\ &\times\Im\left\{\langle a\left|\hat{\mu}_{\alpha\gamma}\right|j\rangle\int\Psi_{j}^{(0)*}\left(\boldsymbol{r},\boldsymbol{X}_{1}\right)\hat{p}_{\beta}\Psi_{a}^{(0)}\left(\boldsymbol{r},\boldsymbol{X}_{1}\right)d\boldsymbol{X}_{1}\right. \\ &\left.-\int\Psi_{a}^{(0)*}\left(\boldsymbol{r},\boldsymbol{X}_{1}\right)\hat{p}_{\beta}\Psi_{j}^{(0)}\left(\boldsymbol{r},\boldsymbol{X}_{1}\right)d\boldsymbol{X}_{1}\langle j\left|\hat{\mu}_{\alpha\gamma}\right|a\rangle\right\} \end{aligned} \tag{4.100}$$

if we multiply and divide for ω_{ja}^{2} being

$$\frac{\omega_{ja}^{2}}{\omega_{ja}^{2}}\frac{1}{\omega_{ja}^{2}-\omega^{2}}=\frac{1}{\omega_{ja}^{2}}\left[1+\frac{\omega^{2}}{\omega_{ja}^{2}-\omega^{2}}\right]=\frac{1}{\omega_{ja}^{2}}+\frac{\omega^{2}}{\omega_{ja}^{2}(\omega_{ja}^{2}-\omega^{2})} \tag{4.101}$$

one obtains two terms

$$\mathcal{J}_{\beta}^{\dot{E}_{\gamma\alpha}}(\boldsymbol{r},\omega)=\mathcal{J}_{\mathrm{s}_{\beta}}^{\dot{E}_{\gamma\alpha}}(\boldsymbol{r})+\mathcal{J}_{\mathrm{d}_{\beta}}^{\dot{E}_{\gamma\alpha}}(\boldsymbol{r},\omega) \tag{4.102}$$

defined respectively as

$$\begin{aligned}\mathcal{J}_{\mathrm{s}_{\beta}}^{\dot{E}_{\gamma\alpha}}(\boldsymbol{r}) &= -\frac{ne}{m_{\mathrm{e}}\hbar}\sum_{j\neq a}\left(\omega_{ja}\right)^{-2} \\ &\times\Im\left\{\langle a\left|\hat{\mu}_{\alpha\gamma}\right|j\rangle\int\Psi_{j}^{(0)*}\left(\boldsymbol{r},\boldsymbol{X}_{1}\right)\hat{p}_{\beta}\Psi_{a}^{(0)}\left(\boldsymbol{r},\boldsymbol{X}_{1}\right)d\boldsymbol{X}_{1}\right. \\ &\left.-\int\Psi_{a}^{(0)*}\left(\boldsymbol{r},\boldsymbol{X}_{1}\right)\hat{p}_{\beta}\Psi_{j}^{(0)}\left(\boldsymbol{r},\boldsymbol{X}_{1}\right)d\boldsymbol{X}_{1}\langle j\left|\hat{\mu}_{\alpha\gamma}\right|a\rangle\right\} \end{aligned} \tag{4.103}$$

$$\begin{aligned}\mathcal{J}_{\mathrm{d}_{\beta}}^{\dot{E}_{\gamma\alpha}}(\boldsymbol{r},\omega) &= -\frac{ne}{m_{\mathrm{e}}\hbar}\sum_{j\neq a}\frac{\omega^{2}}{\omega_{ja}^{2}(\omega_{ja}^{2}-\omega^{2})} \\ &\times\Im\left\{\langle a\left|\hat{\mu}_{\alpha\gamma}\right|j\rangle\int\Psi_{j}^{(0)*}\left(\boldsymbol{r},\boldsymbol{X}_{1}\right)\hat{p}_{\beta}\Psi_{a}^{(0)}\left(\boldsymbol{r},\boldsymbol{X}_{1}\right)d\boldsymbol{X}_{1}\right. \\ &\left.-\int\Psi_{a}^{(0)*}\left(\boldsymbol{r},\boldsymbol{X}_{1}\right)\hat{p}_{\beta}\Psi_{j}^{(0)}\left(\boldsymbol{r},\boldsymbol{X}_{1}\right)d\boldsymbol{X}_{1}\langle j\left|\hat{\mu}_{\alpha\gamma}\right|a\rangle\right\} \end{aligned} \tag{4.104}$$

The integral of this current vector gives us the mixed electric-dipole electric-quadrupole polarizability

$$\int J_{\alpha}^{\boldsymbol{\nabla}\dot{\boldsymbol{E}}}d^{3}r=\alpha_{\alpha,\beta\gamma}^{(P)}\dot{E}_{\gamma\beta}(\omega) \tag{4.105}$$

where

$$\alpha_{\alpha,\beta\gamma}^{(P)}=\frac{e}{m_{\mathrm{e}}\hbar}\sum_{j\neq a}\frac{2}{\omega_{ja}^{2}-\omega^{2}}\Im\left\{\left\langle a\left|\hat{P}_{\alpha}\right|j\right\rangle\langle j\left|\hat{\mu}_{\beta\gamma}\right|a\rangle\right\} \tag{4.106}$$

CHAPTER 5

Implementations and Applications

The aim of this chapter is to show some applications of the previous reported equations and how they have been used to solve chemical problems. All the theory, described in the previous chapters, has been implemented within the freely available SYSMOIC package.[14][**3**] The SYSMOIC program is available online for three different platforms. Instructions for downloading and using the package can be found at: `http://sysmoic.chem.unisa.it/MANUAL/`.

5.1 Time-Independent Electron Current Densities

SYSMOIC is a program package for the calculation of origin-independent electron current density and derived magnetic properties in molecular systems. In particular, it can be used to compute the current density tensors for general unrestricted wavefunctions at the HF[43, 44] or DFT[89, 90] level of theory, using either the orbital or the density matrix approaches. Applying time-independent perturbation theory, as seen before in chapter 3, and introducing the vectors

$$\Psi_a^{L_\beta}(\boldsymbol{r},\boldsymbol{X}_1) = \frac{1}{\hbar}\sum_{j\neq a}\frac{1}{\omega_{ja}}\Psi_j^{(0)}(\boldsymbol{r},\boldsymbol{X}_1)\left\langle j\left|\hat{L}_\beta\right|a\right\rangle \tag{5.1}$$

$$\Psi_a^{P_\delta}(\boldsymbol{r},\boldsymbol{X}_1) = \frac{1}{\hbar}\sum_{j\neq a}\frac{1}{\omega_{ja}}\Psi_j^{(0)}(\boldsymbol{r},\boldsymbol{X}_1)\left\langle j\left|\hat{P}_\delta\right|a\right\rangle \tag{5.2}$$

we rewrite $\mathcal{J}_{\mathrm{p}\alpha}^{B_\beta}$ and $\mathcal{J}_{\mathrm{p}\alpha}^{(\boldsymbol{d}\times\boldsymbol{B})_\beta}$, see equations (3.46) and (3.65), as follows

$$\begin{aligned}\mathcal{J}_{\mathrm{p}\alpha}^{B_\beta}(\boldsymbol{r}) &= \frac{ne^2}{2m_{\mathrm{e}}^2}\Re\Big\{\int\Psi_a^{L_\beta *}(\boldsymbol{r},\boldsymbol{X}_1)\hat{p}_\alpha\Psi_a^{(0)}(\boldsymbol{r},\boldsymbol{X}_1)\,d\boldsymbol{X}_1 \\ &+ \int\Psi_a^{(0)*}(\boldsymbol{r},\boldsymbol{X}_1)\hat{p}_\alpha\Psi_a^{L_\beta}(\boldsymbol{r},\boldsymbol{X}_1)\,d\boldsymbol{X}_1\Big\}\end{aligned} \tag{5.3}$$

$$\mathcal{J}_{\mathrm{p}_\alpha}^{(\boldsymbol{d}\times\boldsymbol{B})_\beta}(\boldsymbol{r}) = -\frac{ne^2}{2m_{\mathrm{e}}^2}\epsilon_{\beta\gamma\delta}d_\gamma(\boldsymbol{r})\Re\Big\{\int \Psi_a^{P_\delta *}(\boldsymbol{r},\boldsymbol{X}_1)\hat{p}_\alpha\Psi_a^{(0)}(\boldsymbol{r},\boldsymbol{X}_1)\,d\boldsymbol{X}_1 + \int \Psi_a^{(0)*}(\boldsymbol{r},\boldsymbol{X}_1)\,\hat{p}_\alpha\Psi_a^{P_\delta}(\boldsymbol{r},\boldsymbol{X}_1)\,d\boldsymbol{X}_1\Big\} \tag{5.4}$$

Allowing for definitions of total electronic angular and linear momentum operators, defined in section 2.2, the vector functions (5.1) and (5.2) become

$$\Psi_a^{L_\beta}(\boldsymbol{r},\boldsymbol{X}_1) = -\mathrm{i}\hbar\Psi_a^{(\boldsymbol{r}\times\boldsymbol{\nabla})_\beta}(\boldsymbol{r},\boldsymbol{X}_1) \tag{5.5}$$

$$\Psi_a^{P_\delta}(\boldsymbol{r},\boldsymbol{X}_1) = -\mathrm{i}\hbar\Psi_a^{\nabla_\delta}(\boldsymbol{r},\boldsymbol{X}_1) \tag{5.6}$$

where

$$\Psi_a^{(\boldsymbol{r}\times\boldsymbol{\nabla})_\beta}(\boldsymbol{r},\boldsymbol{X}_1) = \sum_{j\neq a}\frac{1}{\omega_{ja}}\left\langle j\left|\sum_k\Big[(\boldsymbol{r}\times\boldsymbol{\nabla})_\beta\Big]_k\right|a\right\rangle\Psi_j^{(0)}(\boldsymbol{r},\boldsymbol{X}_1) \tag{5.7}$$

$$\Psi_a^{\nabla_\delta}(\boldsymbol{r},\boldsymbol{X}_1) = \sum_{j\neq a}\frac{1}{\omega_{ja}}\left\langle j\left|\sum_k(\nabla_\delta)_k\right|a\right\rangle\Psi_j^{(0)}(\boldsymbol{r},\boldsymbol{X}_1) \tag{5.8}$$

Assuming real eigenstates of the unperturbed Hamiltonian (we always use this assumption here and in the following), we obtain

$$\mathcal{J}_{\mathrm{p}_\alpha}^{B_\beta}(\boldsymbol{r}) = \frac{ne^2\hbar}{2m_{\mathrm{e}}^2}\Big\{\int\Psi_a^{(\boldsymbol{r}\times\boldsymbol{\nabla})_\beta}(\boldsymbol{r},\boldsymbol{X}_1)\nabla_\alpha\Psi_a^{(0)}(\boldsymbol{r},\boldsymbol{X}_1)\,d\boldsymbol{X}_1 - \int\Psi_a^{(0)}(\boldsymbol{r},\boldsymbol{X}_1)\nabla_\alpha\Psi_a^{(\boldsymbol{r}\times\boldsymbol{\nabla})_\beta}(\boldsymbol{r},\boldsymbol{X}_1)\,d\boldsymbol{X}_1\Big\} \tag{5.9}$$

$$\mathcal{J}_{\mathrm{p}_\alpha}^{(\boldsymbol{d}\times\boldsymbol{B})_\beta}(\boldsymbol{r}) = -\frac{ne^2\hbar}{2m_{\mathrm{e}}^2}\epsilon_{\beta\gamma\delta}d_\gamma(\boldsymbol{r})\Big\{\int\Psi_a^{\nabla_\delta}(\boldsymbol{r},\boldsymbol{X}_1)\nabla_\alpha\Psi_a^{(0)}(\boldsymbol{r},\boldsymbol{X}_1)\,d\boldsymbol{X}_1 - \int\Psi_a^{(0)}(\boldsymbol{r},\boldsymbol{X}_1)\,\nabla_\alpha\Psi_a^{\nabla_\delta}(\boldsymbol{r},\boldsymbol{X}_1)\,d\boldsymbol{X}_1\Big\} \tag{5.10}$$

For an unrestricted system, represented by a one-determinant wavefunction

$$\Psi = \frac{1}{\sqrt{n!}}\det\Big[\psi_1^\alpha,\psi_2^\beta,\cdots\Big] \tag{5.11}$$

constructed by $n = n_\alpha + n_\beta$ occupied molecular orbitals, equations (5.9) and (5.10) become, in atomic units,

$$\mathcal{J}_{\mathrm{p}_\alpha}^{B_\beta}(\boldsymbol{r}) = \frac{1}{2}\sum_j^n\Big[\psi_j^{(\boldsymbol{r}\times\boldsymbol{\nabla})_\beta}(\boldsymbol{r})\nabla_\alpha\psi_j^{(0)}(\boldsymbol{r}) - \psi_j^{(0)}(\boldsymbol{r})\nabla_\alpha\psi_j^{(\boldsymbol{r}\times\boldsymbol{\nabla})_\beta}(\boldsymbol{r})\Big] \tag{5.12}$$

$$\mathcal{J}_{\mathrm{p}_\alpha}^{(\boldsymbol{d}\times\boldsymbol{B})_\beta}(\boldsymbol{r}) = -\frac{1}{2}\epsilon_{\beta\gamma\delta}d_\gamma(\boldsymbol{r})\sum_j^n\Big[\psi_j^{\nabla_\delta}(\boldsymbol{r})\nabla_\alpha\psi_j^{(0)}(\boldsymbol{r}) - \psi_j^{(0)}(\boldsymbol{r})\,\nabla_\alpha\psi_j^{\nabla_\delta}(\boldsymbol{r})\Big] \tag{5.13}$$

The expressions for both diamagnetic contributions require only the electron charge density

$$\mathcal{J}_{\mathrm{d}_\alpha}^{B_\beta}(\boldsymbol{r}) = \frac{1}{2}\epsilon_{\alpha\beta\gamma}r_\gamma\rho^{(0)}(\boldsymbol{r}) \tag{5.14}$$

$$\mathcal{J}_{\mathrm{d}_\alpha}^{(\boldsymbol{d}\times\boldsymbol{B})_\beta}(\boldsymbol{r}) = -\frac{1}{2}\epsilon_{\alpha\beta\gamma}d_\gamma(\boldsymbol{r})\rho^{(0)}(\boldsymbol{r}) \tag{5.15}$$

The spatial part of spin-orbitals is expanded as linear combinations of basis functions χ_q, according to

$$\psi_j^{(0)}(\boldsymbol{r}) = \sum_q C_{qj}^{(0)} \chi_q(\boldsymbol{r}) \tag{5.16}$$

$$\psi_j^{(\boldsymbol{r}\times\boldsymbol{\nabla})_\beta}(\boldsymbol{r}) = \sum_q C_{qj}^{(\boldsymbol{r}\times\boldsymbol{\nabla})_\beta} \chi_q(\boldsymbol{r}) \tag{5.17}$$

$$\psi_j^{\nabla_\delta}(\boldsymbol{r}) = \sum_q C_{qj}^{\nabla_\delta} \chi_q(\boldsymbol{r}) \tag{5.18}$$

where $C_{qj}^{(0)}$ indicates canonical unperturbed coefficients, $C_{qj}^{(\boldsymbol{r}\times\boldsymbol{\nabla})_\beta}$ and $C_{qj}^{\nabla_\delta}$ are the perturbed coefficients, placing in the first n_α columns molecular orbitals of α spin and in the next n_β columns molecular orbitals of β spin. Substituting the expansions of perturbed spin orbitals in the previous equations, it can be seen that geometrical first derivatives of basis set functions are required for the current density tensor calculation. It is easily recognized that the electronic unperturbed charge density can be computed as

$$\rho(\boldsymbol{r}) = \sum_p \sum_q R_{pq}\, \chi_p(\boldsymbol{r}) \chi_q(\boldsymbol{r}) \tag{5.19}$$

where

$$R_{pq} = R_{pq}^\alpha + R_{pq}^\beta \tag{5.20}$$

$$R_{pq}^\alpha = \sum_{j=1}^{n_\alpha} C_{pj}^{(0)} (C_{qj}^{(0)})^* \tag{5.21}$$

$$R_{pq}^\beta = \sum_{j=n_\alpha+1}^{n_\beta} C_{pj}^{(0)} (C_{qj}^{(0)})^* \tag{5.22}$$

are respectively the total, the spin alpha and spin beta unperturbed density matrices. From (5.19) it is also possible to note the link between the orbital and the density matrix approach. For completeness, we present here also the equations for $\mathcal{J}_{\mathrm{p}_\alpha}^{B_\beta}$ and $\mathcal{J}_{\mathrm{p}_\alpha}^{(\boldsymbol{d}\times\boldsymbol{B})_\beta}$ written using the density matrix approach

$$\mathcal{J}_{\mathrm{p}_\alpha}^{B_\beta}(\boldsymbol{r}) = \frac{1}{2} \sum_p \sum_q R_{pq}^{\left([\boldsymbol{r}\times\boldsymbol{\nabla}]_\beta\right)_{+1}} \chi_q \nabla_\alpha \chi_p \tag{5.23}$$

$$\mathcal{J}_{\mathrm{p}_\alpha}^{(\boldsymbol{d}\times\boldsymbol{B})_\beta}(\boldsymbol{r}) = -\frac{1}{2} \epsilon_{\beta\gamma\delta} d_\gamma(\boldsymbol{r}) \sum_p \sum_q R_{pq}^{(\nabla_\delta)_{+1}} \chi_q \nabla_\alpha \chi_p \tag{5.24}$$

in which

$$R_{pq}^{\left([\boldsymbol{r}\times\boldsymbol{\nabla}]_\beta\right)_{+1}} = \sum_i^{\mathrm{n}} \left[C_{pi}^{(0)} C_{qi}^{\left([\boldsymbol{r}\times\boldsymbol{\nabla}]_\beta\right)_{+1}} - C_{pi}^{\left([\boldsymbol{r}\times\boldsymbol{\nabla}]_\beta\right)_{+1}} C_{qi}^{(0)} \right]$$

$$R_{pq}^{(\nabla_\delta)_{+1}} = \sum_i^{\mathrm{n}} \left[C_{pi}^{(0)} C_{qi}^{(\nabla_\delta)_{+1}} - C_{pi}^{(\nabla_\delta)_{+1}} C_{qi}^{(0)} \right] \tag{5.25}$$

are the perturbed anti-symmetric density matrices. Obviously, orbital decomposition of current densities, as well as related molecular properties, can be obtained only using the orbital "picture". However, the orbital "picture" is not suitable to deal with correlated

wavefunctions. In this latter case the density matrix "picture" can be used independently from the electronic structure method adopted for the calculation, getting, for example, the required density matrices in the atomic basis from another program.

The expressions defined in this section for implementation purposes are valid for both HF and DFT levels of theory and all coefficients are calculated using the Coupled Perturbed Hartree-Fock or Kohn-Sham procedures. For closed shell HF calculations these coefficients can be obtained directly with the SYSMOIC. In all other cases, it is possible to use the interfaces available within the SYSMOIC software to obtain the MO coefficients from a Gaussian 16[56] calculation, by means of the keywords NMR=CSGT output=(CSGT,wfx) through the wavefunction file. Geometrical first derivatives of the current density tensor, electronic charge density, and so on, are required by a number of package functionalities, as, for example, topological studies of induced fields but also gradient and vorticity of the current density. These geometrical derivatives can be easily derived, as described in Ref. [14][**3**]. Regarding the basis set expansion in SYSMOIC, unnormalized Cartesian Gaussian functions centered at $\boldsymbol{R}$ are used, defined as

$$\chi(\boldsymbol{r};\zeta,\boldsymbol{n},\boldsymbol{R}) = (x-R_x)^{n_x}\,(y-R_y)^{n_y}\,(z-R_z)^{n_z}\exp\left[-\zeta(\boldsymbol{r}-\boldsymbol{R})^2\right] \tag{5.26}$$

where ζ is the orbital exponent and $\boldsymbol{n} = (n_x, n_y, n_z)$ is a vector of non-negative integers. The sum $n_x+n_y+n_z$ is closely related to the total angular momentum quantum number. Analytical and numerical first, second and third derivatives of the basis set functions are available.

5.1.1 NMR Characterization of MB[6]CPP

One of the most exciting aspects of the research work occurs when one is able to contribute to the elucidation of a problem. This is the case, for example, of the methylene-bridged 6-cycloparaphenylene MB[6]CPP whose structure is illustrated in Figure 5.1.[91, 92][**2**] Rather interestingly, this nanobelt is predicted to sustain a global paratropic current

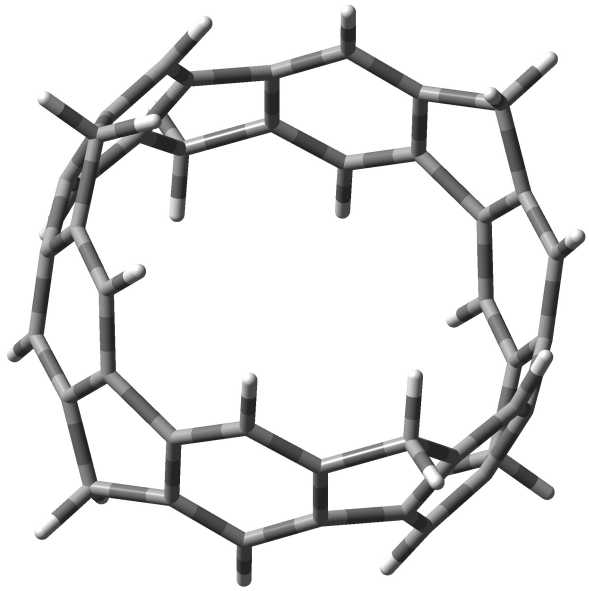

Figure 5.1: Structure of methylene-bridged 6-cycloparaphenylene MB[6]CPP.

around the belt in response to a magnetic perturbation parallel to the main symmetry z-axis. This is a consequence of the HOMO and LUMO symmetries whose direct product matches exactly the symmetry of the rotation R_z.[45, 46] *This behavior is typical of antiaromatic species, and a significant paratropic contribution to the current density induced by a parallel magnetic field is expected to occur. Thanks to Itami's newly reported and diversified experimental data,*[91] *the possibility to validate such a prediction can now be accomplished.*[92][**2**] *In particular, we want show the major impact of the paratropic current on the* ^{1}H-NMR *chemical shifts of this nanobelt.*

A powerful tool to detect and quantify delocalized currents, either diamagnetic (aromatic) or paramagnetic (antiaromatic), is provided by the so-called current strength, or current susceptibility, which provides the net current strength crossing a plane perpendicular to a selected bond in a molecule.[12] Our method to calculate current strengths is as follows.[13] Let P be a plane bisecting at right angles a given bond between atoms K and L and let $\boldsymbol{p}$ be a normal unitary vector pointing from K to L. The cross section of the current density over P is given by

$$J_{\perp}^{\boldsymbol{B}} = \boldsymbol{J}^{\boldsymbol{B}}(\boldsymbol{r}) \cdot \boldsymbol{p} \qquad \boldsymbol{r} \in P \tag{5.27}$$

The cross section $J_{\perp}^{\boldsymbol{B}}$ is a two-dimensional scalar field, having extremum points distributed around the center of the K-L bond. For each of these extrema a domain of integration of $J_{\perp}^{\boldsymbol{B}}$ can be defined as the area inside a contour line containing only that

extremum point and no other point of maximum or minimum. The contour line value is set as close to zero as possible in agreement with the above condition. Then, if N is the number of domains, the net current strength for the selected bond is given by

$$\sum_{I=1}^{N} \int_{I} \boldsymbol{J}^{\boldsymbol{B}}(\boldsymbol{r}) \cdot d\boldsymbol{p} \tag{5.28}$$

Other methods to calculate current strengths have been proposed in the literature.[93] By definition, only delocalized currents can give a contribution. Current strengths calculated at the B97-2/6-311+G(2d,p)//B97-2/6-31G(d) level, induced in the molecule by a magnetic field parallel to the main symmetry axis, are shown in Figure 5.2. Origin

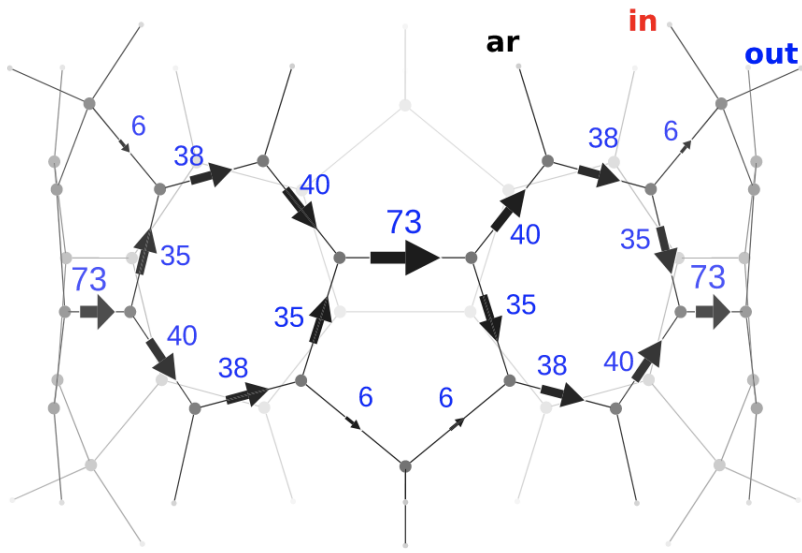

Figure 5.2: Net C−C bond current strengths for a magnetic field parallel to the main symmetry axis and pointing from bottom to top. Values aside each arrow represent the percentage relationship with respect to the benzene current strength. Circulation from left to right are globally paratropic/antiaromatic.

independence of the current density has been ensured by using the continuous set of gauge transformations method with atomic size adjustments determined by the bond critical points of the electron density distribution (CSGT-BCP).[54][**1**] As can be observed, in MB[6]CPP the current flow is paratropic and bifurcates and gathers around the six-membered rings of the embedded cycloparaphenylene nano-hoop.

Predicted and experimental ^{1}H-NMR chemical shifts are reported in Table 5.1. These

Table 5.1: Calculated and experimental ^{1}H-NMR chemical shifts of MB[6]CPP.

	H_{ar}	H_{in}	H_{out}
B972	8.11	4.08	4.22
expt.	7.86	4.09	4.29

are found to be in fairly good agreement. Putting aside for now the aromatic protons we

have found particularly interesting the positions of the signals for the methylene protons. According to the *anisotropy effect* due to the paratropic belt current, the methylene protons overlooking the current should experience a deshielding effect higher than that felt by the protons facing the outside of the belt see Figure 5.3 for a useful scheme of this description. Contrary to expectations based on this simple picture, however, both the

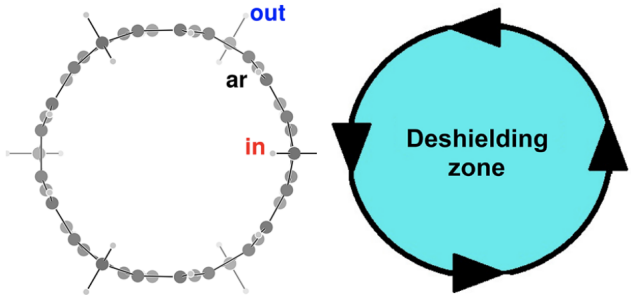

Figure 5.3: Left: top view. Right: schematic representation of the paratropic current flowing in a tiny wire having the nanobelt radius.

experimental data and the calculated chemical shifts show H_{in} more shielded than H_{out} by 0.20 ppm. Of course, other factors superimposed on the paratropic belt current must be taken into account, as, for example, the diatropic currents induced on the distorted atomic scaffold by a perpendicular magnetic field. These currents are predicted to be mainly local to the benzene rings, with sizable portions flowing on the methylene groups as a consequence of the hyperconjugation between the aliphatic C−H bonds and the aromatic π-system. To deconvolute this rather complex situation, we have explored the consequences of cutting the belt to switch off the paratropic current. In addition, to study the influence of the curvature, we have considered planar fluorene **3**, folded fluorene **4**, and a half of the nanobelt **5**, as shown in Figure 5.4. The geometries of **4** and **5** are taken

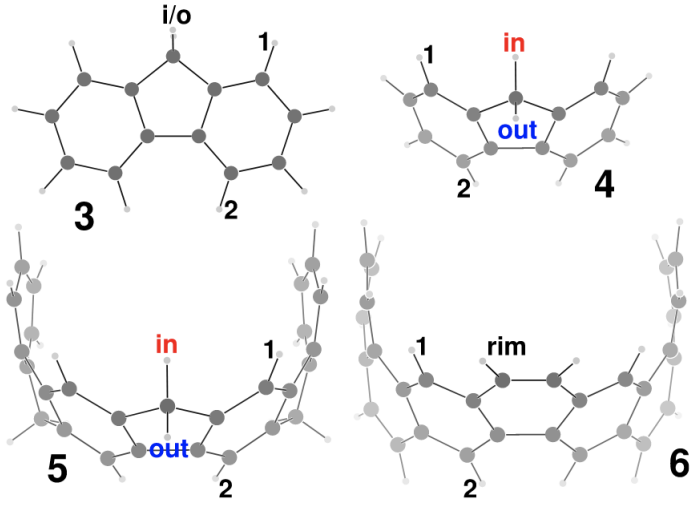

Figure 5.4: Fluorene **3**, Folded Fluorene **4**, Half Nanobelts **5** and **6**.

by cutting out the fragments from MB[6]CPP without further geometry optimization, apart from adding hydrogen atoms to saturate broken bonds. Calculations of proton chemical shifts of **3**−**5** have been carried out at the same levels of theory as above. As

Table 5.2: CSGT-BCP ^{1}H NMR δ's in ppm at the B97-2/6-311+G(2d,p) level

mol	H_{ar1}	H_{ar2}	H_{in}	H_{out}
3	7.56	7.87	3.78	3.78
4	7.39	7.50	3.18	4.28
5	7.27	7.29	3.01	4.11

can be observed in Table 5.2 passing from **3** to **4**, the bending induces effects on all the protons. The most impressive is the splitting of the methylene proton signals in opposite directions: the inner proton moves upfield by nearly 0.6 ppm, while the outer proton moves downfield by about 0.5 ppm. Ignoring for now the magnitude of this very large separation of 1.1 ppm, this corresponds to the relative position of the signals, where the inner proton is more shielded than the outer one. A second effect that can be observed is on the aromatic protons, both of which undergo an upfield shift ranging within 0.2−0.4 ppm. These effects can be readily explained as follows. First, looking at the folded structures, it is easy to recognize the different exposures of the methylene protons to the diamagnetic ring current of the two proximal benzene rings: H_{in} going inside the shielding zones and H_{out} going outside. Second, the decreased conjugation reduces the strength of the benzene ring current with a consequent upfield shift of the aromatic proton signals. This picture is nicely consolidated in **5**, where the aromatic proton signals get closer to each other and move a little further upfield and the methylene proton chemical shifts reach presumably their final values in the absence of the paramagnetic belt current, 1.1 ppm apart. Next, to see if any computationally less intensive method could be found to estimate as close as possible the effect of the paramagnetic belt current, we have considered the few electron model by Steiner and Fowler,[45, 46] calculating the orbital contributions to the current strength for the bond connecting the benzene rings along the cycloparaphenylene nanohoop, induced by a magnetic field parallel to the main symmetry axis, due to the HOMO, HOMO-1, ..., and so on. Of course, the full orbital sum gives the value reported in Figure 5.2, corresponding to 73% of benzene current strength (BCS). The hope is to find some stable value much before using only a few frontier orbitals, whose contribution to the current density would be a genuine feature of the belt. The result of the procedure is given in Figure 5.5. As expected, the A_{2g} HOMO alone gives a very large paratropic current strength equal to 138% of BCS, which is mainly due to virtual transitions to the LUMO and LUMO+1, both of A_{1g} symmetry. Adding the doubly degenerate E_u HOMO-1, the current strength remains paratropic but reduces to the 65% of BCS, as might be expected since a diatropic contribution is determined by the (x, y) translational symmetry of the virtual transitions to the LUMO and LUMO+1. Adding one more occupied orbital, i.e., the A_{2u} HOMO-2, the current strength rises to 67% of BCP, from virtual transitions to higher virtual orbitals, then it does not show any further change adding up to 12 more occupied MO's. This nice result now allows us to confidentially estimate the paratropic belt current effects as those arising from the four HOMO, HOMO-1 (doubly degenerate), and HOMO-2 only, which provide a stable current strength that closely matches the total one. Moreover, maps of the induced current density clearly show that the flow generated by these few orbitals is fully delocalized all over the belt, i.e., it is a genuine feature of the macrocycle.

In summary, it has been found that the effect due to the belt curvature alone would

provide, in general, ^{1}H δ's shifted to high field with respect to the experimental data. Such an effect is particularly evident for the methylene protons of MB[6]CPP, especially for the proton facing inside the belt, which is calculated more than 1 ppm up-field respect to the observed signal. Aromatic protons are also calculated to be shifted up-field to 0.8 ppm for MB[6]CPP. Application of the few electron model[45, 46] has permitted quantitative evaluation of the effect on the proton chemical shifts of the global paratropic belt current, induced by a magnetic perturbation parallel to the main molecular symmetry axis, predicted for these kinds of macrocycles [94, 95] but never proven, until now, on the basis of experimental results. The effect of such tubular paratropic currents result in a general but differentiate down-field shift, which brings all the calculated ^{1}H δ's in nice agreement with the experimental data. The methylene protons of the rigidified [6]cycloparaphenylene, whose NMR signals are the most affected by the two opposite effects, provide striking evidence for the presence of the paratropic belt-currents.

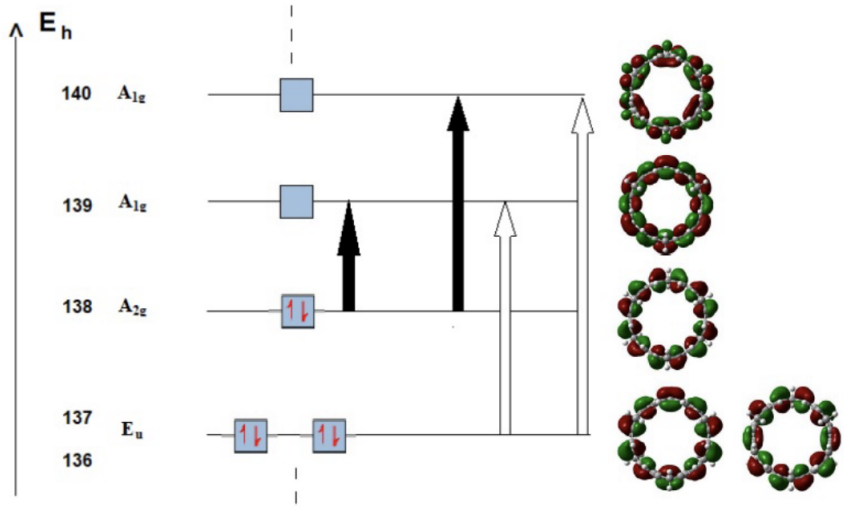

Figure 5.5: Contributions to total current density given only from frontier orbitals. White arrows indicate a diamagnetic current while black arrows a paramagnetic current.

5.1.2 On the JAP Method for the Indirect Determination of Delocalized Currents from Experimental Chemical Shifts

The much more ambitious goal of recovering a coarse-grained picture of the current density from experimental values has been recently advanced by Jirásek, Anderson and Peeks (JAP),[96] who estimated the global current strength in several macrocycles from the change of their proton chemical shifts recorded in solution over the proton chemical shifts of suitably chosen reference compounds, according to the simple intercept-free linear equation

$$\Delta\delta_i = \delta_{i,\mathrm{aro}} - \delta_{i,\mathrm{ref}} = \sigma_{i,\mathrm{ref}} - \sigma_{i,\mathrm{aro}} = \mathrm{RCGF}_i \frac{I}{B} \tag{5.29}$$

where I is the global current strength induced in linear regime by a magnetic field of modulus B, and, foreach magnetic nucleus i, the ring current geometric factor RCGF_i, first proposed in Ref.[97], is a function of the geometry of the molecule and of the circuits considered relevant for the non-localized part of the magnetic response. As with NICS-based works, the JAP approach comes with an internal validation, the ability of the model to reproduce the experimental $\Delta\delta_i$, but, due to the small number of experimental data (not to mention the far from trivial problem of identifying correct reference compounds) the possibility remains that JAP currents are not in agreement with reliable computations, and their meaning could then be questioned. *As the JAP approach could be of wide use in the realm of magnetic aromaticity, we deemed it necessary to assess its effectiveness, and we took the task of computing local and global current strengths for the systems considered in Ref.*[96]. From this analysis, we excluded cycloporphyrin nanorings, which have been object of a previous study.[98][**6**] The systems studied, labeled as in Ref.[96], are reported in Figure 5.6. Topologically, they are annulenes (**1,2**), nanohoops decorated by single rings (**3-7,12**) or by small polycycles (**8,10-11**), and a circulene, i.e. a swung-in-plane nanobelt (**9**), sometimes in different charge states. Magnetically induced currents have been obtained by SYSMOIC starting from wavefunction files (.wfx) obtained by Gaussian 16[56] run at the BHandHLYP/6-31G* level on geometries optimized at the same level. Global current strengths have been computed by integrating the current crossing a plane bisecting a C-C bond up to 10^{-3} atomic units (at this level the reference benzene ring current is -12.2 nA T^{-1}). Numerical results are collected in Table 5.3. Accurate determination of local currents is less straightforward, because the large areas associated to small integration thresholds can include contributions associated to different bonds and a criterion is needed to assign contributions to individual bonds. In this work local currents have been first obtained at the less demanding $2 \cdot 10^{-2}$ atomic units level (the reference benzene ring current reduces to -10.3 nA T^{-1}; percent values are reported in Figures 5.7, 5.8, 5.9, 5.10, 5.11 and 5.12 with or without the sketch of the integration domains, which are useful to grasp the shape of the currents). Current in percent units of the benzene current strength are only approximately preserved when different integration thresholds are used. As a correction for this error, best values of local signed current strength, have been obtained by the equation

$$\bar{I}_{\mathrm{corr},B} = \bar{I}^{(10^{-3})}_{\mathrm{global}} \frac{\bar{I}^{(2\cdot 10^{-2})}_{B}}{\bar{I}^{(2\cdot 10^{-2})}_{\mathrm{global}}} \tag{5.30}$$

Where do residual discrepancies come from? The Biot-Savart law, used to develop the equations of the model, is known to work exactly also in the quantum mechanical domain, provided the correct current density is used. Therefore, the problems can only come from

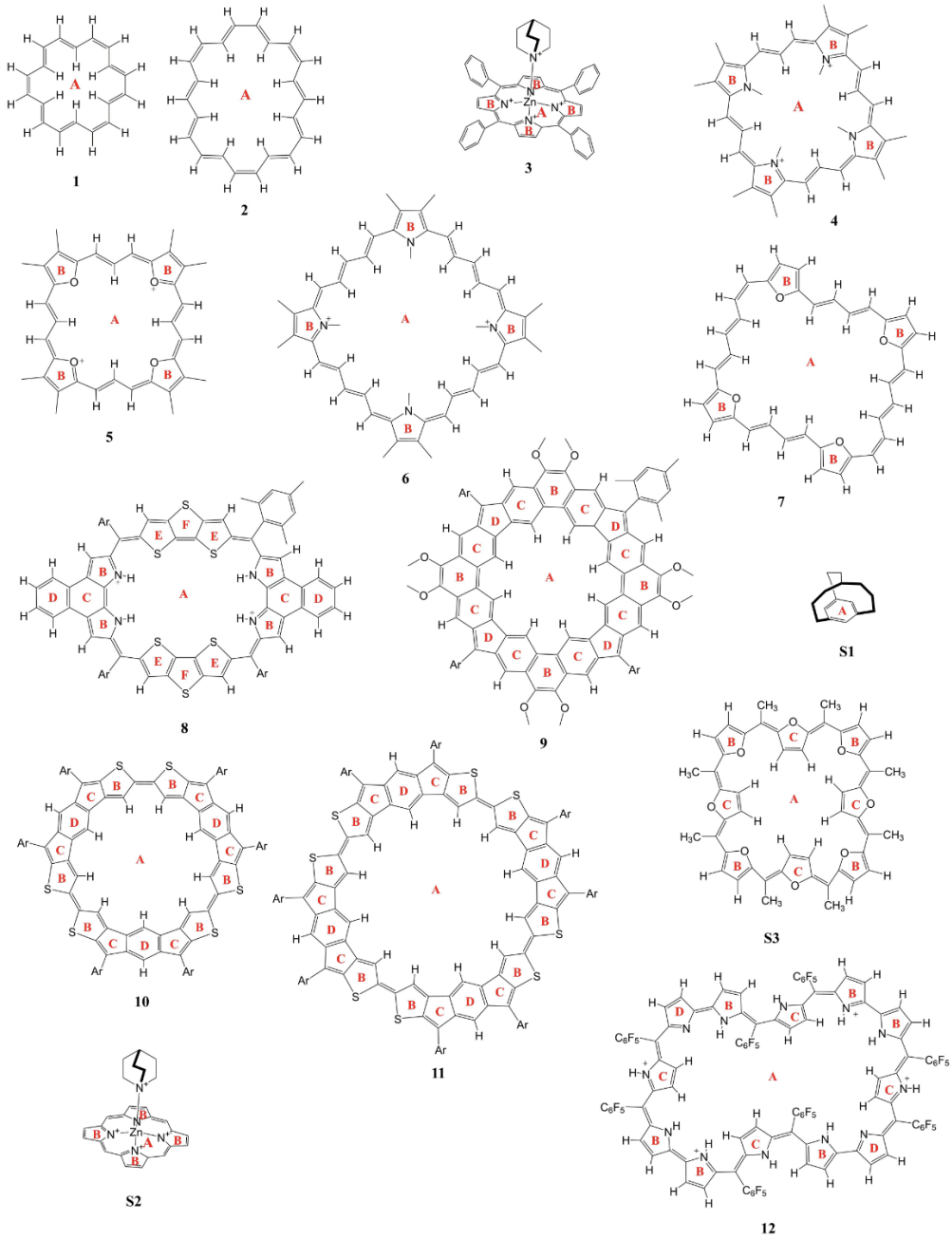

Figure 5.6: Molecules studied in this work.

Table 5.3: Signed current strengths (in nAT^{-1}) retrieved by the JAP method and by DFT calculations at the BHandHLYP/6-31G* level. R^2 is the coefficient of determination of the JAP linear model taken from Ref.[96]. %err is the percent error of the $\bar{I}_{JAP}$ over the $\bar{I}_{DFT}$ values. The fraction of rings whose tropicity is predicted correctly, ϕ^{ok}_{TROP}, is given in the last column.
[a] Non-optimized geometry taken from the crystal structure of Ref.[99]

	R^2	$\bar{I}_{JAP}$	$\bar{I}_{DFT}$	%err	ϕ^{ok}_{TROP}
1	0.97	−13.3	−13.3	0	1/1
2	0.97	−10.1	−8.4	20	1/1
3	0.98	−38.0	−25.1	51	2/2
$\mathbf{4}^{2+}$	0.99	−25.9	−38.5	−33	2/2
$\mathbf{5}^{2+}$	0.98	−26.6	−33.8	−21	2/2
$\mathbf{6}^{2+}$	0.99	−33.4	−25.2	33	2/2
$\mathbf{7}^{2+}$	0.96	−28.3	−27.6	3	2/2
$\mathbf{8}^{2+}$	0.97	−29.3	−25.1	17	3/6
$\mathbf{9}^{2+}$	0.91	−22.7	−36.9	−38	3/4
$\mathbf{10}^{2+}$	0.99	−20.1	−32.6	−38	3/4
$\mathbf{11}^{2+}$	0.99	−26.7	−43.1	−38	3/4
$\mathbf{12}^{4+}$	0.94	−33.0	−6.9	3787	1/4
$\mathbf{12}^{4+}$ [a]			−34.5	2	1/4
$\mathbf{9}^{2-}$	0.84	−12.9	−28.1	−54	3/4
$\mathbf{9}^{4-}$	0.23	5.0	1.8	178	1/4
10	0.88	8.6	11.8	−27	2/4
11	0.96	7.0	3.1	126	2/4
S1	0.96	−11.2	−9.3	20	1/1
S2	0.99	−29.8	−26.7	12	2/2
S3	0.94	5.1	2.1	50	2/3

the inadequate modeling of the current density. In this respect the assumptions of the JAP model can be summarized as follows:

- The macrocycle is assumed to have a single conformation, built upon gas-phase B3LYP/6-31G* optimization starting from the crystallographic structure (geometry can be a problem!);
- the contributions to the shielding of the i-th spectator atom coming from different directions of the external field are weighted by the net projected cross-section area of the circuit along the direction of the applied magnetic field (strictly correct for planar monocycles only!);
- the shape of the current is that of two infinitely thin homotropic circuits displaced from the average local plane by ± 0.7 Å (heterotropic circulations do occur in cycloporphyrins!);
- local currents are preserved passing from the reference compounds to the studied macrocycles (does not seem the case);
- delocalized currents run along one or few equally weighted piecewise linear pathways running along selected conjugated circuits running all along the macrocycle (problematic for localized patterns. Extension of the model to fit more than a ring current proved cumbersome, due to heavy correlation of the fit parameters, but good results were obtained in the case of $\mathbf{9}^{4-}$.);

In conclusion, we have performed a check of the ability of JAP model to recover DFT ring currents, which can be nowadays computed with user-friendly automated software. The model is effective in recovering global and local tropicities, but errors of the order of a full benzene ring current can occur. In percentage terms, the largest error has been reported for a calculation on $\mathbf{12}^{4+}$ and for $\mathbf{9}^{4-}$, a system with a negligible global ring current, dominated by local currents. Extension of the model to fit more than a ring current proved cumbersome, due to heavy correlation of the fit-parameters, but good results were obtained in the case of $\mathbf{9}^{4-}$. The application of a similar approach to other systems will be non-trivial, not only because of the strong correlation of the parameters, but also because choosing the proper reference system can be complicated, especially in bent systems, so that presently the indirect route of retrieving the current density from few experimental chemical shifts should still be considered a rough and challenging road.

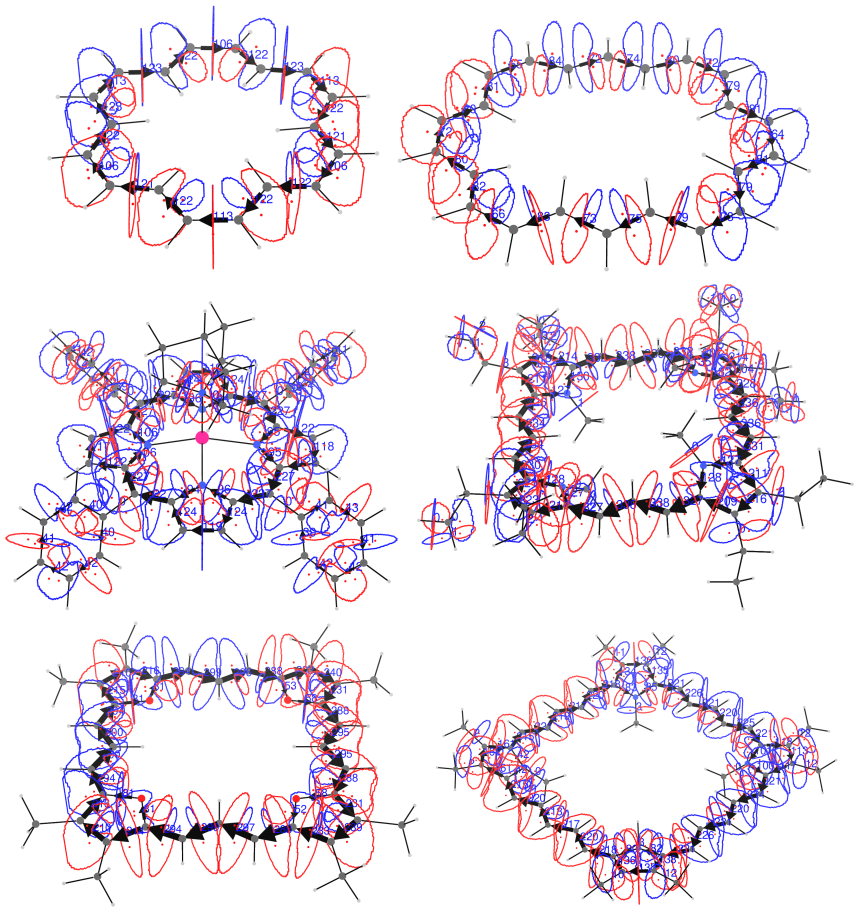

Figure 5.7: Integration domains used to determine the bond current strengths for molecules **1**, **2**, $\mathbf{3}^{2+}$, $\mathbf{4}^{2+}$, $\mathbf{5}^{2+}$ and $\mathbf{6}^{2+}$. The domains are bounded by contour lines at 2×10^{-2} a.u.

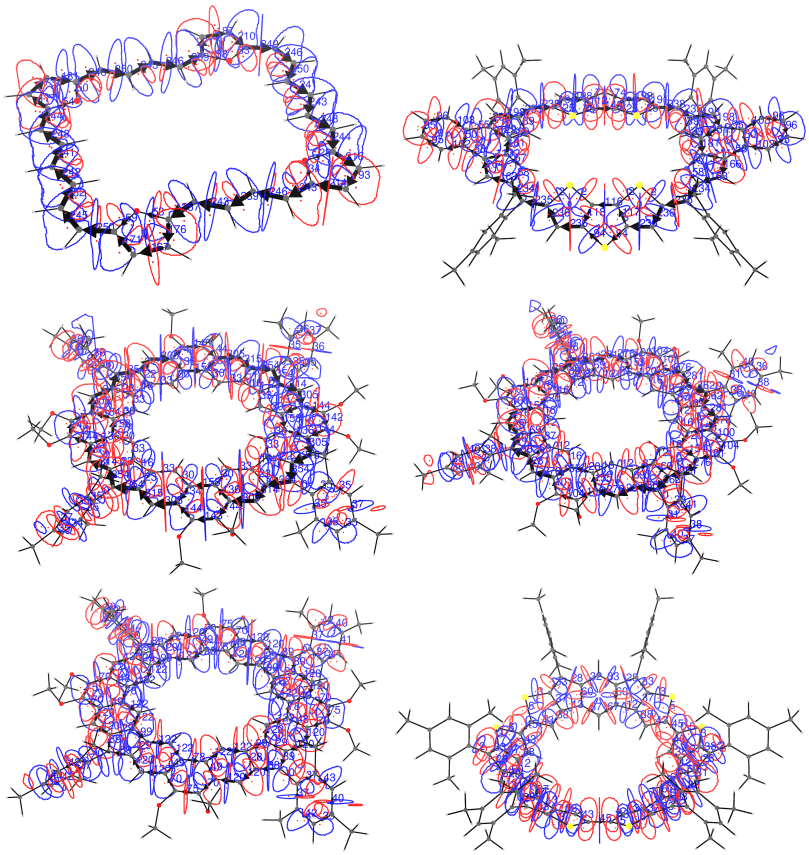

Figure 5.8: Integration domains used to determine the bond current strengths for molecules $\mathbf{7}^{2+}$, $\mathbf{8}^{2+}$, $\mathbf{9}^{2+}$, $\mathbf{9}^{2-}$, $\mathbf{9}^{4-}$ and **10**. The domains are bounded by contour lines at 2×10^{-2} a.u.

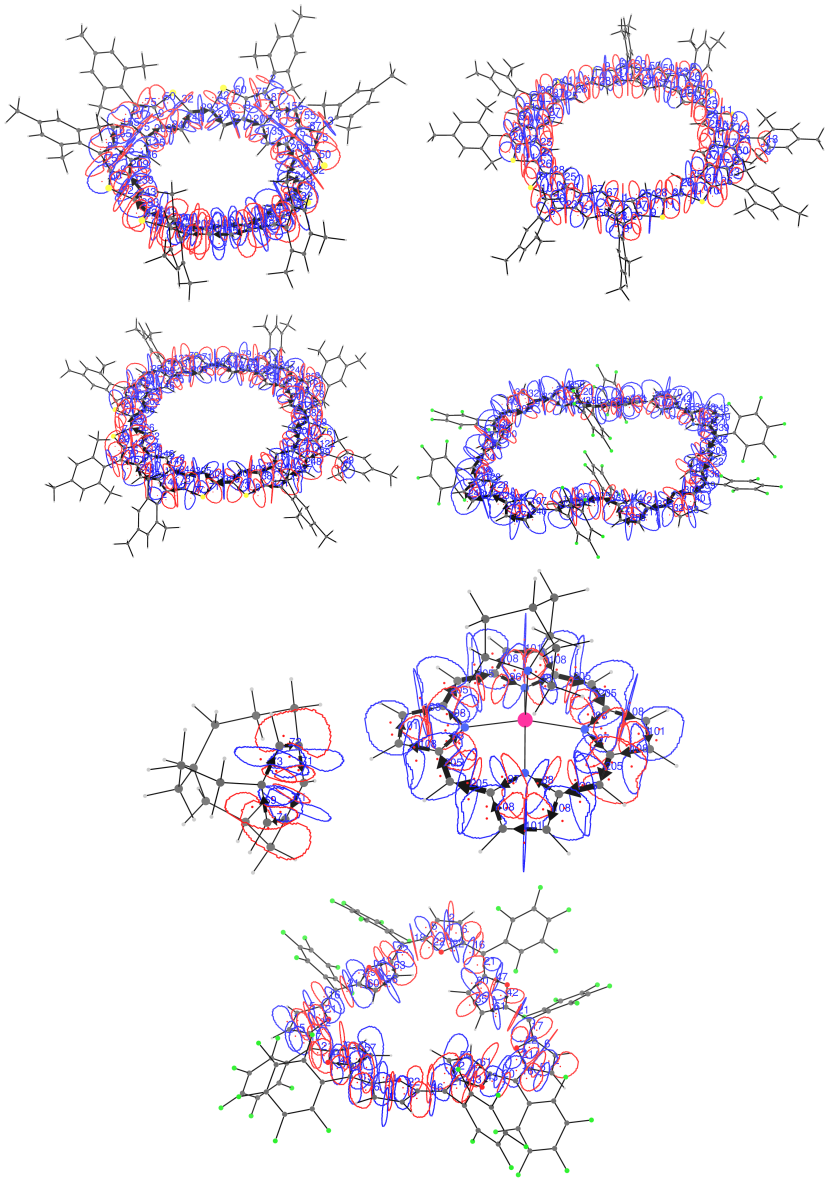

Figure 5.9: Integration domains used to determine the bond current strengths for molecules $\mathbf{10}^{2+}$, **11**, $\mathbf{11}^{2+}$, $\mathbf{12}^{4+}$, **s1**, **s2** and **s3**. The domains are bounded by contour lines at 2×10^{-2} a.u.

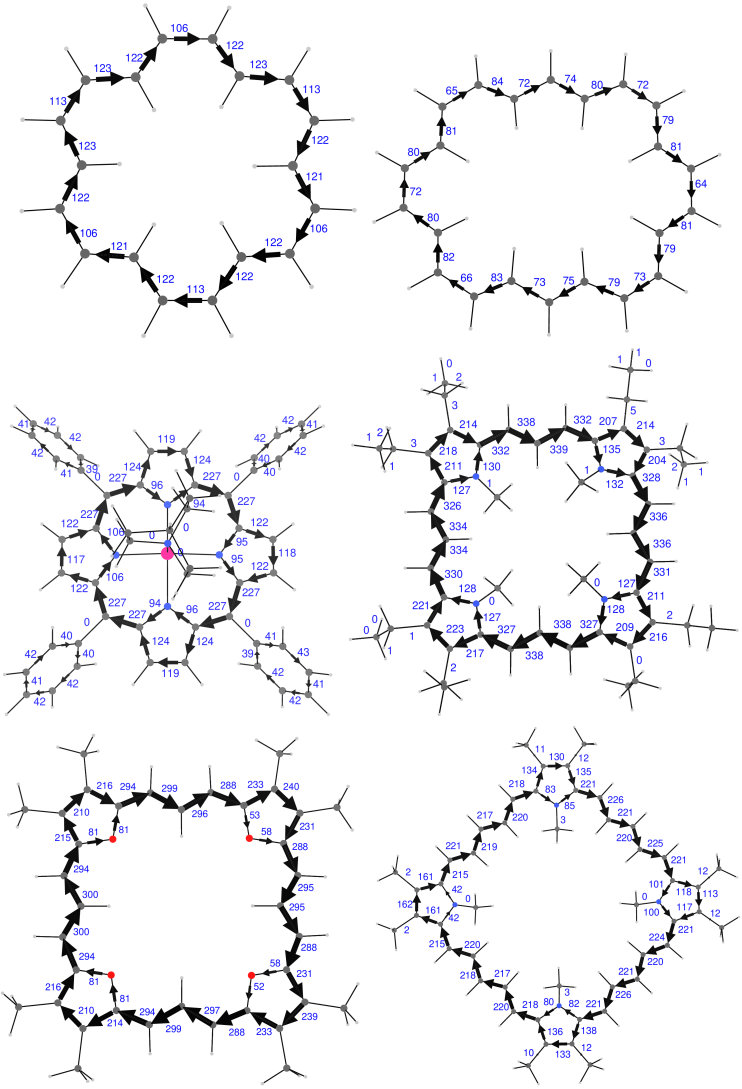

Figure 5.10: Relative bond current strengths obtained with the integration domains of molecules in picture 5.7.

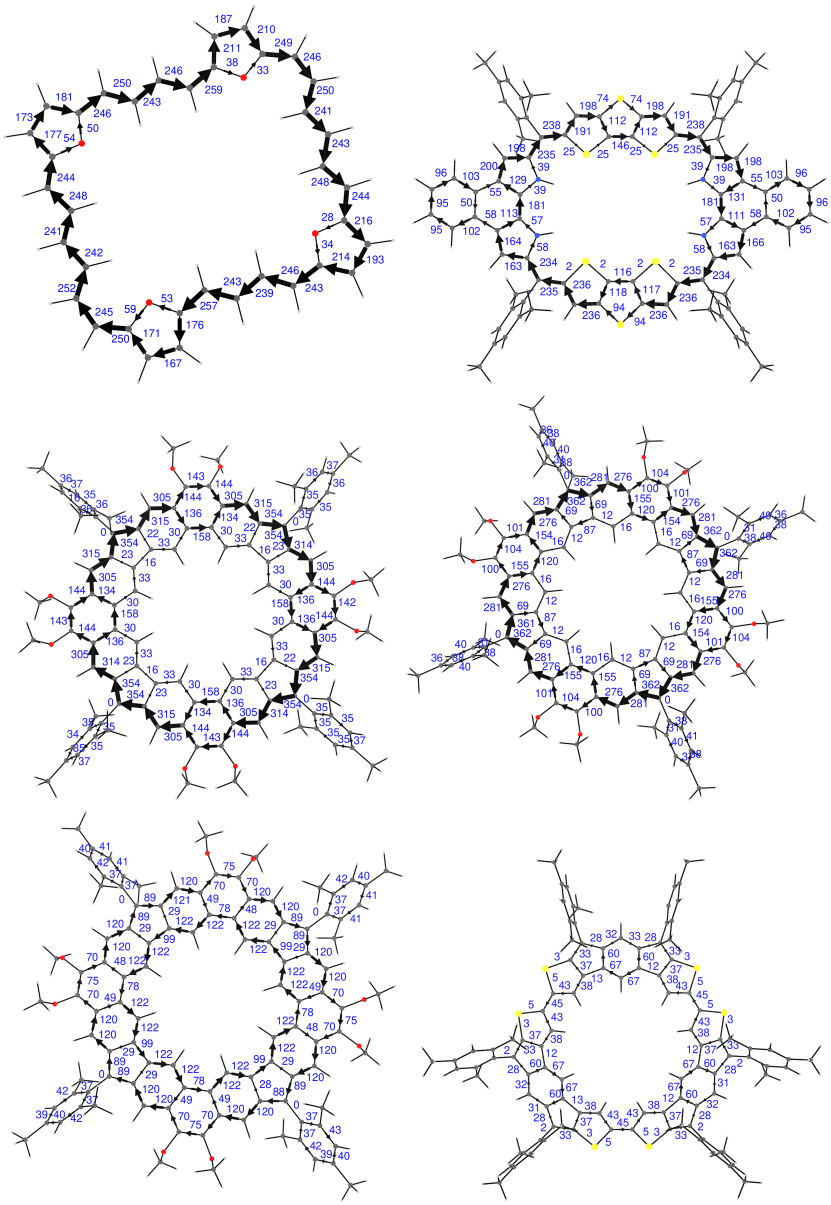

Figure 5.11: Relative bond current strengths obtained with the integration domains of molecules in picture 5.8.

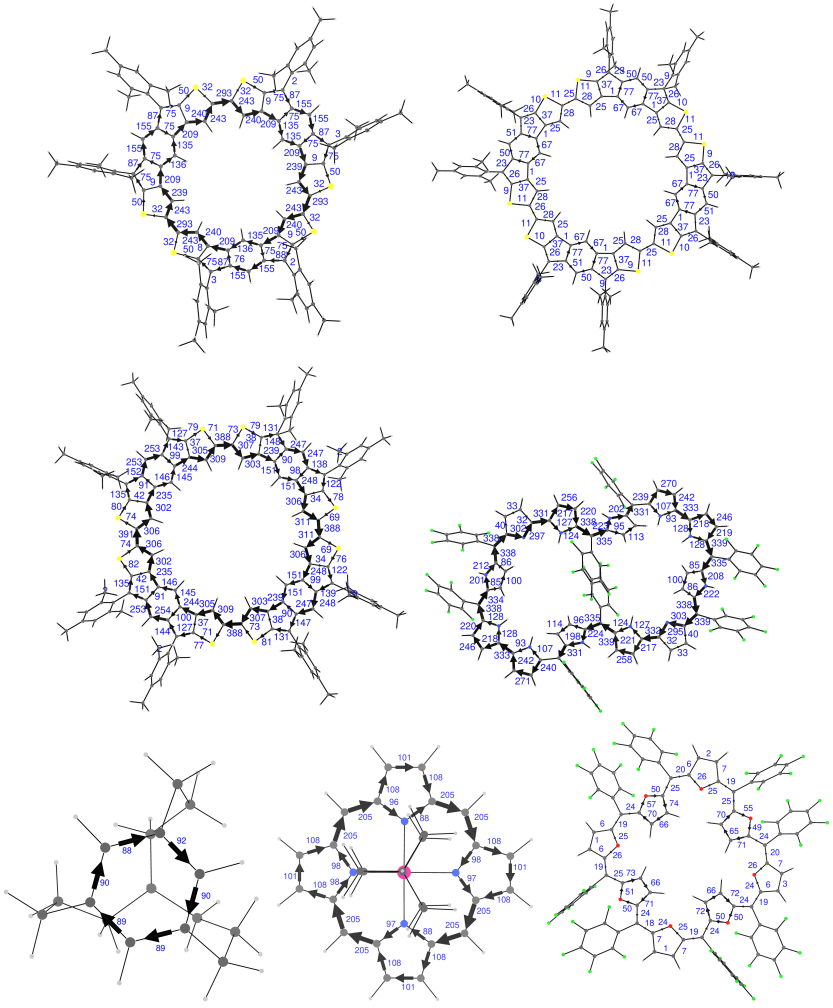

Figure 5.12: Relative bond current strengths obtained with the integration domains of molecules in picture 5.9.

5.1.3 Magnetic Characterization of the Infinitene Molecule

The large family of polycyclic aromatic hydrocarbons (PAHs) has recently acquired a new member referred to as infinitene due to its helically twisted structure resembling that of the ∞ symbol.[100] Even at first glance, infinitene looks as a truly fascinating molecule, in particular with regard to some issues concerning the nature of its aromaticity in terms of the magnetic criterion.[101] In fact, beside enhanced stability, specific reactivity and bond equalization, it is well recognized that the magnetically induced current density is intimately linked with the aromaticity concept and it is an essential ingredient for the interpretation of the magnetic response of conjugated π-systems, such as the nuclear magnetic shielding in NMR spectroscopy and the exaltation of diamagnetism.[102, 103] However, despite recent progress,[96, 104] the inference of the actual shape of the ring current in PAHs, starting from ^{1}H NMR data or the calculations of a few nucleus independent chemical shifts (NICSs)[105] is not straightforward, and this is especially true for curved PAHs.

Infinitene can be seen as two cleaved coronene ([6]circulene) subunits, twisted as two homochiral helices and stitched together by both their ends, in such a way that the rim of one coronene is attached to the hub of the other, forming two circuits of equal length containing 24 carbon atoms each. For coronene it is known that two counter-rotating ring currents are induced by a perpendicular magnetic field, one strongly diatropic on the rim, another weakly paratropic on the hub, which provide evidence for a resultant global aromaticity of the molecule.[106]

Therefore, a number of questions concerning the shape and strength of ring currents (if any) arise:

i) What pathways do the currents travel through?

ii) Are they global, or local to Clar sextets?

iii) Which tropicity do they display?

iv) How does their strength compare with the benzene ring current?

v) How large is the exaltation of diamagnetism for this aromatic molecule?

vi) How can the high-field ^{1}H NMR signals be justified on the basis of the actual current tropicity?

Nowadays, there exist powerful methods that can be readily used to solve the problem by calculating directly the magnetically induced current density for any orientation of the inducing magnetic field.[14, 107] Therefore, not at all surprisingly, despite the work of synthesis was very recent,[100] a theoretical paper elucidating the current pathways in infinitene has already appeared,[108] when our study was still in progress. In that work it has been clearly shown that the induced current is characterized by two aromatic, non-intersecting global π-electron current pathways, formed by the two circuits of 24 carbon atoms along the edges shaped as the infinite symbol. This finding answers the first three of the above questions. Besides, it addresses the question whether the molecule follows Hückel $4n + 2$ or Möbius $4n$ aromaticity rules, showing that infinitene does not belong to any of these classes of molecules. Nonetheless, the last three questions remain.

Experimental ^{1}H NMR spectrum of infinitene presents six doublet peaks within the aromatic region (from 6.4 to 8.2 ppm) which have been successfully assigned to the various kinds of protons on the basis of a very good comparison with calculated chemical shifts at the GIAO-DFT/B3LYP/6-311+G(2d,p) level of theory in $CHCl_3$ with an SMD

solvent model.[100] It was suggested that it is reasonable to attribute the larger shielding of the protons attached to the central naphthalene (H_a and H_b, same labeling as in Ref. [100]) to an effect from the ring current on a lower benzene ring. No other argument was given supporting this idea. To better understand the behavior of this molecule we have taken the geometry of the (P,P)-isomer of infinitene, optimized at the PBE0/6-311+G(d,p) level of theory in the gas phase, reported by Krzeszewski et al.[100] within the Supporting Information file. The symmetry point group of the structure is D_2 with the Cartesian x axis perpendicular to the central C-C bonds of the stacked naphthalene subunits. Then, we have performed the calculation of the magnetically induced current density using the CTOCD-DZ method to ensure origin independent results, adopting the B97-2[109]/6-311+G(2d,p)[110] level of theory in the gas phase. The Gaussian 16 program[56] was used to obtain the perturbed molecular orbitals with the CSGT[55] keyword and the SYSMOIC program package[14][**3**] to perform the actual calculation of the current density. In infinitene σ/π orbital separation is not strictly possible. However, descendants of p-orbitals can be easily detected using a combination of symmetry arguments and by inspection. The 156 doubly occupied molecular orbitals of D_2 infinitene can be partitioned into 48 1s cores plus 84 σ orbitals, spanning the symmetries

$$\Gamma_{\mathrm{core}+\sigma} = 35\mathrm{A} \oplus 34\mathrm{B}_1 \oplus 31\mathrm{B}_2 \oplus 32\mathrm{B}_3, \tag{5.31}$$

and 24 more orbitals that can be tentatively classified as π orbitals

$$\Gamma_{\pi} = 6\mathrm{A} \oplus 5\mathrm{B}_1 \oplus 6\mathrm{B}_2 \oplus 7\mathrm{B}_3. \tag{5.32}$$

Using some facilities contained in the SYSMOIC package, we have readily identified the set composed by HOMO, HOMO-1, HOMO-2, ..., HOMO-14 plus HOMO-17 as nearly true π orbitals, as confirmed by inspection with GaussView. Searching for the remaining 8 orbitals was unsuccessful due to large σ/π mixing. Then, only HOMO,...,HOMO-14 plus HOMO-17 have been used in the calculation of the current density map induced in the π-electron cloud. The calculated CTOCD-DZ π-electron current density, induced by a unitary magnetic field parallel to the Cartesian x axis, is shown in Figure 5.13. Considering that the typical benzene ring current has a maximum value of about 0.08 a.u.[111], we have applied a lower/higher cutoff of 0.05/0.1 a.u. to the current density values calculated over a grid of $12 \times 20 \times 28$ a_0 in step of 0.4 a_0. As can be observed, the result is impressively clear and in full agreement with the current pathways reported in Ref.[108]. Two distinct current flows can be seen to occur along the equivalent circuits of 24 carbon atoms, each one formed by all the K-regions of a coronene subunit plus the internal fjord region of the second coronene subunit. Looking carefully, the two global ring currents are really disjointed, as already noted, since along the radial bond of the coronene subunits the current goes in opposite directions. As can be observed, the homotropicity of the current pathways is a direct consequence of the magnetic symmetry group,[63] which can be worked out according to Tavger and Zaitsev.[64] Actually, when the magnetic field is parallel to C_2^x, the magnetic group is $D_2(C_2^x) = (E\ C_2^x\ RC_2^y\ RC_2^z)$, where R is the time reversal operator. Every symmetry element can be easily seen looking at the current density field depicted in Figure 5.13. This qualitative result is confirmed by the quantitative representation given by the calculated all-electron bond current strengths[12] reported in the bottom inset of Figure 5.14. The two insets in the top of Figure 5.14 have been calculated separating the contribution given by the set of 16 orbitals identified as nearly true π orbitals (top left) and the contribution given by all the remaining 140 orbitals (top right), which includes also the 8 orbitals showing a large σ/π mixing. What is shown in the top right inset of Figure 5.14 can be due to delocalized

currents coming from σ-electrons, which are known to be somewhat less than 10% of the total current in benzene,[13] but also to the residual σ/π mixing. At any rate, in the bottom inset of Figure 5.14 a real representation is given of the current delocalization, which is not affected by any ambiguous assumption. As can be observed, the current strength along the terminal K-regions is about 92% the benzene current strength, it increases in the intermediate K-regions and reaches a maximum of 111% within the fjord regions. The current strength for the radial bonds of the coronene subunits is vanishing for all those bonds which are interchanged by C_2 symmetry elements and is not larger than 0.5 nA/T in all other cases. This shows quantitatively the disconnection of the two global ring currents.

Given the particular form of the current density, in which there are no ring currents localized on benzene rings, we have considered a different explanation to attribute the larger shielding of the protons attached to the central naphthalene. To see that, we

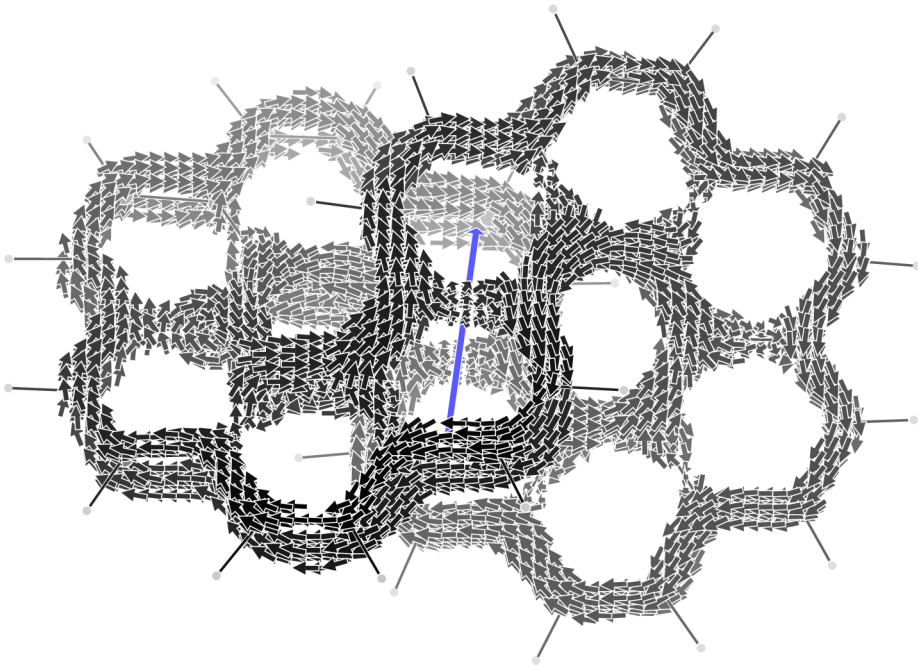

Figure 5.13: π-electron current density induced in infinitene by a unitary magnetic field (blue arrow) parallel to x Cartesian axis, corresponding to C_2^x symmetry element. The other two binary axes of D_2 must be combined with the time reversal operator. Currents lower/higher than 0.05/0.1 a.u. are not shown.

have computed the spatial contributions to the ^{1}H NMR magnetic shieldings, at the CSGT/B97-2/6-311+G(2d,1p) level, using the method proposed by Jinger et al.[113] For the application of this method, integration of the magnetic shielding density function[6] has to be performed adopting Becke's partition scheme for the calculation of molecular integrals.[53] Due to the fairly high sensitivity of the atomic contributions on the atomic size adjustments chosen to decompose the molecular space,[54][**1**] the BCP positions of the electron density gradient[29] have been used to define the heteronuclear cutoff profiles.[114][**9**] In planar aromatics the out-of-plane component of the nuclear magnetic shielding tensor is the one of major interest. Owing to the disjointed global current

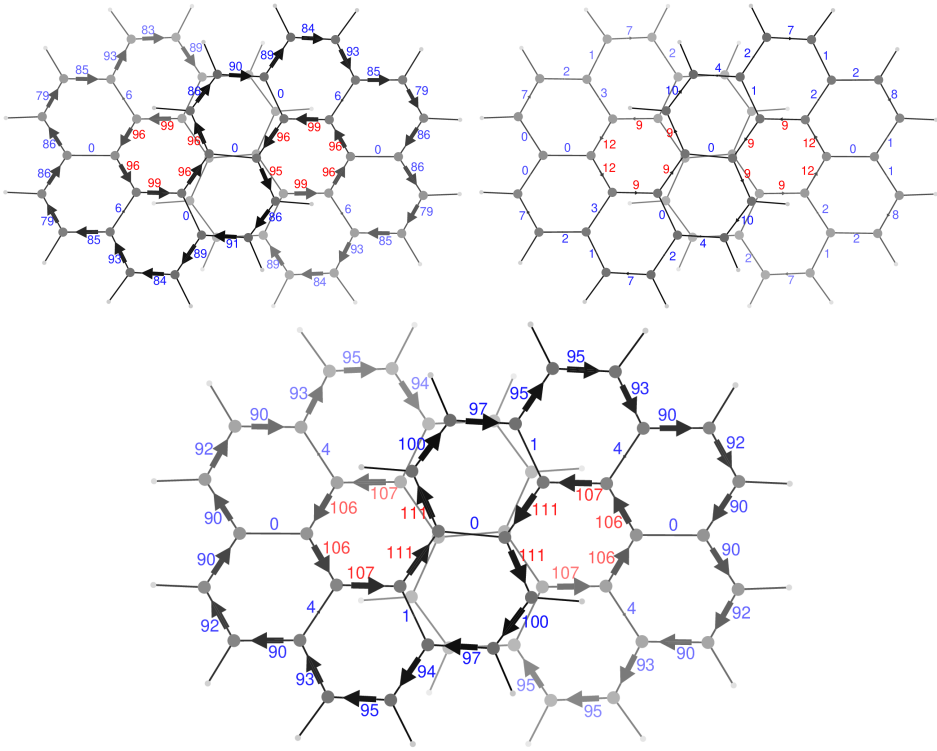

Figure 5.14: Calculated bond current strengths in infinitene. Top left π-electron contribution from the orbital set used to compute Figure 5.13; top right contribution from all the remaining orbitals; bottom all-electrons. See caption of Figure 5.13 for the orientation of the inducing magnetic field. Figures attached to each arrow give the current strength in percentage respect to the benzene ring current strength of 12.0 nA/T taken as reference.[112]

density induced by a magnetic field parallel to the x direction a similar importance is expected to occur for the xx component of the tensor. Therefore, we have focused our attention on both the xx and isotropic component of the proton magnetic shieldings. Results are assembled in Figure 5.15 formed by six insets, one for each symmetry unique

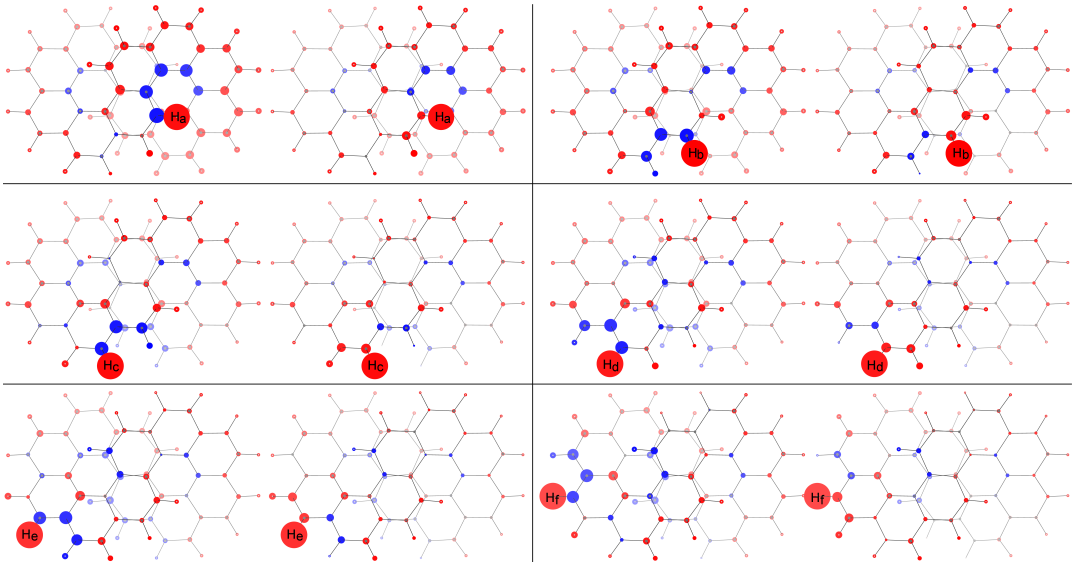

Figure 5.15: Spatial contributions to the proton magnetic shieldings. See text for details.

proton of the molecule (same labeling as in Ref. [100]). In each inset, contributions to the xx component of the tensor are plotted on the left beside the contributions to the isotropic component (tensor average value) on the right. Spatial contributions are represented as spheres of radius proportional to the cubic root of the calculated value and centered on the corresponding nucleus. Shielding/deshielding contributions are shown in red/blue. According to the Biot-Savart law[15] the current effect decreases with the square of the distance. Moreover, closed current loops around atomic nuclei or centered on chemical bond, that do not cover the reference position, provide negligible effects irrespective of their strength. Following this key of interpretation, common to all protons it can be seen that:

i) a main shielding contribution (core contribution) is given by the molecular region around each proton;

ii) the nearest atoms provide the next important contributions;

iii) sizable contributions come from atoms at intermediate distances, or even far away, as a consequence of the globally delocalized current;

iv) the contribution given by the bonded carbon atom to the xx component of the magnetic shielding is always negative (deshielding), which turns always positive (shielding) for the isotropic component;

v) large deshielding contributions from the next nearest atoms are negative in both xx and isotropic components;

vi) with the exception of the attached carbon atom and some very minor ones, the isotropic values closely resemble the xx contributions, revealing the dominant role played by the delocalized current, even if moderated to some extent by the perpendicular components.

It can be observed that all pictures for protons H_c, H_d, H_e, and H_f (see middle and bottom rows of Figure 5.15) show similar features. For H_b there are larger contributions coming from lower benzene rings. For H_a the picture is completely different, showing important deshielding contributions from the carbon atoms forming the fjord region plus a crown of shielding contributions all along the rim of the coronene subunit in which the proton is inserted. To deal with such a complex situation, we have collected in Table 5.4 the core contribution and the sum of all shielding (positive) and deshielding (negative) spatial contributions to the isotropic component of the magnetic shielding of the infinitene protons.

Table 5.4: Contributions to the isotropic component of the proton magnetic shieldings: core, sum of shielding spatial contributions (SSSC), sum of deshielding spatial contributions (SDSC), and proton net charges q_H.

Proton	core	SSSC	SDSC	total	δ_{cal}	δ_{Expt}[100]	q_H
H_a	18.85	8.91	−3.41	24.35	7.14	6.99	0.1675
H_b	19.83	6.95	−1.74	25.04	6.44	6.43	0.1320
H_c	19.76	5.79	−1.70	23.86	7.62	7.60	0.1387
H_d	19.79	5.49	−1.88	23.41	8.08	8.04	0.1385
H_e	19.76	5.36	−1.88	23.24	8.24	8.18	0.1398
H_f	19.78	5.25	−1.76	23.27	8.22	8.16	0.1433

Total values have also been transformed to calculated chemical shifts δ_{cal} relative to TMS using[115]

$$\delta_i = \sigma_{ref} - \sigma_i + \delta_{ref} \tag{5.33}$$

where σ_{ref} is the computed shielding constant for the same nucleus in a reference compound, σ_i is the computed shielding constant for the nucleus in the molecule of interest and δ_{ref} is the experimental chemical shift for the reference compound relative to TMS. For aromatic protons we use C_6H_6 as the reference compound, adopting $\delta_{ref} = 7.36$ ppm in $CDCl_3$.[116] First of all, we note the good comparison with experimental chemical shifts:[100] the order of the signals is correctly computed and the largest deviation is only 0.15 ppm for H_a. Looking at the core contributions, it can be observed that protons c,d,e,f show almost the same value (max deviation 0.03 ppm), indicating a very similar internal region. The same protons display a decreasing sum of shielding spatial contributions (SSSC) going from H_c to H_f ($\Delta\sigma = 0.54$ ppm) in parallel with a decreasing sum of deshielding spatial contributions (SDSC), H_f apart which deviates a little from this tendency. This behavior changes a lot for H_a and H_b. The latter shows an SSSC equal to 6.95 ppm, which surpasses by 1.16 ppm the value relative to H_c, accounting quantitatively for the $\delta_{Expt}(H_c) - \delta_{Expt}(H_b) = 1.17$ ppm. This increment of the SSSC can be traced back to the somewhat larger shielding contributions from the carbon atoms of the lower benzene rings and from the K-regions of the coronene subunit, visible in top row of Figure 5.15 on the right. As regards H_a everything is changed: the core contribution is the smallest, whilst in absolute value both SSSC and SDSC are the largest. This leads to cross compensations, which collocates the H_a chemical shift midway between H_b and H_c. Looking at Figure 5.15, top row on the left, it is possible to locate the source of the

largest deshielding on the carbon atoms forming the fjord and the source of the largest shielding on the carbons in the lower benzene rings and K-regions as well. In other words, seen along the x-axis, H_a is inside two counter-rotating currents and undergoes their opposite effects, i.e., the paratropic one giving a deshielding effect, the diatropic one giving a shielding effect. The smaller core contribution can be attributed to a loss of electron charge in the immediate region around the nucleus, which is compatible with the calculated Mulliken populations, showing that the four H_a's have the highest positive charge within the set of hydrogen atoms. It is known that upon formation of CH-π interactions, the hydrogen loses electrons.[117]

Returning to the unsolved questions underlined before for infinitene, we have shown that: iv) as for the strength of the current, induced by a perturbing magnetic field perpendicular to the central C-C bonds of the two stacked naphthalene subunits, in the K-regions it is 1.5 times weaker than the diatropic current that circulates on a pristine coronene rim, whilst in the fjord the current is twice stronger than the paratropic current on a pristine coronene hub; v) the exaltation of diamagnetism is fairly low, being only 73% of the expected value; vi) the high-field ^{1}H NMR signals are due to the global currents flowing on the fjord region and on the carbon atoms on the lower benzene rings and K-edges, with a fairly large deshielding effect on H_a, from the former, and shielding effect on both H_a and H_b from the latter.

5.2 Time-Dependent Magnetically Induced Current Density and Origin Invariant Optical Rotatory Power Density

In this section the aim is to illustrate how it is possible to implement the origin independent isotropic optical rotation power density defined according to equation (4.87), starting from the implementation of the time dependent magnetically induced current density according to the definitions given in section 4.4. To implement the CTOCD-DZ dynamic current density tensor the procedure to follow is exactly the same as the one given in section 5.1. The only difference is that the vectors (5.1) and (5.2) are now redefined accordingly

$$\Psi_a^{L_\beta}(\boldsymbol{r}, \boldsymbol{X}_1, \omega) = \frac{1}{\hbar} \sum_{j \neq a} \frac{\omega_{ja}}{\omega_{ja}^2 - \omega^2} \Psi_j^{(0)}(\boldsymbol{r}, \boldsymbol{X}_1) \left\langle j \left| \hat{L}_\beta \right| a \right\rangle \tag{5.34}$$

$$\Psi_a^{P_\delta}(\boldsymbol{r}, \boldsymbol{X}_1, \omega) = \frac{1}{\hbar} \sum_{j \neq a} \frac{\omega_{ja}}{\omega_{ja}^2 - \omega^2} \Psi_j^{(0)}(\boldsymbol{r}, \boldsymbol{X}_1) \left\langle j \left| \hat{P}_\delta \right| a \right\rangle \tag{5.35}$$

This means also that the previous equations (5.9) and (5.10) now depend on the radiation frequency ω

$$\Psi_a^{(\boldsymbol{r}\times\boldsymbol{\nabla})_\beta}(\boldsymbol{r}, \boldsymbol{X}_1, \omega) = \sum_{j \neq a} \frac{\omega_{ja}}{\omega_{ja}^2 - \omega^2} \left\langle j \left| \sum_k \left[(\boldsymbol{r} \times \boldsymbol{\nabla})_\beta \right]_k \right| a \right\rangle \Psi_j^{(0)}(\boldsymbol{r}, \boldsymbol{X}_1) \tag{5.36}$$

$$\Psi_a^{\nabla_\delta}(\boldsymbol{r}, \boldsymbol{X}_1, \omega) = \sum_{j \neq a} \frac{\omega_{ja}}{\omega_{ja}^2 - \omega^2} \left\langle j \left| \sum_k (\nabla_\delta)_k \right| a \right\rangle \Psi_j^{(0)}(\boldsymbol{r}, \boldsymbol{X}_1) \tag{5.37}$$

From a practical point of view, we have that the perturbed coefficients introduced in the section 5.1 and consequently the perturbed density matrices now depend on the radiation frequency, and to compute them we can use RPA at the HF or DFT level of theory, equivalent to TDHF[118] and TDDFT.[119, 120] As noted before for the static case, these coefficients can be obtained directly using SYSMOIC at the HF level of theory for closed shell systems, or from a Gaussian 16 calculation using the interfaces provided within the program. Examples of applications of these equations, that are given in Refs.[88][**4**] and [121][**11**], for the calculation of origin independent optical rotatory power density and time-dependent magnetically induced current densities in the CTOCD-DZ approach, are illustrated in the following subsections respectively for H_2O_2 and for LiH changing the frequency of radiation ω.

5.2.1 Origin-Invariant MEMDP Density

We have studied how Mixed Electric Dipole Magnetic Dipole Polarizability (MEMDP) density equation (4.87) varies with respect to internal rotation. For this purpose, we have calculated the optical rotation density in the CTOCD-DZ formalism for a selection of dihedral angles at the wavelength of 355 nm for the H_2O_2 molecule. Five dihedral angles are of interest, i.e., the two at which the optical rotation is maximum ($\delta \sim 60°$) and minimum ($\delta \sim 150°$), the angle at which optical rotation changes sign ($\delta \sim 120°$), in addition to $\delta = 0°$ and $\delta = 180°$, corresponding to C_{2v} and C_{2h} structures, respectively. The conventional specific rotation

$$[\alpha]_\lambda = \frac{28800\pi^2 N_\mathrm{A}}{\lambda^2 M}\beta \tag{5.38}$$

in the usual deg [dm g/cm^3]$^{-1}$ units, when the radiation wavelength λ is in cm, the molecular mass M in g mol^{-1} and $\beta = \mathrm{Tr}(\boldsymbol{\kappa}')/(3\omega)$ in cm^4, can be obtained as a volumetric integral of the MEMDP density. In Figure 5.16 the specific rotation is reported as a function of the dihedral angle. Computed optical rotation densities for the selected δ's

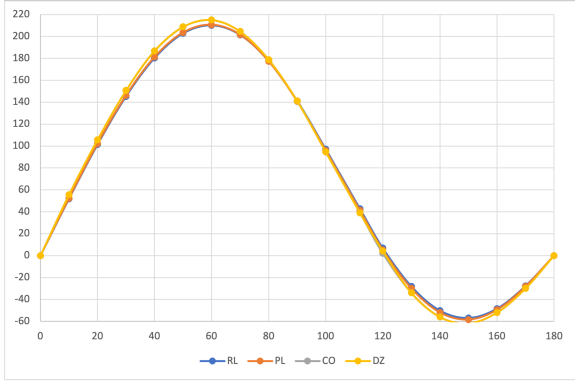

Figure 5.16: Specific rotation of the R_a enantiomer of H_2O_2, $\lambda = 355$ nm, as a function of the dihedral angle for the MEMDP. See Figure 5.17 for other details.

are shown as diverging color maps in Figure 5.17, for planes containing the oxygen atoms, parallel (left) and perpendicular (right) to the C_2 symmetry axis. Positive/negative density values are red/blue. As can be observed, the specific rotation density is mainly located in the vicinity of oxygen atoms, with conspicuous alternation of sign.

At $\delta = 0°$ and $\delta = 180°$ the symmetry of density maps is consistent with obviously vanishing optical rotation. In particular, the specific rotation density changes sign by reflection through a symmetry plane and vanishes at all its points. This is the typical feature of the scalar product between a polar vector and an axial vector. For $\delta = 0°$ two such planes are present, i.e., σ_v and σ'_v, for $\delta = 180°$ only σ_h is present. For all the intermediate conformers, the absence of symmetry planes gives rise to positive and negative regions which do not cancel one another out. At $\delta = 60°$ a red (positive) contribution is dominant over the plane containing the C_2 axis; at $\delta = 150°$ a blue (negative) contribution over the plane perpendicular to the C_2 axis prevails; at $\delta = 120°$ the two slices in Figure 5.17 suggest how all contributions cancel out passing from positive to negative optical rotation.

In summary, as far as we can see from this simple example, the specific rotation density provided by the CDT evaluated by the CTOCD-DZ approach is a function characterized

by high intensity peaks of opposite sign in the proximity of atoms, whose symmetry is clearly connected with the integrated property. It enables us to understand more precisely how the absence of symmetry planes gives rise to optical rotation.

Nonetheless, it remains to be understood how the dominant sign of optical rotation density is connected with the molecular configuration, which implies that further investigations are needed in this regard.

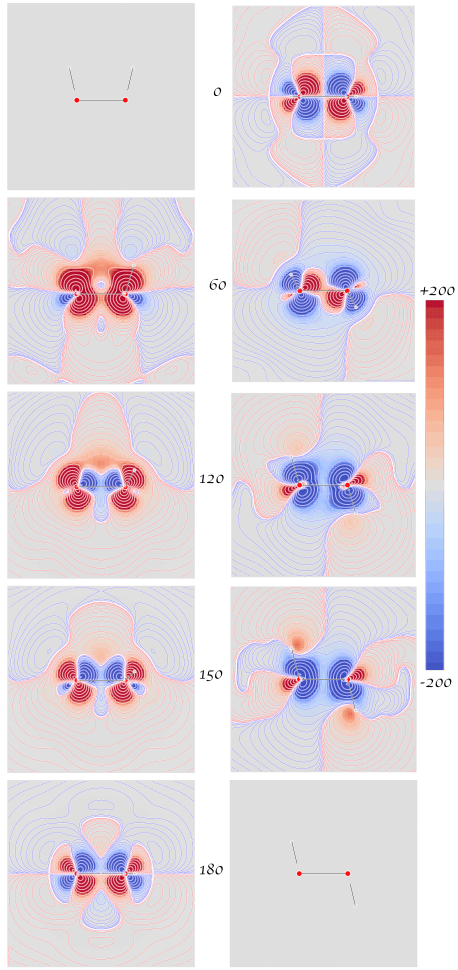

Figure 5.17: Origin-independent CTOCD-DZ MEMDP densities calculated at 355 nm using TDHF theory adopting a fairly large basis set consisting of the uncontracted d-aug-cc-pVQZ on hydrogen atoms and d-aug-cc-pVTZ on oxygen atoms, displayed for five different values of the H_2O_2 dihedral angle. On the left, the plotting plane contains the main symmetry axis; on the right, the plane is perpendicular to the C_2 symmetry axis. Each plotting area is a square centered in the O–O bond midpoint, with a side of 10 a_0. Side bar values are in deg $[\text{dm g/cm}^3]^{-1} a_0^{-3}$.

5.2.2 Stagnation Graphs of LiH

For the LiH molecule, chosen in a first attempt to implement the theory presented in section 4.4, we have adopted a system of coordinates with origin in the center of nuclear charges. The Li-H bond lies in the z Cartesian direction, coinciding with the $C_{\infty v}$ symmetry axis; lithium (hydrogen) has positive (negative) z-coordinate.

To investigate the effects of optical magnetic fields, associated to monochromatic waves with different ω frequency on the $\boldsymbol{J}^{\boldsymbol{B}}(\boldsymbol{r},\omega)$ vector field, we have chosen the corresponding stagnation graphs, which yield nearly complete information in a compact and portable way. SGs superimposed to streamline maps showing heteroclinic orbits that join the equilibrium points, thus defining the topological structure of $\boldsymbol{J}^{\boldsymbol{B}}(\boldsymbol{r},\omega)$, have been calculated for nine ω-frequency values of the magnetic field $\boldsymbol{B} \equiv B_x(\omega)\boldsymbol{\epsilon}_1$ oscillating at right angles to the z-axis, see Figure 5.20.

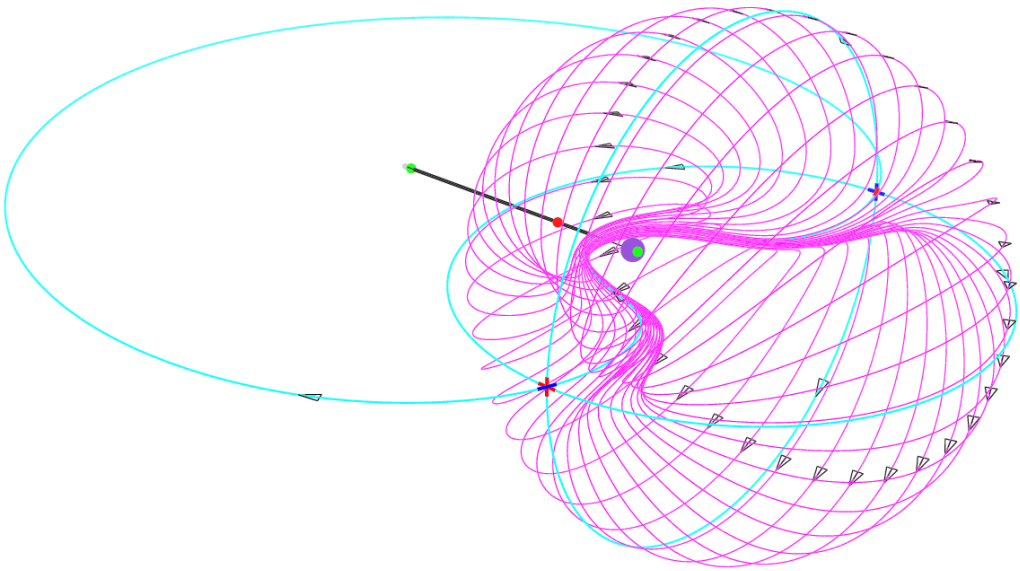

Figure 5.18: Toroidal current density induced in the lithium hydride molecule by a static magnetic field $B_x\boldsymbol{\epsilon}_1$ perpendicular to the bond, directed along the vertical direction of the figure. The $(3,\pm1)$ saddle-nodes are represented by three branched crosses: two red branches on the forefront denote a sink (3,$-$1) saddle-node, with index $\iota = +1$, lying on a manifold tangent to the surface of a topological torus T^2, with Euler characteristic $\chi = 0$. In the background, the conjugated (3,+1) source, with index $\iota = -1$, is indicated by a blue cross on the tangent plane. The (3,$\pm$1) SPs are joined by a heteroclinic streamline corresponding to a one-dimensional hollow region of the toroidal flow. The Poincaré-Hopf theorem[122, 123] is satisfied in the form $+1\ -1 = 0$, using the indices reported in the literature.[78, 124]

The first panel **a** corresponds to the frequency of sodium D-line. The asymptotic orbits reported in Figure 5.20 can be compared with those of Figure 5.18 for static magnetic field, and others previously reported,[67, 72] to visualize qualitative modifications of molecular response induced by a frequency-dependent perturbation.

The current density vector field and its SG are characterized by the magnetic symmetry group of the molecule, obtained by the Tavger-Zaitsev method,[64] i.e.,

$$C_{2v}(C_s) \equiv \{E\, RC_2(z)\, R\sigma_v(xz)\, \sigma_v(yz)\} \equiv \underline{2m}m, \tag{5.39}$$

denoting by R the time-reversal operator and using either the Schönflies or the international notation. Accordingly, the $\sigma_v(yz)$ plane cannot be crossed by the flow, and the $R\sigma_v(xz)$ is traversed only by streamlines orthogonal to it.[101]

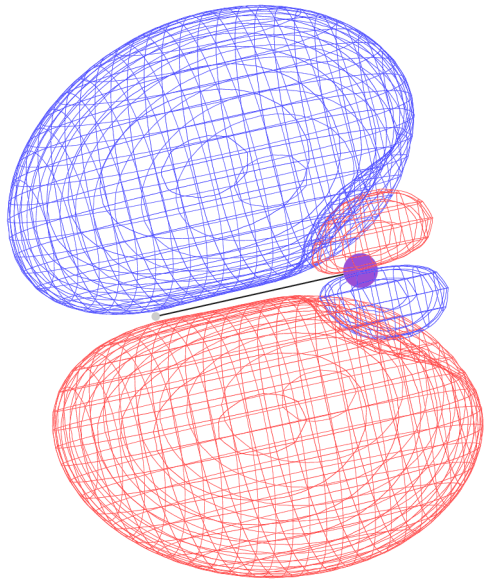

Figure 5.19: The $\varrho^{\dot{B}_x}$ density induced by the time derivative of the magnetic field of a monochromatic wave oscillating with $\omega = 0.125$ a.u. It vanishes identically all over the $R\sigma_v(xz)$ plane for symmetry reasons.

The disconnected SGs of LiH, in the presence of magnetic field perpendicular to the bond axis, for all the ω values examined in this study, are constituted by two (or three, see panels **c**-**i**) connected subgraphs. Five basic features characterize their topology:

- (i) the presence, in the vicinity of the H nucleus, of a green SL, nearly parallel to $\boldsymbol{B} \equiv B_x(\omega)\boldsymbol{\epsilon}_1$, going from and up to the boundaries of the configuration space. It indicates the primary (referred to as "matrix" by Gomes[66]) diatropic vortex, which consists of a continuous pattern of juxtaposed current loops, approximately parallel to one another;
- (ii) a closed SL, forming a ring of (2,0) SPs, with a pair of green and red segments.[125] Such a stagnation loop implies the presence of vortical currents winding on the surface of a topological torus;
- (iii) a pair of conjugated $(3, \pm 1)$ saddle-nodes, denoted by crosses, which play a pivotal role for understanding the connected subgraph of toroidal currents;
- (iv) the primary vortical SL and all the stagnation loops lie entirely on the $R\sigma_v(xz)$ symmetry plane;

- (v) on increasing the value of ω a compression of the toroidal surface is observed in panels **a** through **i** of Figure 5.20. The decrease of volume is accompanied by the onset of vortex- and saddle-flow, documented by connected subgraphs on the right of **c**-**i**, starting and decaying at (0,0) singularities.

An important result, consistent with point (iv), is that the continuity equation (4.51) is exactly satisfied on the xz plane, for symmetry reasons, in the form $0 + 0 = 0$ when the magnetic field oscillates in the x direction. In fact, as shown in Figure 5.19, the $\varrho^{\dot{B}_x}(\boldsymbol{r}, \omega)$ vector vanishes all over the $R\sigma_v(xz)$ plane, which can only be crossed by perpendicular streamlines of $J_y^{B_x}(\boldsymbol{r}, \omega)$, with $\nabla_y J_y^{B_x}(\boldsymbol{r}, \omega) = 0$. Thus

$$\varrho^{\dot{B}_x}(\boldsymbol{r}, \omega) = 0 \quad J_x^{B_x}(\boldsymbol{r}, \omega) = J_z^{B_x}(\boldsymbol{r}, \omega) = 0 \quad \nabla_\alpha \mathcal{J}_\alpha^{B_x}(\boldsymbol{r}, \omega) B_x = \nabla_\alpha J_\alpha^{B_x}(\boldsymbol{r}, \omega) = 0 \tag{5.40}$$

for each $\boldsymbol{r}$ on this plane. Let us now consider a topological sphere, i.e., an S^2 surface with Euler characteristic $\chi = 2$, enclosing the molecule, the stagnation loops observed in panels **a**-**i** and all the asymptotic orbits connecting the $(3, \pm 1)$ SPs. At its intersections with the connected part of the SG which consists of the primary stagnation line passing close to the H nucleus, the electron flow can be represented on a tangent plane, i.e., a smooth Euclidean manifold, by a diatropic vortex with Poincaré index $\iota = +1$. Thus, the Poincaré-Hopf theorem[122, 123] is satisfied in the form $+1 + 1 = 2$ on S^2. A second connected part of the SG contains the stagnation loop represented in red and green[125] in Figure 5.20, which also displays a pair of conjugated $(3, \pm 1)$ saddle-nodes. Six orbits enter or leave the $(3, \pm 1)$ SPs saddle-nodes in the directions specified by an arrow. On the $\sigma_v(yz)$ plane, which contains these points, the continuity equation (4.51) is *not* satisfied by symmetry, but it would be fulfilled in the case of complete basis set. At right angles to the $\sigma_v(yz)$ plane, two heteroclinic trajectories, lying on an xy plane, leave the source $(3, +1)$ and arrive at the sink $(3, -1)$ singular point. An asymptotic wavy line on $\sigma_v(yz)$ flows across the stagnation loop, through its center, thus defining the central "axis" of the toroidal currents, four of which are shown above and below the yz plane in panel **b**. Another pair of vortices is displayed on either side of the separation between green and red SLs in **a**. The two heteroclinic orbits which lie on the yz plane, leaving and entering the $(3, \pm 1)$ saddle-nodes, enclose the vortical diatropic axis and the stagnation loop, respectively. This pattern is analogous to that observed in Figure 5.18 for a static $\boldsymbol{B}$: also for optical magnetic fields, the Poincaré-Hopf theorem[122, 123] is satisfied in the form $+1 \; -1 = 0$, i.e., the Euler characteristic of a torus T^2.

Thus, the set of six asymptotic lines joining the $(3, \pm 1)$ saddle-nodes constitutes a peculiar structure of all the panels displayed in Figure 5.20, playing a major role for the rationalization of the current density vector field of LiH.

A secondary, connected stagnation subgraph, observable for ω=0.116 a.u., in the inset **c** of Figure 5.20, is formed by one green and one blue SLs. An analogous loop is observed in panels **d** and **e**. The latter shows further splitting of the green vortex line, giving rise to a blue segment which indicates intermediate saddle-flow. These loops account for a pattern not considered by Gomes,[66] which may be referred to as a "vacuum fluctuation", since it indicates the ability of a current density vector field of giving rise *ex nihilo* to (0,0) singular points in regions where they are not observed in analogous situations, e.g., for static fields and lower frequencies. Remarkably, the fluctuations displayed in panels **h** and **i** are characterized by saddle- and paratropic flow, denoted by blue and red SLs, respectively.

However, since these subgraphs lie on the $R\sigma_v(xz)$ plane, where the identities (5.40) are fulfilled for symmetry reasons, the index conservation theorem[121][**11**] is evidently

valid. In fact, the creation of a vortical axis is accompanied by that of a saddle line. For instance, in panel **c**, they take place at a (0,0) singular point with coordinates $x = 0.267, z = 2.394$ bohr, in the proximity of which the Poincaré indices +1 of a vortex is canceled by −1 of an associated saddle. In other words, the transition from two imaginary to two real eigenvalues with opposite sign of the Jacobian matrix necessarily comes about via three null eigenvalues of the Jacobian matrix. Another (0,0) point, symmetrically placed at $x = -0.267, z = 2.394$ bohr, defines the end of the vacuum fluctuation.

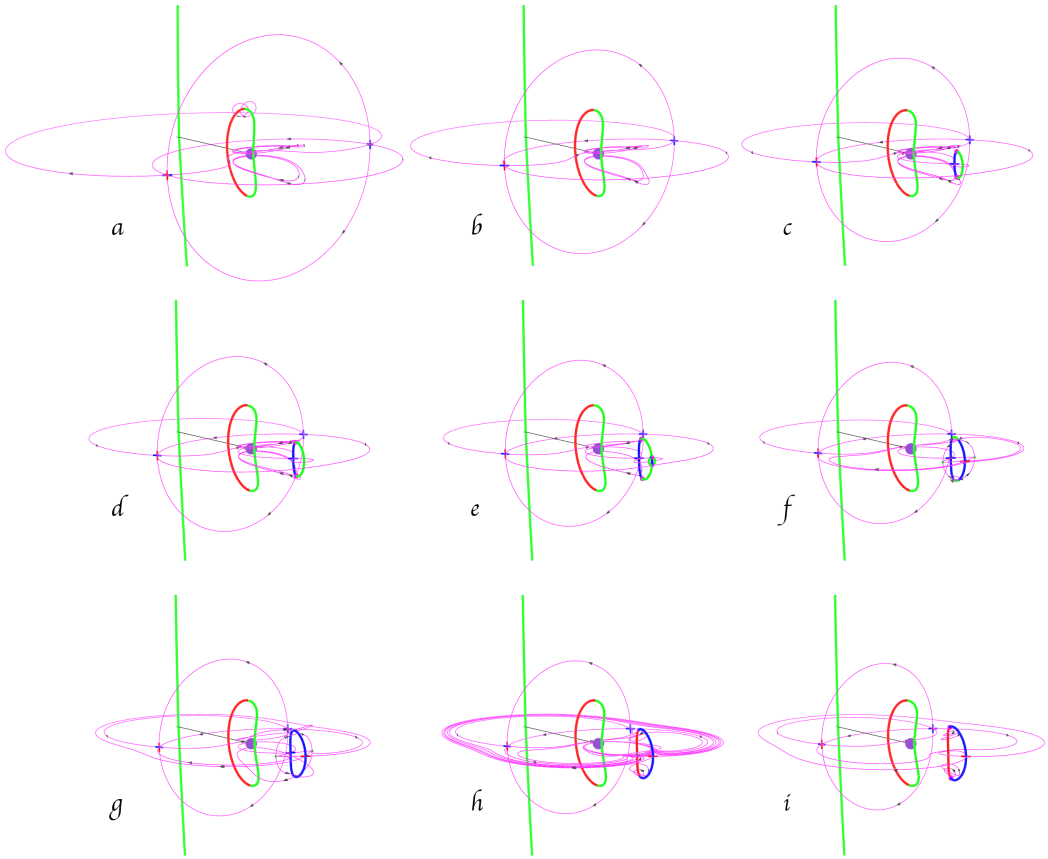

Figure 5.20: Stagnation graphs of the current density vector induced in the electron cloud of the lithium hydride molecule by a magnetic field $B_x(\omega)\boldsymbol{\epsilon}_1$ perpendicular to the bond axis, oscillating at nine increasing frequencies in the transparent region: **a**) 0.07732, **b**) 0.110, **c**) 0.116, **d**) 0.118, **e**) 0.120, **f**) 0.121, **g**) 0.122, **h**) 0.123 and **i**) 0.125 a.u.. Blue color indicates saddle SLs formed by (2,0) points; red/green color designates (2,0) points of paratropic/diatropic vortical SLs. (3,±1) SPs are marked by a cross, indicating the direction of streamlines which enter (leave) the singularity in red (blue) on the tangent plane.

Summarizing, the present work provides convincing evidence that theoretical procedures based on continuous translation of the origin of the electronic current density, induced in a chemical species by frequency-dependent magnetic fields, can be easily and effectively coded in a computer program. The $\boldsymbol{J}^{\boldsymbol{B}}(\boldsymbol{r}, \omega)$ based on such a computational scheme

yields reliable visualizations of vector fields that meet the requirement of origin independence all over the electron charge distribution. The preliminary investigation outlined in this study,[121][**11**] which, to the best of our knowledge, is the first ever reported, may stimulate future research in this field. Although limited to a small compound, the LiH molecule, it revealed quite useful to analyze a series of questions, concerning mathematical and physical aspects. For instance, the information arrived at on topological features, e.g., the distribution of singular points of different types, is expected to be immediately transferable to larger compounds.

A number of characteristics so far not observed for time-independent $\boldsymbol{B}$ appear in $\boldsymbol{J}^{\boldsymbol{B}}(\boldsymbol{r})$ for a molecule in the presence of optical magnetic field, marking differences that may be quite relevant between static and dynamic case. They are nicely described via a disconnected stagnation graph, usually containing connected subgraphs constituted by stagnation lines and isolated singularities. In the case of the LiH molecule, two noticeable phenomena have been detected:

- (i) a contraction of the toroidal surface surrounding the Li nucleus, a typical signature of its $\boldsymbol{J}^{\boldsymbol{B}}(\boldsymbol{r},\omega)$ field, is observed on increasing the ω frequency of the impinging radiation. This reduction of volume is accompanied by shrinkage of the asymptotic orbits which connect $(3,\pm1)$ singularities defining source and sink of the torus.

- (ii) The decrease in size of toroidal flow takes place together with a sudden outbreak of connected subgraphs, i.e., stagnation loops formed by vortex- and saddle-lines, beginning and ending at two (0,0) singularities, critical points at which three eigenvalues of the Jacobian matrix vanish. Since the Poincaré indices of vortex and saddle SLs have opposite (±1) sign, their sum must identically vanish where the fluctuation starts and decays to fulfil the Gomes theorem. The loops of saddle- and vortex-lines, either diatropic or paratropic, start appearing at certain values of ω in regions of the electron cloud where they could not be observed for smaller frequencies. Accordingly, they have been referred to as "vacuum fluctuations", since they suddenly materialize in the vector field. Branchings of this kind have not been predicted by Gomes.[66]

All the calculations, shown in this subsection, have been carried out using the BHandHLYP functional,[126] recently shown to provide reliable linear response properties,[58][**5**] employing basis sets of contracted functions which include terms of high angular momentum, taken from Basis Set Exchange (BSE).[110] In particular, the aug-pcSseg-4 basis set[127] has been adopted for this molecule. BHandHLYP transition matrix elements $\left\langle j \left| (\boldsymbol{r}\times\boldsymbol{\nabla})_\beta \right| a \right\rangle$, $\langle j\,|\nabla_\delta|\,a\rangle$, amplitudes $\boldsymbol{T}_j$ and energies ω_{ja} have been computed by the Gaussian 16 program package,[56] using the TD=(full,sos) 6d 10f keywords. The molecular geometry has been optimized using the same functional and basis set. CTOCD-DZ time-dependent CDT components have been evaluated using the SYSMOIC program package.[14][**3**] Stagnation graphs have been computed at $t=0$.

5.3 Origin Independent Polarizability Densities and Toroidisabilities

The aim of this section is to discuss how the implementation of an origin-independent polarizability density can be achieved, starting from the definition of the current density tensor $\mathcal{J}_\alpha^{\dot{E}_\beta}$, given in section 4.5. Using a notation similar to the one adopted before we have that equation (4.43) can be rewritten as

$$\begin{aligned}\mathcal{J}_\alpha^{\dot{E}_\beta}(\boldsymbol{r},\omega) =& \frac{ne^2}{m_\mathrm{e}}\Im\Big\{\int \Psi_a^{(R_\beta)_0 *}(\boldsymbol{r},\boldsymbol{X}_1,\omega)\hat{p}_\alpha\Psi_a^{(0)}(\boldsymbol{r},\boldsymbol{X}_1)d\boldsymbol{X}_1 \\ &- \int \Psi_a^{(0)*}(\boldsymbol{r},\boldsymbol{X}_1)\hat{p}_\alpha\Psi_a^{(R_\beta)_0}(\boldsymbol{r},\boldsymbol{X}_1,\omega)d\boldsymbol{X}_1\Big\} \end{aligned} \tag{5.41}$$

or if we use off-diagonal hypervirial relationships

$$\begin{aligned}\mathcal{J}_\alpha^{\dot{E}_\beta}(\boldsymbol{r},\omega) &= \frac{ne^2}{m_\mathrm{e}^2}\Re\Big\{-\int \Psi_j^{(P_\beta)_{-1}*}(\boldsymbol{r},\boldsymbol{X}_1,\omega)\,\hat{p}_\alpha\Psi_a^{(0)}(\boldsymbol{r},\boldsymbol{X}_1)\,d\boldsymbol{X}_1 \\ &\quad + \int \Psi_a^{(0)*}(\boldsymbol{r},\boldsymbol{X}_1)\,\hat{p}_\alpha\Psi_j^{(P_\beta)_{-1}}(\boldsymbol{r},\boldsymbol{X}_1,\omega)\,d\boldsymbol{X}_1\Big\} \end{aligned} \tag{5.42}$$

where

$$\Psi_a^{(R_\beta)_0}(\boldsymbol{r},\boldsymbol{X}_1,\omega) = \frac{1}{\hbar}\sum_{j\neq a}\frac{\left\langle j|\hat{R}_\beta|a\right\rangle}{\omega_{ja}^2-\omega^2}\Psi_j^{(0)}(\boldsymbol{r},\boldsymbol{X}_1) \tag{5.43}$$

$$\Psi_a^{(P_\beta)_{-1}}(\boldsymbol{r},\boldsymbol{X}_1,\omega) = \frac{1}{\hbar}\sum_{j\neq a}\frac{\left\langle j|\hat{P}_\beta|a\right\rangle}{\omega_{ja}(\omega_{ja}^2-\omega^2)}\Psi_j^{(0)}(\boldsymbol{r},\boldsymbol{X}_1) \tag{5.44}$$

can be regarded as vectors explicitly dependent on the radiation frequency ω. Allowing for definitions of total electronic angular momentum operator, introduced before, the vector function (5.44) becomes

$$\Psi_a^{(P_\beta)_{-1}}(\boldsymbol{r},\boldsymbol{X}_1,\omega) = -\mathrm{i}\hbar\Psi_a^{(\nabla_\beta)_{-1}}(\boldsymbol{r},\boldsymbol{X}_1,\omega) \tag{5.45}$$

where

$$\Psi_a^{(\nabla_\beta)_{-1}}(\boldsymbol{r},\boldsymbol{X}_1,\omega) = \sum_{j\neq a}\frac{1}{\omega_{ja}(\omega_{ja}^2-\omega^2)}\left\langle j\left|\sum_k(\nabla_\beta)_k\right|a\right\rangle\Psi_j^{(0)}(\boldsymbol{r},\boldsymbol{X}_1) \tag{5.46}$$

For an unrestricted open-shell system, represented by a one-determinant wavefunction

$$\Psi = \frac{1}{\sqrt{n!}}\det\left[\psi_1^\alpha,\psi_2^\beta,\cdots\right] \tag{5.47}$$

constructed by $n = n_\alpha + n_\beta$ occupied molecular orbitals, the previous equations become, in atomic units, respectively

$$\mathcal{J}_\alpha^{\dot{E}_\beta}(\boldsymbol{r},\omega) = \sum_j^n\left[-\psi_j^{(R_\beta)_0}(\boldsymbol{r},\omega)\nabla_\alpha\psi_j^{(0)}(\boldsymbol{r}) + \psi_j^{(0)}(\boldsymbol{r})\nabla_\alpha\psi_j^{(R_\beta)_0}(\boldsymbol{r},\omega)\right] \tag{5.48}$$

$$\mathcal{J}_{\alpha}^{\dot{E}_{\beta}}(\boldsymbol{r},\omega) = -\sum_{j}^{n}\left[\psi_{j}^{(\nabla_{\beta})^{-1}}(\boldsymbol{r},\omega)\nabla_{\alpha}\psi_{j}^{(0)}(\boldsymbol{r}) - \psi_{j}^{(0)}(\boldsymbol{r})\nabla_{\alpha}\psi_{j}^{(\nabla_{\beta})^{-1}}(\boldsymbol{r},\omega)\right] \tag{5.49}$$

Then, spin-orbitals ψ_j are expanded as linear combinations of basis functions χ_q

$$\psi_{j}^{(0)}(\boldsymbol{r}) = \sum_{q} C_{qj}^{(0)}\chi_{q}(\boldsymbol{r}) \tag{5.50}$$

$$\psi_{j}^{(R_{\beta})_0}(\boldsymbol{r},\omega) = \sum_{q} C_{qj}^{(R_{\beta})_0}(\omega)\chi_{q}(\boldsymbol{r}) \tag{5.51}$$

$$\psi_{j}^{(\nabla_{\beta})^{-1}}(\boldsymbol{r},\omega) = \sum_{q} C_{qj}^{(\nabla_{\beta})^{-1}}(\omega)\chi_{q}(\boldsymbol{r}) \tag{5.52}$$

where $C_{qj}^{(0)}$, $C_{qj}^{(R_{\beta})_0}(\omega)$ and $C_{qj}^{(\nabla_{\beta})^{-1}}(\omega)$ are unperturbed and perturbed coefficients that are different for α and β spin-orbitals that can be obtained using the RPA at the HF or DFT level of theory. To be complete, as done before, we can introduce also the equations rewritten using the density matrices approach

$$\mathcal{J}_{\alpha}^{\dot{E}_{\beta}}(\boldsymbol{r},\omega) = -\sum_{p}\sum_{q} R_{pq}^{(R_{\beta})_0}(\omega)\chi_{q}\nabla_{\alpha}\chi_{p} \tag{5.53}$$

$$\mathcal{J}_{\alpha}^{\dot{E}_{\beta}}(\boldsymbol{r},\omega) = -\sum_{p}\sum_{q} R_{pq}^{(\nabla_{\beta})^{-1}}(\omega)\chi_{q}\nabla_{\alpha}\chi_{p} \tag{5.54}$$

where the anti-symmetric density matrices are defined as

$$R_{pq}^{(R_{\beta})_0}(\omega) = \sum_{j}^{n}\left[C_{pj}^{(0)}C_{qj}^{(R_{\beta})_0} - C_{pj}^{(R_{\beta})_0}C_{qj}^{(0)}\right] \tag{5.55}$$

$$R_{pq}^{(\nabla_{\beta})^{-1}}(\omega) = \sum_{j}^{n}\left[C_{pj}^{(0)}C_{qj}^{(\nabla_{\beta})^{-1}} - C_{pj}^{(\nabla_{\beta})^{-1}}C_{qj}^{(0)}\right] \tag{5.56}$$

The tensor $\mathcal{J}_{\alpha}^{\dot{E}_{\beta}}(\boldsymbol{r},\omega)$ is connected with two physical quantities, depending on whether it is multiplied by $\boldsymbol{E}(\omega,t) = \boldsymbol{E}_0\,\cos(\omega t)$ or $\dot{\boldsymbol{E}}(\omega,t) = -\omega\,\boldsymbol{E}_0\,\sin(\omega t) = \omega\,\boldsymbol{E}_0\,\cos(\omega t + \pi/2)$.

$$\mathcal{M}_{\alpha}(\boldsymbol{r},\omega) \;=\; \mathcal{J}_{\alpha}^{\dot{E}_{\beta}}(\boldsymbol{r},\omega)E_{0\beta}\,\cos(\omega t), \tag{5.57}$$

$$J_{\alpha}^{\dot{\boldsymbol{E}}}(\boldsymbol{r},\omega) \;=\; \omega\,\mathcal{J}_{\alpha}^{\dot{E}_{\beta}}(\boldsymbol{r},\omega)\,E_{0\beta}\,\cos(\omega t + \pi/2) \tag{5.58}$$

These relations define the dipole density vector $\mathcal{M}_{\alpha}(\boldsymbol{r},\omega)$ induced in the molecule and the current density vector $\boldsymbol{J}^{\dot{\boldsymbol{E}}}(\boldsymbol{r},\omega)$, quite important for the interpretation of static and dynamic properties. An interesting feature of $\boldsymbol{J}^{\dot{\boldsymbol{E}}}(\boldsymbol{r},\omega)$ is that can be interpreted as a polarization current because it is generated by an electric field out of phase by $\pi/2$. A detailed description of these applications can be found in Refs.[128][**8**] and [129][**10**].

5.3.1 Origin-Independent Polarizability Density

Three simple model systems have been considered for the calculation of static and dynamic electric dipole polarizability densities at the TDDFT level of approximation. They are H_2O and the linear molecules CO and N_2. Owing to their small size, very accurate computations have been carried out, using the BHandHLYP functional, [126] recently shown to provide good linear response properties, [58][**5**] adopting basis sets of contracted functions which include terms of high angular momentum, taken from the BSE.[110] In particular, on H atom we have chosen the aug-cc-pV5Z basis, that is, a (6s5p4d3f2g) basis set. For C, N, and O atoms we have adopted the aug-cc-pV7Z, which corresponds to a (9s8p7d6f5g4h3i2j) basis set. BHandHLYP transition matrix elements, amplitudes $\boldsymbol{T}_j$ and energies ω_{ja} have been computed by the Gaussian 16 program package,[56] using the TD=(full,sos) 6d 10f keywords. Molecular geometries were optimized at BHandHLYP/aug-cc-pVTZ level. Polarizability densities have been evaluated using the SYSMOIC program package.[14][**3**] Spatial integration of the density functions has been performed using the Becke scheme,[53] adopting 131 angular points for the Lebedev's quadrature of 59th order of accuracy[130] and 131 radial points for the Gauss-Chebyshev radial quadrature of second-kind.[131] Let us first consider the origin independence of the polarizability densities defined by means of $\mathcal{J}_\alpha^{\dot{E}_\beta}(\boldsymbol{r},\omega)$ for the (P,R) and (P,P) formalisms, in comparison with the conventional origin-dependent polarizability density

$$\aleph_{\alpha\beta}(\boldsymbol{r},\omega) = r_\alpha \varrho^{E_\beta}(\boldsymbol{r},\omega) \tag{5.59}$$

in the (R,R) formalism. This is a quite interesting point since translational invariance is a fundamental requirement for any physically meaningful density, *irrespective of basis set choice*. To investigate this aspect, we have calculated the isotropic value of the polarizability densities of the H_2O molecule for two different origins, adopting the rather small 6-31G(d,p) basis set within the TDHF approach. The origin hereafter denoted '000' has been chosen by making it coincide with the center of nuclear charges. The second origin, referred to as '123', has been set shifting the previous one by 1, 2, and 3 bohr along x, y, and z, respectively. Some points of interest are:

1. Densities **b** and **c** would be exactly the same in the limit of complete basis set. In Figure 5.21 some differences can be observed owing to the small size of the basis set adopted;

2. Computed tensor components $\alpha_{\alpha\beta}$ depend on basis set quality. Upon integration, all densities, for both origins, would converge to the same value of dipole polarizability in the complete basis set limit;

3. The density **a** depends on the origin, although the corresponding electric dipole polarizability does not, but improves on increasing basis set quality towards the complete basis set result.

Carbon monoxide is similar to the nitrogen molecule, in that it has the same number of electrons, chemical bonds and lone pairs. To some extent, also their electric response properties, permanent electric dipole moment and electric dipole polarizability, are similar, consider for instance the very small dipole moment of CO, 0.122 D.[132] However, these molecules contain distinct atomic species and different polarizability densities are expected to characterize them, in connection with diverse topology of induced current density fields. To highight this point, in Figures 5.22 and 5.23 we display diverging color maps for the polarizability density tensor components of CO and N_2, respectively,

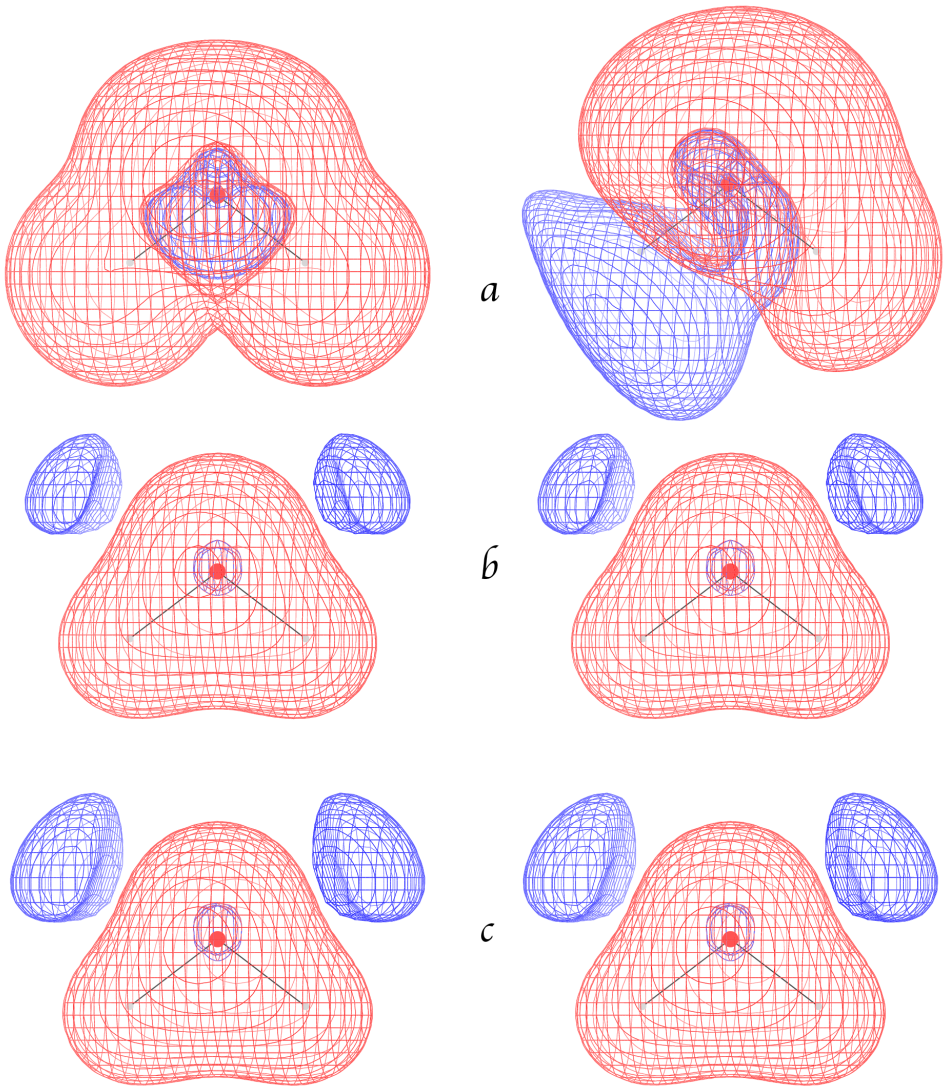

Figure 5.21: Calculated isotropic polarizability densities for the H_2O molecule at TDHF 6-31G(d,p) level of approximation, displayed as iso-value surfaces: red +0.02, blue -5×10^{-4} a_0^3. Densities on the **left**/**right** column are relative to the '000'/'123' origin, see text. Labels **a**, **b**, **c** denote the three different polarizability densities respectively.

calculated for the static case and for two radiation frequencies which bracket - one less and one greater than - the excitation energy associated with the first non-zero transition moment of the corresponding tensor component. For $\omega \neq 0$, we stress that our approach is not valid in the near-resonant region, since the SOS relations used here do not contain any (phenomenological) dumping term representing the finite lifetime of the excited states.[133] Therefore, we have carefully chosen the frequency values to keep the polarizability tensor components below reasonable limits within the transparent region. The captions to Figures 5.22 and 5.23 report $\alpha_{\parallel}$ and $\alpha_{\perp}$ obtained by integrating the polarizability densities displayed. As can be observed, the absolute value of the integrated polarizability components is always less than 75 a.u.

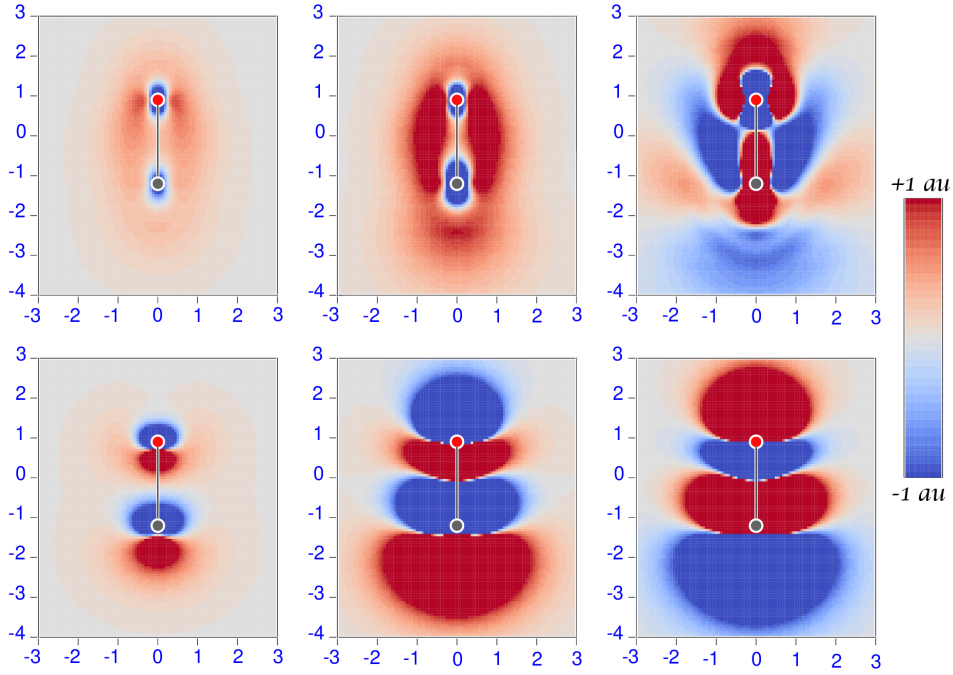

Figure 5.22: Diverging color map of the origin-independent polarizability density functions for the CO molecule. The CPK (Corey-Pauling-Koltun) color scheme colors 'atom' objects by the atom (element) type. The top row shows parallel components calculated by Eq. (5.48) for three radiation frequencies, $\omega = 0.0, 0.393, 0.401$ a.u., from left to right. The polarizability components obtained by spatial integration are $\alpha_{\parallel}^{(R,P)}(0) = 14.67$, $\alpha_{\parallel}^{(R,P)}(0.393) = 44.03$, and $\alpha_{\parallel}^{(R,P)}(0.401) = -18.37$ a.u.. The bottom row shows perpendicular components calculated for three radiation frequencies, $\omega = 0.0, 0.312, 0.325$ a.u., from left to right. The polarizability components obtained by spatial integration are $\alpha_{\perp}^{(R,P)}(0) = 11.59$, $\alpha_{\perp}^{(R,P)}(0.312) = 64.02$, and $\alpha_{\perp}^{(R,P)}(0.325) = -73.71$ a.u.

For the static case, we found that the parallel polarizability densities of CO and N_2 are characterized by similar negative domains of small extension in the vicinity of the nuclei, embedded within a positive region, which in carbon monoxide is more conspicuous about the oxygen nucleus - in the upper end of the CO bond in Figure 5.22 - than carbon's, whilst in N_2 the obviously symmetric positive distribution has a magnitude roughly in-

termediate between that of O and C in Fig. 5.22. Interestingly, the $\alpha_{\parallel}$ components calculated in this study are almost the same for CO (14.67 a.u.) and N_2 (14.56 a.u.), despite the different density distributions.

The perpendicular component of the polarizability density presents pairs of "bubbles" of opposite sign nearby each nucleus, resembling a p orbital oriented along the bond. Notably, the bubble size depends on the nuclear species, being larger about C rather than O in carbon monoxide. In the nitrogen molecule, the bubbles have smaller size and are characterized by N-centered negative cores. In any case, positive (red) regions extend in space much more than negative (blue) ones. Moreover, the bubble pairs are aligned in CO, whereas they are anti-aligned in N_2.

Remarkably, the domains of juxtaposed bubbles with opposite sign tend to offset one another upon integration. Therefore, their contribution to the integrated property almost vanishes. As a consequence, $\alpha_{\perp}(0)$ turns out to be smaller than $\alpha_{\parallel}(0)$, a result that would be difficult to explain without the corresponding maps of polarizability density components shown in Figures. 5.22 and 5.23. Actually, our calculated values are 11.59 and 9.93 a.u. for CO and N_2, respectively, whereas computed $\alpha_{\parallel}(0)$ for these molecules are 14.67 and 14.56 a.u. respectively.

Comparing our results with the coupled-cluster (CCSDT) static polarizability calculated by Hammond et al. [134], we note a general good agreement, with the relevant exception of $\alpha_{\parallel}$ in CO for which a discrepancy as large as 6% is observed. From this point of view, it seems clear that for this component the electronic correlation provides a sizeable contribution, larger in CO than in N_2, as evidenced also by the quite small dipole moment estimated here 4×10^{-4} D, at least with the correct sign.

For the dynamic case, the positive regions of electric dipole polarizability density are observed to increase steadily more than the negative ones, as the radiation frequency increases from zero towards the first transition energy in both molecules, see for example the central panel of Figures 5.22 and 5.23. This is consistent with the expected enhancement of the polarizability tensor components. Since the first transition energy for the perpendicular matrix element $\left\langle j \left| \hat{R}_{\perp} \right| a \right\rangle$ is less than the first transition energy for the parallel matrix element $\left\langle j \left| \hat{R}_{\parallel} \right| a \right\rangle$ in both molecule, $\alpha_{\perp}(\omega)$ becomes larger than $\alpha_{\parallel}(\omega)$ as the radiation frequency ω approaches the first transition pole, as also noted in Ref.[134].

The situation changes drastically when the components turn negative whenever ω goes beyond a resonant frequency. Interestingly, with the exception of the perpendicular polarizability density in CO, the density functions do not just change their sign, but undergo also a significant modification of size, as well as distortion of their shape.

Summarizing, we have shown how is possible to define a pure theoretical origin-independent polarizability density that can be used to explain better the charge polarization mechanism, to our knowledge this has not been done before. This density function manifests a behavior that changes inside the molecular domain due to an electron counter-polarization effect observed only if the considered system has at least p-type electrons. As found practically, in He atom and H_2 molecule we have only red regions. This picture is confirmed also at the Full-CI level of theory.

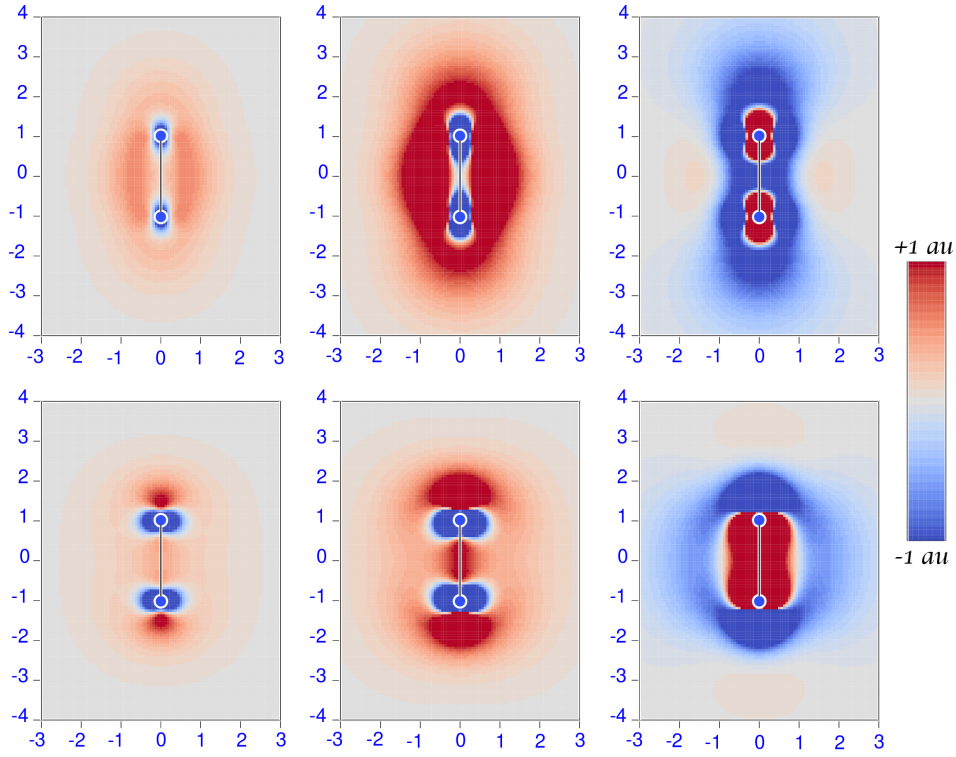

Figure 5.23: Diverging color map of the origin-independent polarizability density functions for the N_2 molecule. The top row displays parallel components calculated by Eq. (5.48) for three radiation frequencies, $\omega = 0.0, 0.465, 0.486$ a.u., from left to right. The polarizability components obtained by spatial integration are $\alpha_{\parallel}^{(R,P)}(0) = 14.56$, $\alpha_{\parallel}^{(R,P)}(0.465) = 71.89$, and $\alpha_{\parallel}^{(R,P)}(0.486) = -40.92$ a.u. The bottom row displays perpendicular components computed for three radiation frequencies, $\omega = 0.0, 0.450, 0.478$ a.u., from left to right. The polarizability components obtained by spatial integration are $\alpha_{\perp}^{(R,P)}(0) = 9.93$, $\alpha_{\perp}^{(R,P)}(0.450) = 29.20$, and $\alpha_{\perp}^{(R,P)}(0.478) = -16.40$ a.u.

5.3.2 Dynamic Toroidizability in Optical Electric Fields

The existence of red and blue regions in maps of the polarizability density function, shown in the previous subsection, implies that the vectorial field $\boldsymbol{J}^{\dot{\boldsymbol{E}}}(\boldsymbol{r},\omega)$ associated with the tensor $\mathcal{J}_{\alpha}^{\dot{E}_\beta}$ is characterized by a toroidal structure. This particular shape is a universal feature of closed-shell atoms and molecules in the presence of a time-dependent electric field.

A toroidal moment together with an induced electric dipole moment generates a particular configuration termed an *electric anapole*. The aim of this subsection is to show some plots of the current density vector field $\boldsymbol{J}^{\dot{\boldsymbol{E}}}$ in atoms and molecules.

Very accurate computations have been carried out using the BHandHLYP functional, [126] recently shown to provide good linear response properties.[58][**5**] Large basis sets, which include high angular momentum functions, taken from BSE,[110] have been adopted. Three different basis sets have been considered, that are, aug-cc-pV5Z-RIFIT for Ne, Ar, Kr and BeH_2; aug-cc-pV7Z for CO and N_2; aug-cc-pVQZ for benzene. The Gaussian 16 program package [56] has been used to compute transition matrix elements of operators $\hat{\boldsymbol{R}}$ and $\hat{\boldsymbol{P}}$ and to optimize geometries at BHandHLYP/aug-cc-pVTZ level. The SYSMOIC program package [14][**3**] has been employed to compute maps and trajectories of the current density $\boldsymbol{J}^{\dot{\boldsymbol{E}}}$ and to evaluate the spatial integrals of polarisability and mixed anapole-electric dipole polarisability densities, using the Becke scheme,[53] adopting 131 angular points for Lebedev's quadrature of 59th order of accuracy[130] and 131 radial points for the Gauss-Chebyshev radial quadrature of second-kind.[131]

The theoretical results arrived at in the present subsection demonstrate that the electronic cloud of diamagnetic atoms and molecules, i.e., closed shell systems containing an even number of electrons, is characterized by a peculiar and pervasive propensity to dynamic toroidization, which can be induced by the oscillating electric field of a beam of monochromatic light. Such a phenomenology is determined by the time derivative of the associated electric field, giving rise to an electronic current density vector field, and inducing at the same time an electric dipole polarizability density conveniently described by a second-rank tensor field.

Therefore, atoms and molecules exhibit induced anapolar response resulting from superposition of toroidal and electric dipole moments in the transparent region. At any rate, the induction of toroidization is governed by a second-rank tensor, the anapole polarizability $f'_{\alpha\beta}$ defined by

$$\begin{aligned} f'_{\alpha\beta} &= -\frac{1}{\hbar}\sum_{j\neq a}\frac{2\omega}{\omega_{ja}^2-\omega^2}\Im\left\{\langle a\left|\hat{a}_\alpha\right|j\rangle\left\langle j\left|\hat{\mu}_\beta\right|a\right\rangle\right\} \\ &= -\frac{1}{6}\,\omega\int\left(r^2\delta_{\alpha\gamma}-r_\alpha r_\gamma\right)\mathcal{J}_\gamma^{\dot{E}_\beta}d^3r \end{aligned} \tag{5.60}$$

with

$$\hat{\boldsymbol{a}} = \frac{e}{6m_{\mathrm{e}}}\sum_{k=1}^{n}\left[r^2\hat{\boldsymbol{p}}-\boldsymbol{r}\left(\boldsymbol{r}\cdot\hat{\boldsymbol{p}}\right)+\mathrm{i}\hbar\boldsymbol{r}\right]_k \tag{5.61}$$

the electronic anapole operator. Its expectation value is quite weak and hardly measurable, according to computed estimates reported in Table 5.5.[88, 135][**4**] The toroidal contributions are small and difficult to detect in materials that exist in nature.[136] However they are possibly enhanced for ω approaching an absorption frequency.

The discovery of a resonant toroidal response in metamaterials has driven the methodical study of toroidal electrodynamics. Therefore, further investigations are needed to understand the behavior of chemical probes in near-resonance spectral regions. Nonetheless, despite the recent flood of experimental and theoretical works, the field is still in its infancy, with a number of problems to be solved and practical applications to delve into. Toroidal resonances in chemical systems like those studied here remain to be observed and the spectroscopy of toroidal resonances to be developed. Thus systematic investigations must be taken up in earnest by physicists and chemists.

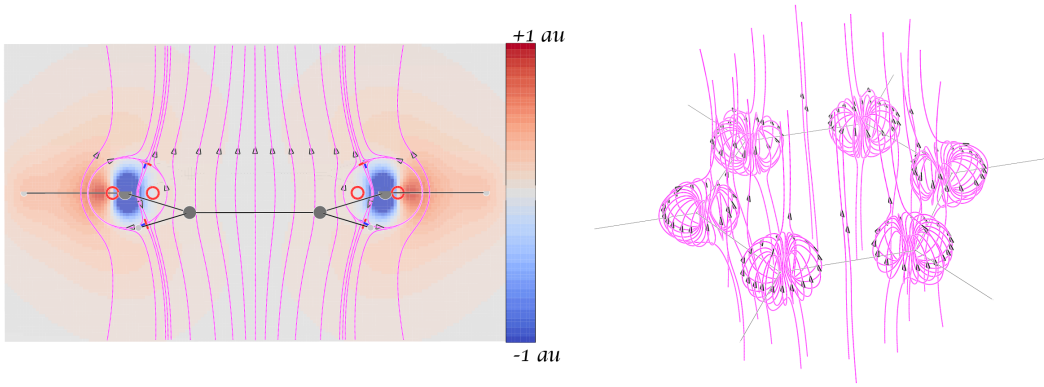

Figure 5.24: Anapole moments of benzene induced by the time derivative $\dot{\boldsymbol{E}}$ of monochromatic light with wavelength λ=589.3 nm, corresponding to sodium D line. The map on the left shows a section of the $\boldsymbol{J}^{\dot{\boldsymbol{E}}}$ vector field induced by a uniform electric field orthogonal to the $T\sigma_h$ plane, by placing a set of streamlines lying on a σ_d plane onto the electric dipole polarisability density. Heteroclinic trajectories about two opposite C atoms connect pairs of conjugated saddle-nodes, i.e., critical $(3, \pm 1)$ stagnation points corresponding to source and sink of poloidal flow that generates six toroidal moments, one for each carbon atom, shown on the right.

Table 5.5: Toroidal and electric dipole polarisabilities of the considered systems.[†]

Molecule	$f'_{\parallel}$	$f'_{\perp}$	$\alpha_{\parallel}^{(R,P)}$	$\alpha_{\perp}^{(R,P)}$	$\alpha_{\parallel}^{(R,R)}$	$\alpha_{\perp}^{(R,R)}$
Ne	−0.0267	−0.0267	2.58	2.58	2.54	2.54
Ar	−0.3129	−0.3129	11.22	11.22	11.15	11.15
Kr	−0.5527	−0.5527	17.13	17.13	17.14	17.14
CO	−0.3443	−0.7994	14.9391	11.8749	14.9394	11.8751
N_2	−0.3099	−0.4700	14.7997	10.0691	14.7999	10.0691
BeH_2	−0.7722	−1.8998	20.61	20.33	20.63	20.35
C_6H_6	−7.1495	−6.5442	45.02	82.13	44.95	82.13

[†] From CODATA recommended values of physical constants,[137] the conversion factors from a.u. to SI units are,
for $f'_{\alpha\beta}$: $e^2a_0^4/\hbar \;\; = 1.908\,750\,473 \times 10^{-45}\,\mathrm{F\,m^4 s^{-1}}$,
for $\alpha_{\alpha\beta}$: $e^2a_0^2/E_\mathrm{h} = 1.648\,777\,273 \times 10^{-41}\,\mathrm{F\,m^2}$.
The SI units for toroidal moment are $\mathrm{Am^3}$.

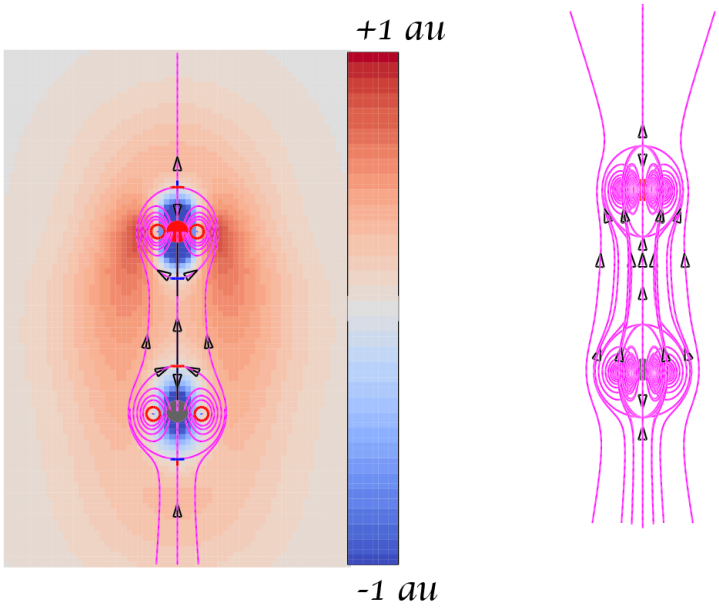

Figure 5.25: Anapole moment of CO induced by the time derivative $\dot{\boldsymbol{E}}$ of monochromatic light with wavelength λ=589.3 nm, corresponding to sodium D line. The map on the left shows a section of the $\boldsymbol{J}^{\dot{\boldsymbol{E}}}$ vector field induced by the electric field $E_z\boldsymbol{\epsilon}_3$ parallel to the bond, by placing a set of streamlines onto the electric dipole polarisability density. Heteroclinic trajectories connect two pairs of conjugated saddle-nodes, i.e., $(3, \pm 1)$ stagnation points corresponding to source (blue) and sink (red) of flow that generates toroidal moments along the central symmetry axis of toroidal surfaces represented on the right.

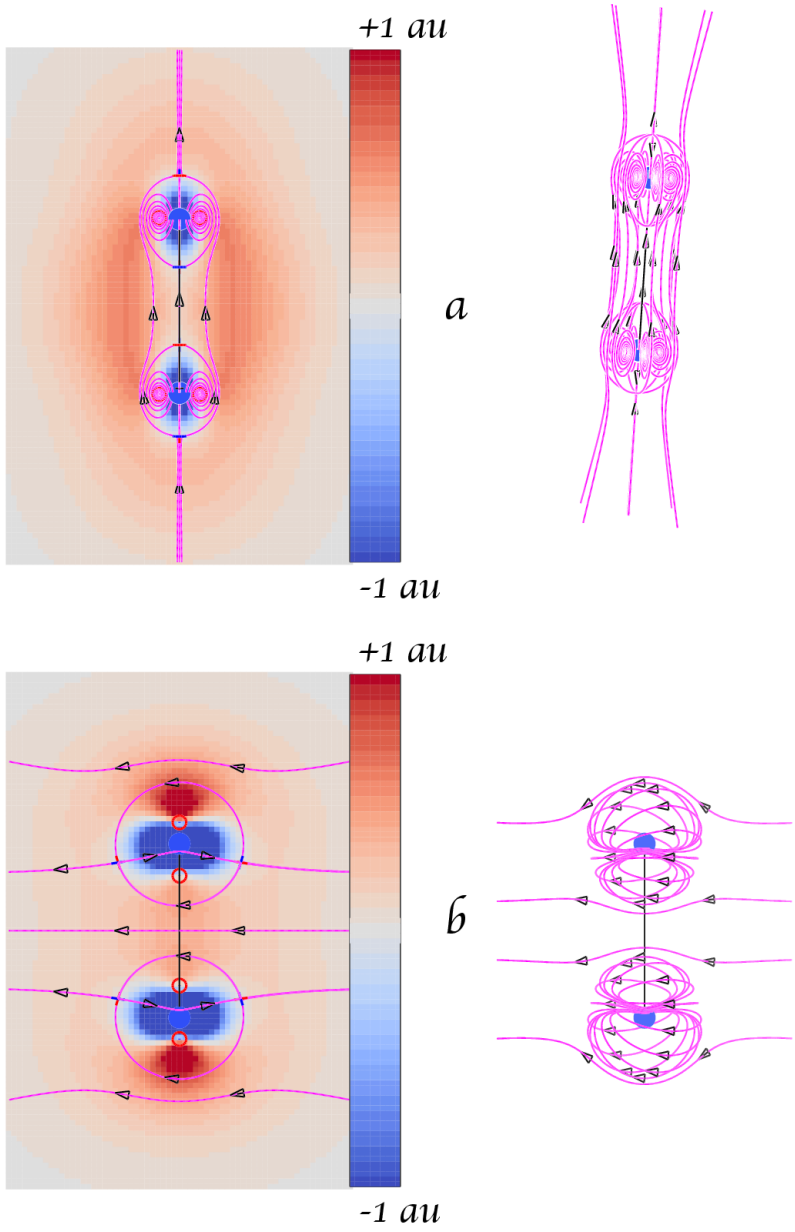

Figure 5.26: Anapole moments of N_2 induced by the time derivative $\dot{\boldsymbol{E}}$ of monochromatic light with wavelength λ=589.3 nm, corresponding to sodium D line. The maps on the left show a section of the $\boldsymbol{J}^{\dot{\boldsymbol{E}}}$ vector field, by placing a set of streamlines onto the electric dipole polarisability density. Heteroclinic trajectories connect two conjugated saddle-nodes, i.e., $(3, \pm 1)$ stagnation points corresponding to source and sink of poloidal flow that generates a toroidal moment along the central symmetry axis of toroidal surfaces displayed on the right. On the left of panel **a** (**b**) the electric field $E_z\boldsymbol{\epsilon}_3$ is parallel ($E_x\boldsymbol{\epsilon}_1$, directed from right to left, is orthogonal) to the bond direction.

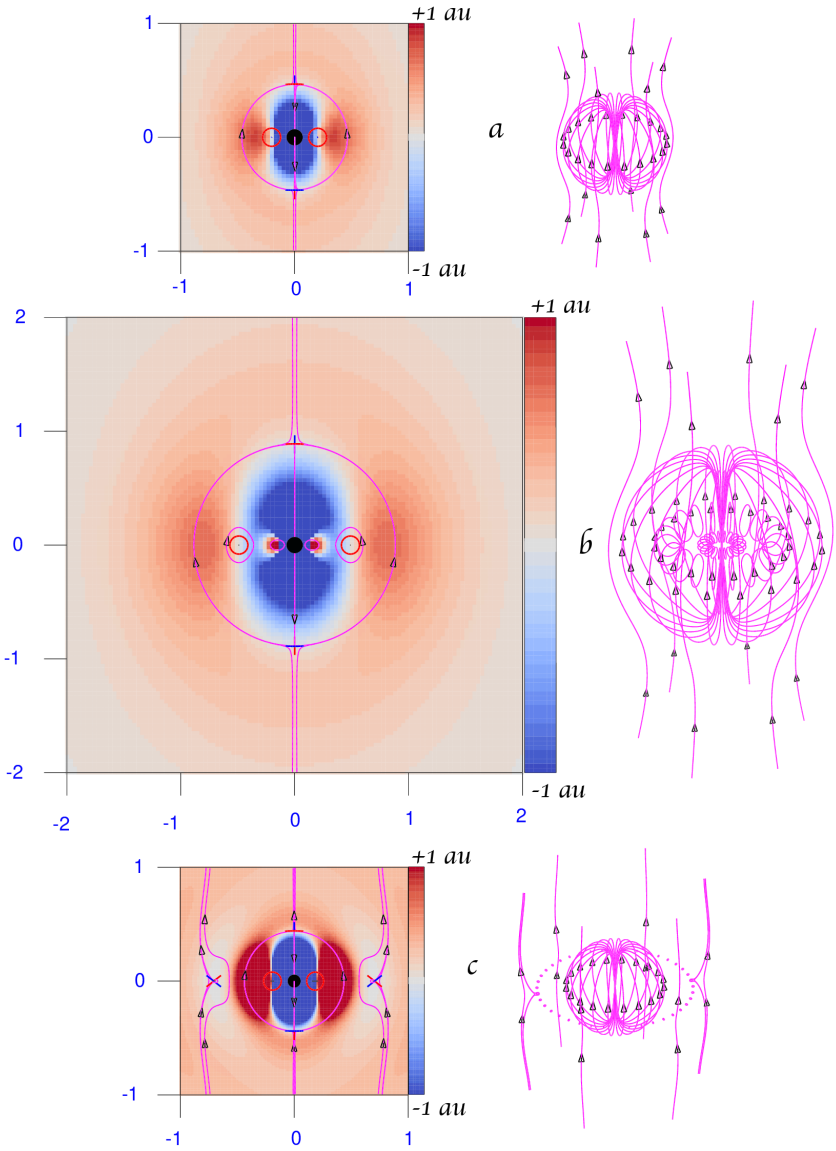

Figure 5.27: Anapole moments of rare gas atoms induced by the time derivative $\dot{\boldsymbol{E}}$ of monochromatic light with wavelength λ=589.3 nm, corresponding to sodium D line. **a**: Ne, **b**: Ar, **c**: Kr. Maps on the left show a section of the $\boldsymbol{J}^{\dot{\boldsymbol{E}}}$ vector field, by superimposing electric dipole polarisability density and heteroclinic streamlines that connect two conjugated saddle-nodes,[34] i.e., critical $(3, \pm 1)$ stagnation points corresponding to *source* and *sink* of the poloidal flow that generates a toroidal moment along the central symmetry axis of a torus represented on the right. The onion-like structure of the vector field is shown on the left of panel **b** via two closed orbits flanking the nucleus. They mark the intersection with the plot plane of inner poloidal currents observed on the right. A second torus of much smaller size, with stagnation circumference crossing the plot plane at ± 0.13 bohr, highlighted by red circles, was found in the proximity of the Ar nucleus. A peripheral poloidal circulation takes place in Kr.

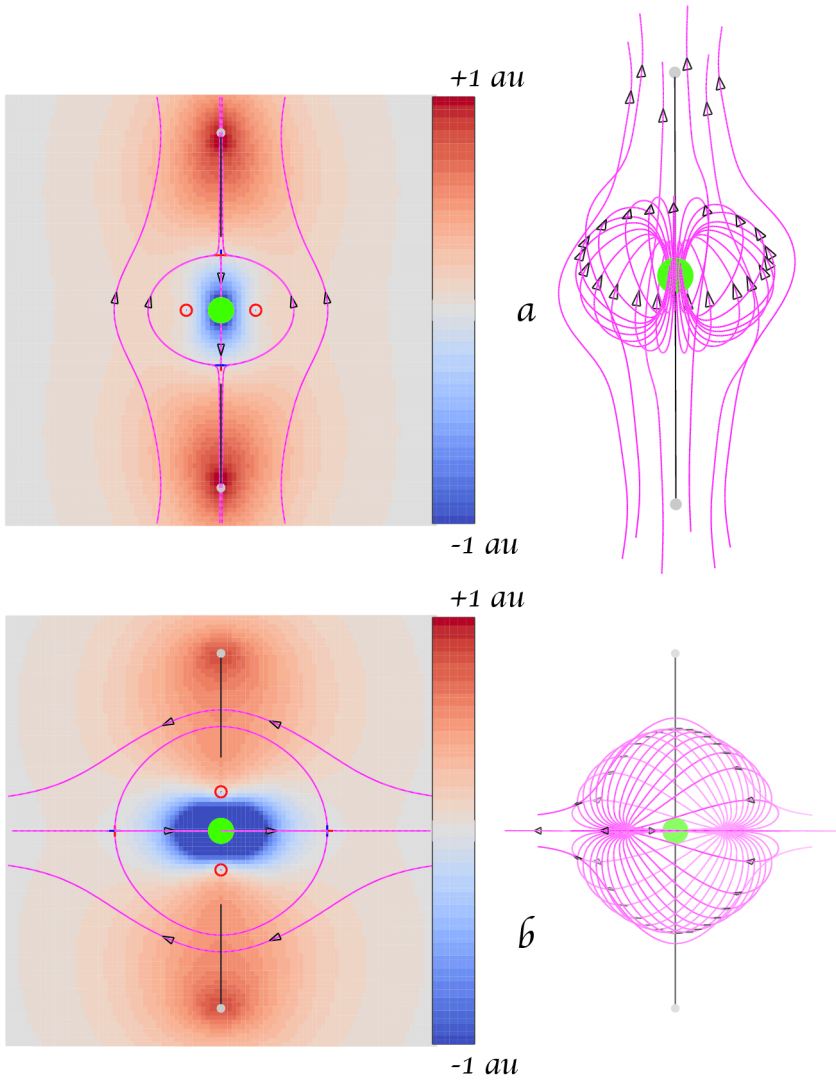

Figure 5.28: Anapole moments of BeH_2 induced by the time derivative $\dot{\boldsymbol{E}}$ of monochromatic light with wavelength λ=589.3 nm, corresponding to sodium D line. The maps on the left show a section of the $\boldsymbol{J}^{\dot{\boldsymbol{E}}}$ vector field, by superimposing a few streamlines onto the electric dipole polarisability density. Heteroclinic trajectories connect two conjugated saddle-nodes, i.e., critical $(3, \pm 1)$ stagnation points corresponding to source and sink of poloidal flow that generates a toroidal moment along the central symmetry axis of a torus represented on the right. On the left of panel **a** (**b**) the electric field $E_z\boldsymbol{\epsilon}_3$ is parallel ($E_x\boldsymbol{\epsilon}_1$, directed outward, is orthogonal) to the bond direction. The torus on the right of **b** has been rotated by $\approx 45^\circ$ about the z axis to improve visibility of source and sink on the x axis.

CHAPTER 6

Conclusions and Outlook

The general theory of first-order molecular density functions, which are connected to the molecular response to external electric and magnetic fields, has been developed in terms of induced charge and current densities.

The study started by considering first the well-established working methods already available for the calculation of the current density induced within the molecular electronic cloud interacting with a static magnetic field. Then, we considered interaction with time-dependent fields, associated to the radiation. The first part was preparatory to the second one, as it allowed the introduction of methods that solve the so-called gauge problem, which manifests itself in the approximate calculation of magnetic properties that depend on the reference origin. It has been shown that these methods, which exploit the continuous transformation of the origin of the current density (CTOCD), can be applied also when the inducing magnetic field depends on time.

Moreover, it has been shown how to obtain a reasonable description of the molecular system in the presence of radiation. This entails that different multipolar orders in the potentials defining the time-dependent electric and magnetic fields must be considered. In the simplest case (quadrupole approximation), it turns out that both the first-order time-dependent electronic charge density and the first-order time-dependent current density are made of six terms, three proportional respectively to the electric field, the magnetic field, and the gradient of the electric field, plus another three proportional to the time derivative of the fields. Only the sum of these contributions provides a total current density that is invariant with respect to passive and active translations of the origin for an exact calculation. All contributions to induced current and charge densities, with the exception of $\boldsymbol{J}^{\boldsymbol{\nabla}\dot{\boldsymbol{E}}}$ and $\rho^{\boldsymbol{\nabla}\boldsymbol{E}}$, have been implemented at TDHF and TDDFT level of theory.

The application of the theoretical methods studied and developed during the period of thesis can be listed separately for the static and the dynamic cases. For the current density induced by a static magnetic field, four studies have been performed. In particular, one for disentangling the contributions to the proton magnetic shielding in carbon nanohoops and nanobelts and another to characterize the magnetic behaviour of the infinitene molecule. For the dynamic case, six studies have been performed.

The contribution to the time-dependent current density provided by the time derivative of the electric field shows an interesting double-faced interpretation. From the one side, it is an unconventional vector field formed by toroidal circulations of electronic current around heavy molecular nuclei induced by the variation with time of the electric field; from the other side, it is a mixed electric-dipole magnetic-dipole polarizability density, which reveals negative contributions to the molecular polarizability in regions nearby heavy nuclei, in connection with the internal toroidal flow. The contribution to the current density provided by the time-dependent magnetic field has been implemented using the CTOCD-DZ method to ensure origin independent current density. Its topology has been analyzed. This contribution has been shown to provide, after the extraction of the time-dependent part, an optical rotatory power density, which is promising for the topological interpretation of the optical chirality.

With regard to upcoming activities, the contribution to current density provided by the electric field gradient will be implemented. In this way all terms appearing in (4.41) will be available to compute the total first order current density within the quadrupole approximation. Then, it will be interesting to evaluate the relative weights of the various contributions and fully verify the charge and current conservation constraint.

Also, the study and the implementation of other applications has commenced. In particular:

- the extension to open-shell systems;
- the study of the interaction with strong magnetic fields, which was initiated through an approach based on the finite field perturbation method in the static case, but which would be more appropriately addressed by calculating the time-dependent current density induced at second-order by an electromagnetic field.

Last but not least, the study of electron correlation effects on the induced current densities which has been my main argument of study and work during my stay abroad, concerning the implementation of method for the calculation of densities at CCSD level of theory. Preliminary results are reported in poster 3.

Posters

Posters presented at international meetings on the topic of the thesis in the three years period.

1. **Magnetic Characterization of the Infinitene Molecule** presented at the XV Italian Conference on Supramolecular Chemistry, SUPRAMOL2022, June 28 July 1 2022, Salerno, Proceedings P7;

2. **On the JAP method for the indirect determination of delocalized currents from experimental chemical shifts** presented at the XIX International Symposium on Novel Aromatic Compounds, ISNA19, 3-8 July 2022, Warsaw, Poland pag. 217;

3. **CCSD Calculation of Dynamic Polarizability Density and Toroidizability** presented at the "XVIII European Summer School in Quantum Chemistry 2022" September 11-24 2022, at Hotel Torre Normanna, Sicily.

Magnetic Characterization of the Infinitene Molecule

Guglielmo Monaco, Riccardo Zanasi, Francesco F. Summa*
Dipartimento di Chimica e Biologia "A. Zambelli", Università di Salerno, Italy

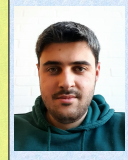

ABSTRACT

The origin-independent current density induced by a perpendicular magnetic field in the infinitene molecule [1] has been calculated, confirming the recently presented result by Orozco-Ic et al. [2] of **two disjointed global current pathways** along the edges formed by 24 carbon atoms having the form of the infinity symbol. The current strength has been assessed along the C–C bonds forming the two separate circuits, whose particular shape provides a diamagnetic exaltation which is only 73% of the expected value for this aromatic molecule. Through space currents have been found along the bond paths determined by the electron density gradient, whose strength is 10% that of the aromatic benzene ring current. It is shown that the pair of high-field ^{1}H NMR experimental signals carry the signature of the two global currents, which are counterrotating inside the fjord regions with respect to the rim of the coronene subunits.

SYSTEM

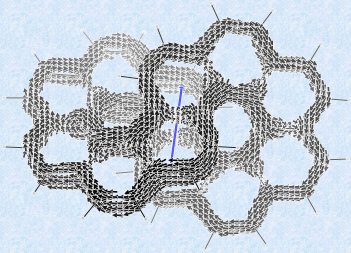

π-Electron current density induced in infinitene by a unitary magnetic field (blue arrow) parallel to the Cartesian *x*-axis, corresponding to C_2^x symmetry element.

METHODS

We have taken the geometry of the (*P*,*P*)-isomer of infinitene, optimized at the PBE0/6-311+G(d,p) level of theory in the gas phase, reported by Krzeszewski et al. [1] The symmetry point group of the structure is D_2 with the Cartesian *x*-axis perpendicular to the central C–C bonds of the stacked naphthalene subunits, as shown in Figure. Then, we have performed the calculation of the magnetically induced current density using the CTOCD-DZ method to ensure origin-independent results, [3] adopting the B97-2/6-311+G(2d,p) level of theory in the gas phase. The Gaussian 16 program was used to obtain the perturbed molecular orbitals with the CSGT keyword and the SYSMOIC program package [4] to perform the actual calculation of the current density. The entire procedure is a very simple one; details can be obtained visiting the link reported in ref [4].

DISCUSSION

(i) What pathways do the currents travel through?
(ii) Are they global, or local to Clar sextets?
(iii) Which tropicity do they display?
(iv) How do their strengths compare with the benzene ring current?
(v) How large is the exaltation of diamagnetism for this aromatic molecule?
(vi) How can the high-field ^{1}H NMR signals be justified on the basis of the actual current tropicity?

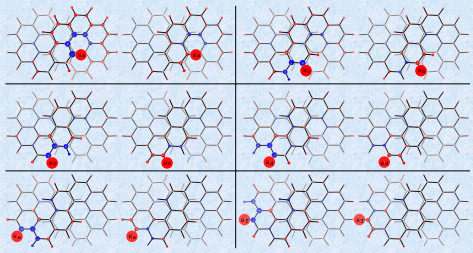

Spatial contributions to the proton magnetic shieldings. In each panel, contributions to the xx component of the tensor are plotted on the left beside the contributions to the isotropic component on the right. Shielding/deshielding contributions are shown in red/blue.

Contributions to the Isotropic Component of the Proton Magnetic Shieldings: Core, Sum of Shielding Spatial Contributions (SSSC), Sum of Deshielding Spatial Contributions (SDSC), and Proton Net Charges q_H

proton	core	SSSC	SDSC	total	δ_{cal}	δ_{Expt} [1]	q_H
H_a	18.85	8.91	−3.41	24.35	7.14	6.99	0.1675
H_b	19.83	6.95	−1.74	25.04	6.44	6.43	0.1320
H_c	19.76	5.79	−1.70	23.86	7.62	7.60	0.1387
H_d	19.79	5.49	−1.88	23.41	8.08	8.04	0.1385
H_e	19.76	5.36	−1.88	23.24	8.24	8.18	0.1398
H_f	19.78	5.25	−1.76	23.27	8.22	8.16	0.1433

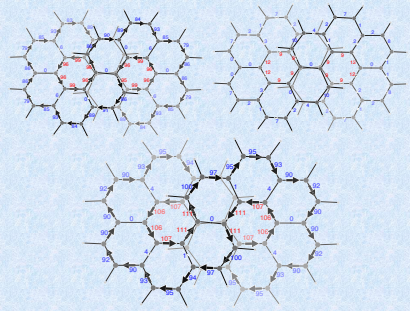

Calculated bond current strengths in infinitene. Top left, **π**-electron contribution; top right, contribution from all the remaining orbitals; bottom, all electrons. Numbers attached to each arrow give the current strength in percentage with respect to the benzene ring current strength of 12.0 nA/T.

CONCLUSIONS

Returning to the unsolved questions underlined before for infinitene, we have shown the following: (iv) As for the strength of the current, induced by a perturbing magnetic field perpendicular to the central C−C bonds of the two stacked naphthalene subunits, in the K-regions it is 1.5 times weaker than the diatropic current that circulates on pristine coronene rim, while in the fjord the current is 2 times stronger than the paratropic current on pristine coronene hub. (v) The exaltation of diamagnetism is fairly low, being only 73% of the expected value. (vi) The high-field ^{1}H NMR signals are due to the global currents flowing on the fjord region and on the carbon atoms on the lower benzene rings and K-edges, with a fairly large deshielding effect on H_a , the former, and shielding effects on both H_a and H_b , the latter.

REFERENCES

[1] Krzeszewski, M.; Ito, H.; Itami, K. *J. Am. Chem. Soc.* **2022**, *144*, 862−871.
[2] Orozco-Ic, M.; Valiev, R. R.; Sundholm, D. *Phys. Chem. Chem. Phys.* **2022**, *24*, 6404−6409.
[3] Lazzeretti, P.; Malagoli, M.; Zanasi, R. *Chem. Phys. Lett.* **1994**, *220*, 299– 304.
[4] Monaco, G.; Summa, F. F.; Zanasi, R. *J. Chem. Inf. Model.* **2021**, *61*, 270–283.

Figure 6.1: SUPRAMOL 2022, "XV Italian Conference on Supramolecular Chemistry" Jun. 28-Jul. 1, Salerno, Proceedings P7.

On the JAP method for the indirect determination of delocalized currents from experimental chemical shifts

Alessandro Landi, Francesco F. Summa, Riccardo Zanasi , Guglielmo Monaco*
Dipartimento di Chimica e Biologia "A. Zambelli", Università di Salerno, Italy

ABSTRACT

The **JAP model** (after **Jirásek, Anderson, and Peeks** [1]) aims at **retrieving global current strengths from experimental ^{1}H chemical shifts**. Owing to the present capabilities of accurate computations of current strengths, the efficacy of the model has been tested with DFT computations using **SYSMOIC** [2]. Both global and local tropicities are correctly predicted in most cases and the quantitative agreement is overall fair. An extension of the model is found to give improvement in an exemplary critical case, where the global delocalized current is negligible and the current density map is dominated by local currents.

SYSTEMS

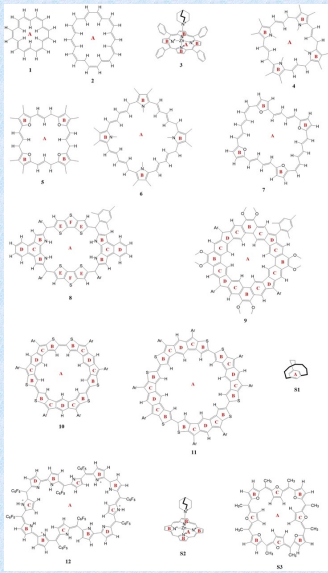

METHODS

Magnetically induced currents have been obtained by SYSMOIC[37] starting from wavefunction files (.wfx) obtained by Gaussian16[38] run at the BHandHLYP/6-31G* level on geometries optimized at the same level. The functional used is one of the best for the calculation of the magnetic response, according to gradings based on magnetizabilities[39] and hypervirial relationships.[40] Global current strengths have been computed integrating the current crossing a plane bisecting a C-C bond up to 10^{-3} atomic units (at this level the reference benzene ring current is -12.2 nA T^{-1}). Numerical results are collected in Table 1. Accurate determination of local currents is less straightforward, because the large areas associated to small integration thresholds can include contribution associated to different bonds and a criterion is needed to assign contributions to individual bonds. In this work local currents have been first obtained at the less demanding $2{\cdot}10^{-2}$ atomic units level (the reference benzene ring current reduces to -10.3 nA T^{-1}; percent values are reported in Fig.s S1 and S2, with or without the sketch of the integration domains, which are useful to grasp the shape of the currents). Current in percent units of the benzene current strength are only approximately preserved when different integration thresholds are used. As a correction for this error, best values of local signed current strength, e.g. for ring B, have been obtained by the equation in yellow.

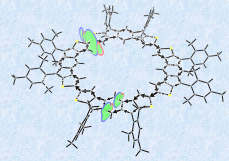

$$I_{\mathrm{corr},B} = I^{(10^{-3})}_{\mathrm{global}} \frac{I^{(2\cdot10^{-2})}_{B}}{I^{(2\cdot10^{-2})}_{\mathrm{global}}}.$$

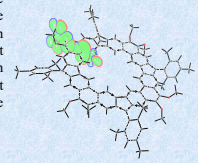

WHERE DO RESIDUAL DISCREPANCIES COME FROM?

The Biot-Savart law, used to develop the equations of the model, is known to work exactly also in the quantum mechanical domain, provided the correct current density is used. Therefore, the problems can only come from the inadequate modeling of the current density. In this respect the assumptions of the JAP model can be summarized as follows:

I) The macrocycle is assumed to have a single conformation, built upon gas-phase B3LYP/6-31G* optimization starting from the crystallographic structure,

🤔 Geometry can be a problem. [3]

II) the contributions to the shielding of the *i*-th spectator atom coming from different directions of the external field are weighted by the net projected cross-section area of the circuit along the direction of the applied magnetic field

🤔 Strictly correct for planar monocycles only

III) the shape of the current is that of two infinitely thin homotropic circuits displaced from the average local plane by ±0.7 Å (the displacement is in-plane for porhyrins),

🤔 Heterotropic circulations do occur in cycloporphyrins [4]

IV) local currents are preserved passing from the reference compounds to the studied macrocycles,

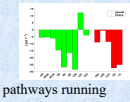

🤔🤔 Does not seem the case

V) delocalized currents run along one or few equally weighted piecewise linear pathways running along selected conjugated circuits running all along the macrocycle

🤔🤔 Problematic for localized patterns. Extension of the model to fit more than a ring current revealed cumbersome, due to heavy correlation of the fit parameters, but good results were obtained in the case of **9**$^{4+}$.

RESULTS

👍

	R^2	I_{JAP}	I_{DFT}	%err	ϕ^{ok}_{TROP}
1	0.97	-13.3	-13.3	0	**1/1**
2	0.97	-10.1	-8.4	20	**1/1**
3	0.98	-38.0	-25.1	51	**2/2**
4^{2+}	0.99	-25.9	-38.5	-33	**2/2**
5^{2+}	0.98	-26.6	-33.8	-21	**2/2**
6^{2+}	0.99	-33.4	-25.2	33	**2/2**
7^{2+}	0.96	-28.3	-27.6	3	**2/2**
8^{2+}	0.97	-29.3	-25.1	17	**3/6**
9^{2+}	0.91	-22.7	-36.9	-38	**3/4**
10^{2+}	0.99	-20.1	-32.6	-38	**3/4**
11^{2+}	0.99	-26.7	-43.1	-38	**3/4**
12^{4+}	0.94	-33.0	-6.9	3787	**1/4**
12^{4+} [a]			-34.5	2	**1/4**
9^{2-}	0.84	-12.9	-28.1	-54	**3/4**
9^{4-}	0.23	5.0	1.8	178	**1/4**
10	0.88	8.6	11.8	-27	**2/4**
11	0.96	7.0	3.1	126	**2/4**
S1	0.96	-11.2	-9.3	20	**1/1**
S2	0.99	-29.8	-26.7	12	**2/2**
S3	**0.94**	**5.1**	**2.1**	**50**	**2/3**

Table 1. Signed current strengths (in nA T^{-1}) retrieved by the JAP method and by DFT. R^2 is the coefficient of determination of the JAP linear model taken from ref. [1]. %err is the percent error of the I_{JAP} over the I_{DFT} values. The fraction of rings whose tropicity is predicted correctly, ϕ^{ok}_{TROP}, is given in the last column.

CONCLUSIONS

JAP model is effective in recovering global and local tropicities, but errors of the order of a full benzene ring current can occur. In percent term, the largest error has been reported for a calculation on **12**$^{4+}$ and for **9**$^{4+}$, a system with a negligible global ring current, dominated by local currents. The application of variants with more ring current parameters to other system will be non-trivial, not only because of the strong correlation of the parameters, but also because choosing the proper reference system can be complicated, especially in bent systems [5], so that presently the indirect route of retrieving the current density from few experimental chemical shifts should still be considered a rough and bumpy challenging road.

REFERENCES

[1] Jirásek, M.; Anderson, H. L.; Peeks, M. D. *Acc. Chem. Res.* **2021**, *54*, 3241–3251.
[2] Monaco, G.; Summa, F. F.; Zanasi, R. *J. Chem. Inf. Model.* **2021**, *61*, 270–283.
[3] Matito, E.; Casademont, I.; Ramos-Cordoba, E.; Torrent-Sucarrat, M.; Guerrero-Avilés, R. *Angew. Chem. Int. Ed.* **2021**,
[4] Landi, A.; Summa, F. F.; Monaco, G. *Chemistry* **2021**, *3*, 991–1004.
[5] Summa, F. F.; Monaco, G.; Scott, L. T.; Zanasi, R. *J. Phys. Chem. Lett.* **2020**, 7489–7494.

Figure 6.2: ISNA19, "XIX International Symposium on Novel Aromatic Compounds, 3-8 July, Warsaw, pag. 217.

CCSD Calculations of Dynamic Polarizability Density and Toroidizability

G. Monaco[a], R. Zanasi[a], S. Coriani[b], J. H. Andersen[b] and F. F. Summa[a,b]
[a]Department of Chemistry and Biology "A. Zambelli", University of Salerno, Italy
[b]DTU Chemistry, Technical University of Denmark

A physically meaningful, origin-independent, definition of the polarizability density function was found to be equivalent to the current density due to the time derivative of the electric field[1]

$$\mathcal{J}_\alpha^{\hat{E}_\beta}(\boldsymbol{r},\omega) = \frac{ne^2}{m_e\hbar}\sum_{j\neq a}\left(\omega_{ja}^2-\omega^2\right)^{-1}\times\Im\left\{\left\langle a\left|\hat{R}_\beta\right|j\right\rangle\int\Psi_j^{(0)*}(\boldsymbol{r},\boldsymbol{X}_1)\,\hat{p}_\alpha\Psi_a^{(0)}(\boldsymbol{r},\boldsymbol{X}_1)\,d\boldsymbol{X}_1-\int\Psi_a^{(0)*}(\boldsymbol{r},\boldsymbol{X}_1)\,\hat{p}_\alpha\Psi_j^{(0)}(\boldsymbol{r},\boldsymbol{X}_1)\,d\boldsymbol{X}_1\left\langle j\left|\hat{R}_\beta\right|a\right\rangle\right\}$$

since $\int\mathcal{J}_\alpha^{\hat{E}_\beta}(\boldsymbol{r},\omega)d^3r=\alpha_{\beta\alpha}^{(R,P)}(\omega)=\frac{e^2}{m_e\hbar}\sum_{j\neq a}\frac{2}{\omega_{ja}^2-\omega^2}\Im\left\{\left\langle a\left|\hat{R}_\beta\right|j\right\rangle\left\langle j\left|\hat{P}_\alpha\right|a\right\rangle\right\}$, where $\alpha_{\beta\alpha}^{(R,P)}$ is the frequency dependent electric dipole

polarizability in the mixed dipole length-dipole velocity formalism, which is equivalent to that in the dipole gauge via off-diagonal hypervirial relationships. Here we present an improved level of calculation from

TDHF/TDDFT[1] ⟹ TDCCSD[2]

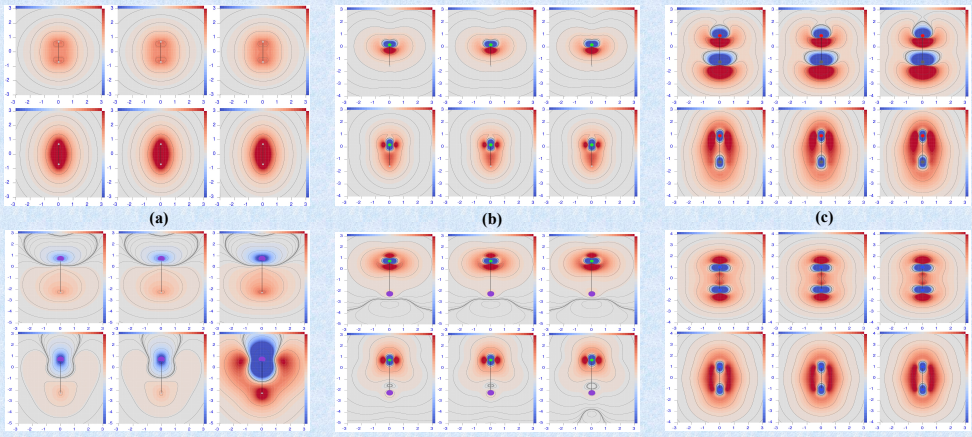

Diverging color map of the origin-independent polarizability density functions calculated at CCSD/aug-pcSseg2 level of theory. Top/bottom row shows the perpendicular/parallel component for three radiation wave-lengths, λ = 633, 589.3, 355 nm, from left to right, respectively of H_2 **(a)**, HF **(b)**, CO **(c)**, LiH **(d)**, LiF **(e)** and N_2 **(f)**. Red positive, blue negative.

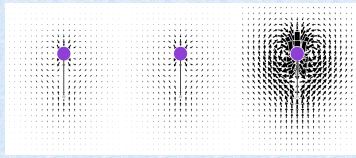

Instant views of the current density induced in LiH by the time derivative of the electric field of the radiation parallel to the symmetry axis of the molecule. Left λ = 633 nm, center λ = 589.3 nm, right λ = 355 nm. Owing to axial symmetry, rotating about the z-axis a torus is generated.

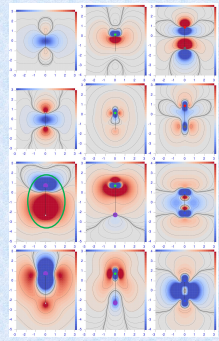

Difference maps of the polarizability density calculated at CCSD minus HF level of theory for λ = 633 nm. First/second row ⊥/∥ component, from left to right for H_2, HF, CO, side bar is ± 0.01, ± 0.1, and ± 0.1 a.u. respectively. Third/fourth row ⊥/∥ component, from left to right for LiH, LiF, N_2, side bar is ± 0.1, 0.1, and ± 0.05 a.u. respectively. Red positive, blue negative.

Table 1: Electric dipole polarizability in mixed dipole length-dipole velocity formalism in a.u. calculated at CCSD and HF theory levels using the aug-pcSseg2 basis set.

Mol	CCSD						HF					
	α_{xx}			α_{zz}			α_{xx}			α_{zz}		
	633	589.3	355	633	589.3	355	633	589.3	355	633	589.3	355
H_2	4.26	4.29	4.45	6.53	6.55	6.83	4.26	4.40	4.56	6.59	6.61	6.90
LiH	34.92	35.93	61.15	33.20	34.71	303.67	28.70	29.33	42.21	25.74	26.48	52.62
HF	5.25	5.26	5.40	6.37	6.38	6.52	4.47	4.48	4.57	5.76	5.77	5.88
LiF	10.21	10.26	11.15	9.89	9.93	10.53	7.73	7.76	8.14	7.56	7.58	7.86
N_2	9.91	9.93	10.20	13.82	13.85	14.25	9.83	9.84	10.07	15.15	15.18	15.65
CO	11.62	11.66	12.20	15.19	15.23	15.76	11.42	11.46	11.97	14.62	14.65	15.12

Comparing CCSD and HF results, it clearly emerges that, point by point, the electron correlation effects are much larger than one would argue considering the integrated dipole electric polarizability alone reported in the table.

REFERENCES

[1] Summa, F. F.; Monaco, G.; Lazzeretti, P.; Zanasi, R. J. Phys. Chem. Lett. 2021, 12, 8855 8864.
[2] Faber, R.; Andersen, J. H.; Coriani, S. py-ccrsp, Python module for CC and EOM-CC response experiments. 2020-2022.
[3] Monaco, G.; Summa, F. F.; Zanasi, R. J. Chem. Inf. Model. 2021, 61, 270 283.

Figure 6.3: "XVIII European Summer School in Quantum Chemistry 2022" 11-24 Sept., at Hotel Torre Normanna, Sicily.

Bibliography

[1] T. B. Pedersen, Introduction to Response Theory, in *Handbook of Computational Chemistry*, edited by J. Leszczynski et al., pages 269–294, Springer International Publishing, Cham, 2017.

[2] N. Marzari, A. Ferretti, and C. Wolverton, Nat. Mater. **20**, 736 (2021).

[3] S. P. A. Sauer, *Molecular electromagnetism: a computational chemistry approach*, Oxford graduate texts, Oxford University Press, Oxford ; New York, 2011.

[4] T. Helgaker et al., Chem. Rev. **112**, 543 (2012).

[5] P. Norman, K. Ruud, and T. Saue, *Principles and practices of molecular properties: theory, modeling and simulations*, John Wiley & Sons, Hoboken, NJ, 2018.

[6] C. J. Jameson and A. D. Buckingham, J. Phys. Chem. **83**, 3366 (1979).

[7] C. J. Jameson and A. D. Buckingham, J. Chem. Phys. **73**, 5684 (1980).

[8] J. A. Pople, The Journal of Chemical Physics **24**, 1111 (1956).

[9] J. A. Pople, Molecular Physics **1**, 175 (1958).

[10] R. McWeeny, Molecular Physics **1**, 311 (1958).

[11] P. Lazzeretti, Prog. Nucl. Magn. Reson. Spectrosc. **36**, 1 (2000).

[12] J. Jusélius, D. Sundholm, and J. Gauss, J. Chem. Phys. **121**, 3952 (2004).

[13] G. Monaco, R. Zanasi, S. Pelloni, and P. Lazzeretti, J. Chem. Theory Comput. **6**, 3343 (2010).

[14] G. Monaco, F. F. Summa, and R. Zanasi, J. Chem. Inf. Model. **61**, 270 (2021).

[15] J. D. Jackson, *Classical electrodynamics*, Wiley, New York, 3rd ed edition, 1999.

[16] O. Heaviside, *Electromagnetic Theory*, volume 1, Chelsea publishing company, 1971.

[17] O. Heaviside, *Electromagnetic Theory*, volume 2, Chelsea publishing company, 1971.

[18] O. Heaviside, *Electromagnetic Theory*, volume 3, Chelsea publishing company, 1971.

[19] W. K. H. Panofsky and M. Phillips, *Classical Electricity and Magnetism*, Addison-Wesley Publishing Company, 1962.

[20] A. M. Stewart, Eur. J. Phys. **24**, 519 (2003).

[21] A. Stewart, Sri Lankan J Phys **12**, 33 (2012).

[22] R. McWeeny, *Methods of molecular quantum mechanics*, Theoretical chemistry, Academic Press, London, 2. aufl edition, 1992.

[23] H. Goldstein, C. Poole, and J. Safko, *Classical Mechanics*, Addison Wesley, 2002.

[24] M. Gell-Mann, Nuovo Cim **4**, 848 (1956).

[25] M. Born and R. Oppenheimer, Annalen der Physik **389**, 457 (1927).

[26] F. Bloch, Zur Wirkung äußerer elektromagnetischer Felder auf kleine Systeme, in *Werner Heisenberg und die Physik unserer Zeit*, edited by F. Bopp, pages 93–102, Vieweg+Teubner Verlag, Wiesbaden, 1961.

[27] M. Göppert-Mayer, Annalen der Physik **401**, 273 (1931).

[28] R. F. W. Bader and P. L. A. Popelier, Int. J. Quantum Chem. **45**, 189 (1993).

[29] R. F. W. Bader, *Atoms in molecules: a quantum theory*, Number 22 in The International series of monographs on chemistry, Clarendon Press ; Oxford University Press, Oxford [England] : New York, 1994.

[30] P. L. A. Popelier and F. M. Aicken, ChemPhysChem **4**, 824 (2003).

[31] G. Bruno, G. Macetti, L. Lo Presti, and C. Gatti, Molecules **25**, 3537 (2020).

[32] G. Monaco and R. Zanasi, J. Chem. Phys. **153**, 104114 (2020).

[33] P. Popelier, *Atoms in molecules: an introduction*, Prentice Hall, Harlow, 2000.

[34] J. W. Reyn, Z. Angew. Math. Phys. **15**, 540 (1964).

[35] W. Cao, C. Gatti, P. MacDougall, and R. Bader, Chemical Physics Letters **141**, 380 (1987).

[36] C. F. Matta and R. J. Boyd, editors, *The quantum theory of atoms in molecules: from solid state to DNA and drug design*, WILEY-VCH, Weinheim, 2007.

[37] L. D. Landau, E. M. Lifšic, and L. D. Landau, *Quantum mechanics: non-relativistic theory*, Number Vol. 3 in Course of theoretical physics / by L. D. Landau and E. M. Lifshitz, Elsevier [u.a.], Singapore, 3. ed., rev. and enl., authorized engl. reprint ed edition, 2007.

[38] W. B. Hodge, S. V. Migirditch, and W. C. Kerr, American Journal of Physics **82**, 681 (2014).

[39] F. F. Summa and R. Citro, Physchem **2**, 96 (2022).

[40] P. Lazzeretti, The Journal of Chemical Physics **150**, 184117 (2019).

[41] P. Lazzeretti, Theor Chem Acc **131**, 1222 (2012).

[42] J. O. Hirschfelder, J. Chem. Phys. **68**, 5151 (1978).

[43] T. A. Keith and R. F. Bader, Chem. Phys. Lett. **210**, 223 (1993).

[44] P. Lazzeretti, M. Malagoli, and R. Zanasi, Chem. Phys. Lett. **220**, 299 (1994).

[45] E. Steiner and P. W. Fowler, Chem. Commun. , 2220 (2001).

[46] E. Steiner and P. W. Fowler, J. Phys. Chem. A **105**, 9553 (2001).

[47] S. Coriani, P. Lazzeretti, M. Malagoli, and R. Zanasi, Theoret. Chim. Acta **89**, 181 (1994).

[48] P. Fowler, R. Zanasi, B. Cadioli, and E. Steiner, Chem. Phys. Lett. **251**, 132 (1996).

[49] R. Zanasi, P. Lazzeretti, M. Malagoli, and F. Piccinini, J. Chem. Phys. **102**, 7150 (1995).

[50] P. Lazzeretti and R. Zanasi, Int. J. Quantum Chem. **60**, 249 (1996).

[51] A. Soncini, P. Lazzeretti, and R. Zanasi, Chemical Physics Letters **421**, 21 (2006).

[52] R. Zanasi, J. Chem. Phys. **105**, 1460 (1996).

[53] A. D. Becke, J. Chem. Phys. **88**, 2547 (1988).

[54] G. Monaco, F. F. Summa, and R. Zanasi, Chem. Phys. Lett. **745**, 137281 (2020).

[55] J. R. Cheeseman, G. W. Trucks, T. A. Keith, and M. J. Frisch, J. Chem. Phys. **104**, 5497 (1996).

[56] M. J. Frisch et al., Gaussian16 Revision C.01, 2016, Gaussian Inc. Wallingford CT.

[57] S. T. Epstein, *The variation method in quantum chemistry*, Number v. 33 in Physical chemistry, a series of monographs, Academic Press, New York, 1974.

[58] F. F. Summa, G. Monaco, P. Lazzeretti, and R. Zanasi, Phys. Chem. Chem. Phys. **23**, 10.1039.D1CP01298C (2021).

[59] H. Sambe, The Journal of Chemical Physics **59**, 555 (1973).

[60] G. P. Arrighini, C. Guidotti, M. Maestro, R. Moccia, and O. Salvetti, The Journal of Chemical Physics **49**, 2224 (1968).

[61] M. Hamermesh, *Group theory and its application to physical problems*, Dover books on physics and chemistry, Dover Publications, New York, 1989.

[62] E. P. Wigner and J. J. Griffin, *Group theory and its applications to the quantum mechanics of atomic spectra*, Number 5 in Pure and applied physics, Academic press, New York [etc.], expanded and improved ed edition, 1959.

[63] A. Shubnikov and N. Belov, *Coloured Symmetry*, Pergamon Press, Oxford, 1964.

[64] B. Tavger and V. Zaitsev, Journal of Experimental and Theoretical Physics **3**, 430 (1956).

[65] J. A. N. F. Gomes, J. Chem. Phys. **78**, 4585 (1983).

[66] J. A. N. F. Gomes, Phys. Rev. A **28**, 559 (1983).

[67] T. A. Keith and R. F. W. Bader, J. Chem. Phys. **99**, 3669 (1993).

[68] T. J. P. Irons, A. Garner, and A. M. Teale, Chemistry **3**, 916 (2021).

[69] S. Pelloni, F. Faglioni, R. Zanasi, and P. Lazzeretti, Phys. Rev. A **74** (2006).

[70] S. Pelloni, P. Lazzeretti, and R. Zanasi, J. Phys. Chem. A **111**, 8163 (2007).

[71] S. Pelloni, P. Lazzeretti, and R. Zanasi, J. Phys. Chem. A **111**, 3110 (2007).

[72] S. Pelloni, P. Lazzeretti, and R. Zanasi, Theor. Chem. Acc. **123**, 353 (2009).

[73] S. Pelloni and P. Lazzeretti, Int. J. Quantum Chem. **111**, 356 (2011).

[74] G. Monaco, P. D. Porta, M. Jabłoński, and R. Zanasi, Phys. Chem. Chem. Phys. **17**, 5966 (2015).

[75] R. Carion et al., J. Chem. Theory Comput. **6**, 2002 (2010).

[76] G. Monaco and R. Zanasi, J. Phys. Chem. A **123**, 1558 (2019).

[77] P. Lazzeretti, Phys. Chem. Chem. Phys. **18**, 11765 (2016).

[78] R. Abraham, J. E. Marsden, and T. S. Raţiu, *Manifolds, tensor analysis, and applications*, Number v. 75 in Applied mathematical sciences, Springer-Verlag, New York, 2nd ed edition, 1988, p. 268.

[79] P. Lazzeretti, J. Chem. Phys. **149**, 154106 (2018).

[80] P. W. Langhoff, S. T. Epstein, and M. Karplus, Rev. Mod. Phys. **44**, 602 (1972).

[81] N. S. Piskunov, G. Der Mégréditchian, and E. Gloukhian, *Calcul différentiel et intégral*, Éd. Mir Ellipses, Moscou [Paris], 3 ème éd edition, 1969, Exemple 6, p. 395.

[82] R. D. Mattuck, *A guide to Feynman diagrams in the many-body problem*, Dover books on physics and chemistry, Dover Publications, New York, 2nd ed edition, 1992, p. 377.

[83] P. Lazzeretti, *General Connections Among Nuclear Electromagnetic Shieldings and Polarizabilities*, pages 507–549, John Wiley & Sons, Ltd, 1989.

[84] P. Roman, *Advanced quantum theory: an outline of the fundamental ideas*, Addison-Wesley series in advanced physics, Addison-Wesley, Reading, Mass, 1965.

[85] D. Moncrieff and S. Wilson, Journal of Physics B: Atomic, Molecular and Optical Physics **26**, 1605 (1993).

[86] J. H. Van Vleck, *The theory of electric and magnetic susceptibilities*, Oxford University Press, 1965.

[87] P. Lazzeretti, J. Chem. Phys. **151**, 114108 (2019).

[88] F. F. Summa, G. Monaco, R. Zanasi, S. Pelloni, and P. Lazzeretti, Molecules **26**, 4195 (2021).

[89] R. W. Havenith and P. W. Fowler, Chem. Phys. Lett. **449**, 347 (2007).

[90] A. Soncini, A. M. Teale, T. Helgaker, F. De Proft, and D. J. Tozer, J. Chem. Phys. **129**, 074101 (2008).

[91] Y. Li, Y. Segawa, A. Yagi, and K. Itami, J. Am. Chem. Soc. **142**, 12850 (2020).

[92] F. F. Summa, G. Monaco, L. T. Scott, and R. Zanasi, J. Phys. Chem. Lett. **11**, 7489 (2020).

[93] T. J. P. Irons et al., J. Phys. Chem. A **124**, 1321 (2020).

[94] G. Monaco and R. Zanasi, J. Phys. Chem. Lett. **8**, 4673 (2017).

[95] G. Monaco, E. L. T. Scott, and R. Zanasi, ChemistryOpen **9**, 616 (2020).

[96] M. Jirásek, H. L. Anderson, and M. D. Peeks, Acc. Chem. Res. **54**, 3241 (2021).

[97] R. Haddon, Tetrahedron **28**, 3613 (1972).

[98] A. Landi, F. F. Summa, and G. Monaco, Chemistry **3**, 991 (2021).

[99] T. Soya, W. Kim, D. Kim, and A. Osuka, Chem. Eur. J. **21**, 8341 (2015).

[100] M. Krzeszewski, H. Ito, and K. Itami, J. Am. Chem. Soc. **144**, 862 (2022).

[101] P. Lazzeretti, Progress in Nuclear Magnetic Resonance Spectroscopy **36**, 1 (2000).

[102] J. A. Pople, J. Chem. Phys. **24**, 1111 (1956).

[103] J. A. N. F. Gomes and R. B. Mallion, Chem. Rev. **101**, 1349 (2001).

[104] E. Paenurk and R. Gershoni-Poranne, Phys. Chem. Chem. Phys. , (2022).

[105] P. v. R. Schleyer, C. Maerker, A. Dransfeld, H. Jiao, and N. J. R. v. E. Hommes, J. Am. Chem. Soc. **118**, 6317 (1996).

[106] E. Steiner, P. W. Fowler, and L. W. Jenneskens, Angew. Chem. Inter. Ed. **40**, 362 (2001).

[107] J. Jusélius, D. Sundholm, and co workers, Gimic, gauge-including magnetically induced currents, a stand-alone program for the calculation of magnetically induced current density.

[108] M. Orozco-Ic, R. R. Valiev, and D. Sundholm, Phys. Chem. Chem. Phys. **24**, 6404 (2022).

[109] P. J. Wilson, T. J. Bradley, and D. J. Tozer, J. Chem. Phys. **115**, 9233 (2001).

[110] B. P. Pritchard, D. Altarawy, B. Didier, T. D. Gibson, and T. L. Windus, J. Chem. Inf. Model. **59**, 4814 (2019).

[111] R. Zanasi and P. Fowler, Chem. Phys. Lett. **238**, 270 (1995).

[112] H. Fliegl, D. Sundholm, S. Taubert, J. Jusélius, and W. Klopper, J. Phys. Chem. A **113**, 8668 (2009), PMID: 19586004.

[113] R. K. Jinger et al., J. Phys. Chem. A **125**, 1778 (2021).

[114] F. F. Summa, G. Monaco, and R. Zanasi, Croat. Chem. Acta **94** (2021).

[115] M. W. Lodewyk, M. R. Siebert, and D. J. Tantillo, Chem. Rev. **112**, 1839 (2012).

[116] H. E. Gottlieb, V. Kotlyar, and A. Nudelman, J. Org. Chem. **62**, 7512 (1997).

[117] J. Ran and M. W. Wong, J. Phys. Chem. A **110**, 9702 (2006).

[118] P. Jørgensen and J. Linderberg, Int. J. Quantum Chem. **4**, 587 (1970).

[119] R. Bauernschmitt and R. Ahlrichs, Chem. Phys. Lett. **256**, 454 (1996).

[120] M. Casida and M. Huix-Rotllant, Annu. Rev. of Phys. Chem. **63**, 287 (2012).

[121] F. F. Summa, G. Monaco, R. Zanasi, and P. Lazzeretti, J. Chem. Phys. **156**, 154105 (2022).

[122] V. Guillemin and A. Pollack, *Differential topology*, AMS Chelsea Pub, Providence, R.I, 2010.

[123] J.-P. Brasselet, J. Seade, and T. Suwa, *Vector fields on Singular Varieties*, volume 1987 of *Lecture Notes in Mathematics*, Springer Berlin Heidelberg, Berlin, Heidelberg, 2009.

[124] X. Tricoche and C. Garth, in *Mathematical foundations of scientific visualization, computer graphics, and massive data exploration*, edited by T. Möller, B. Hamann, R. D. Russell, and B. I. R. S. for Mathematics Innovation & Discovery, Mathematics and visualization, pages 89–107, Springer, Berlin, 2009.

[125] Within the color convention adopted to represent stagnation lines, for an observer at a distance from the figure, the sense of rotation, given by the curl $\boldsymbol{\nabla} \times \boldsymbol{J}^{\boldsymbol{B}}$, is diatropic (paratropic) about a green (red) segment. In fact, all the vortices rotating on the donut-shaped surface have the same direction, as shown by the small loops in the vicinity of the point separating green and red lines: vortical streamlines flow up through the center and down around the sides.

[126] A. D. Becke, J. Chem. Phys. **98**, 1372 (1993).

[127] F. Jensen, J. Chem. Theory Comput. **11**, 132 (2015).

[128] F. F. Summa, G. Monaco, P. Lazzeretti, and R. Zanasi, J. Phys. Chem. Lett. **12**, 8855 (2021).

[129] F. F. Summa, G. Monaco, R. Zanasi, and P. Lazzeretti, J. Chem. Phys. **156**, 054106 (2022).

[130] V. Lebedev, Dokl. Akad. Nauk **338**, 454 (1994).

[131] M. Abramowitz and I. A. Stegun, editors, *Handbook of mathematical functions: with formulas, graphs, and mathematical tables*, Dover books on mathematics, Dover Publ, New York, NY, 9. dover print.; [nachdr. der ausg. von 1972] edition, 2013.

[132] J. Muenter, J. Mol. Spectrosc. **55**, 490 (1975).

[133] P. Norman, D. M. Bishop, H. Jørgensen Aa. Jensen, and J. Oddershede, J. Chem. Phys. **115**, 10323 (2001).

[134] J. R. Hammond, W. A. de Jong, and K. Kowalski, J. Chem. Phys. **128**, 224102 (2008).

[135] P. Lazzeretti, J. Chem. Phys. **153**, 074102 (2020), and references therein.

[136] K. Marinov, A. D. Boardman, V. A. Fedotov, and N. Zheludev, New J. Phys. **9**, 324 (2007).

[137] P. J. Mohr, D. B. Newell, B. N. Taylor, and E. Tiesinga, Metrologia **55**, 125 (2018), See also https://physics.nist.gov/cuu/Constants/index.html.